02/02/2026, 09:16:31

Compare Results

Old File:		New File:
PE_study.pdf	versus	**PartI_PartII_merged.pdf**
38 pages (8,14 MB)		**71 pages (38,08 MB)**
01/02/2026, 19:49:15		02/02/2026, 07:35:37

Total Changes

1212

Content

309 Replacements

307 Insertions

263 Deletions

Styling and Annotations

72 Styling

261 Annotations

Go to First Change (page 1)

Annual wake impacts in and between wind farm clusters - Part I: WRF simulated wake losses for different atmospheric conditions

Sara Porchetta[1,2,3], Wim Munters[3], Maxime Lejeune[3], Ruben Borgers[4], Sophia Buckingham[5], and Michael F. Howland[1]

[1]Massachusetts Institute of Technology, Civil and Environmental Engineering, 77 Massachusetts Avenue, 1-290, Cambridge, MA 02139, United States of America
[2]Faculty of Civil Engineering and Geosciences, Delft University of Technology, Delft, The Netherlands
[3]von Karman Institute for Fluid Dynamics, 1640 Sint-Genesius-Rode, Belgium
[4]Department of Earth and Environmental Sciences, KU Leuven, Belgium
[5]ENGIE Laborelec, 1630 Linkebeek, Belgium

Correspondence: s.p.porchetta@tudelft.nl

Abstract. With the rapid increase in wind farm developments, it is essential to evaluate the impacts of newly constructed wind farms on adjacent wind farms, both existing and planned. Numerical weather prediction models are essential tools to predict wake effects, especially under varying atmospheric conditions that occur throughout the year. In this study, we investigate the annual variation of wake effects caused by the planned, Belgian Princess Elisabeth (PE) wind farm cluster on adjacent, existing wind farms in the Southern North Sea. To represent the annual variation, a simulation of a representative year is performed with the Weather Research and Forecasting (WRF) model. The analysis focuses on how variability in atmospheric conditions influences wake interactions throughout the year, which is important for wind farm planning and operational strategies. A distinction is made between external wake energy losses, caused by the new wind farm cluster, and internal wake energy losses, caused by the individual wind farms within the existing area. The diurnal variations in external wake energy losses are driven by changes in atmospheric stability, while the seasonal variations are largely a consequence of seasonal variations in wind direction, wind speed and atmospheric stability. In contrast, internal wake energy losses are mainly determined by seasonal patterns and show only weak diurnal variability. The spatiotemporal averaged external wake energy losses are limited to 4%, while the internal wake energy losses can reach 42% for the closest adjacent BE-NL wind farm. The spatial distribution of wake losses further reveals that turbines located in the center of a wind farm experience higher internal wake energy losses, especially in densely packed layouts, while those at the edges are less affected for internal wake energy losses but more for external wake energy losses. Both the internal and external energy losses decrease with increasing atmospheric instability when wind speeds are in region II of the wind turbine's power curve where wind turbine operation maximizes coefficient of power. When binning for wind speed and wind direction, stable stratification results in external wake losses that are approximately twice as large as in unstable stratification. The presence of the new wind farm cluster also leads to episodes of negative wake energy losses, implying power gain after the construction of the PE wind farm cluster, which are related to flow speed-up around the new wind farm. This paper constitutes Part I of a two-part study. In Part II, the impacts induced by the PE wind

farm cluster are evaluated using fast-running engineering wake models and compared against the WRF results presented here, allowing for a systematic assessment of differences and uncertainties between models.

1 Introduction

Wind energy holds significant potential as a primary contributor to meet the growing demand for clean energy in the global community, with the expectation that wind energy will account for up to one-third of the global energy supply by 2050 (Veers et al., 2019). Following the signing of the Ostend Declaration in April 2023, Belgium, Germany, Denmark and the Netherlands have committed to deliver 65 GW of offshore wind by 2030, illustrating the exponential growth that one can expect in development areas such as the North Sea. As the deployment of wind farms continues to accelerate, leading to lower distance in between wind farms, it becomes crucial to investigate interactions between neighboring wind farms. Wind farms create wakes, which are regions of mean momentum and kinetic energy deficit downwind of the turbines (Fischereit et al., 2022b). These wakes can extend over large distances (Platis et al., 2018; Schneemann et al., 2020) and influence the power production of downwind wind farms (Lundquist et al., 2019; Barthelmie et al., 2010; Pryor et al., 2021; Stieren and Stevens, 2022).

A variety of numerical models have been employed to examine these farm-[illegible] the significance of studying wakes within a mesoscale (or numerical weather prediction) model framework has gained prominence (Cuevas-Figueroa et al., 2022). Mesoscale models are particularly valuable for their ability to incorporate the influence of multiple atmospheric variables, which may exhibit non-uniform spatial and temporal distributions. However, it is important to note that typical horizontal resolutions in mesoscale models for wind energy research mostly range from 1 to 3 km, which is larger than the spacing between the wind turbines (Fischereit et al., 2022a). However, horizontal resolutions of 333 m and 5 km are also possible (Prosper et al., 2019).

To account for subgrid scale effects of wind turbines which are not explicitly resolved by the model, wind farm parameterizations are employed within mesoscale models (Veers et al., 2019). Here, wind turbines are typically parameterized as momentum sink and turbulence kinetic energy source within the planetary boundary layer. A widely used scheme is the Fitch parameterization (Fitch et al., 2012), which represents the extracted momentum by a single wind turbine based on the turbine thrust curve and the added turbulent kinetic energy is proportional to the difference between the thrust and power coefficients. This allows the model to account for both the wake velocity deficit and the enhanced mixing caused by turbine-induced turbulence. Other wind farm parameterizations focus on further elaborating on this parameterization by tuning model coefficients or incorporating additional physical effects such as wind shear, turbine layout, etc. (Redfern et al., 2019; Pan and Archer, 2018). Over the years, these different wind farm parameterizations have been developed and implemented in mesoscale models to investigate a wide range of questions. These investigations, employing different wind farm parameterizations, have included studying the effects of wind veer and shear using the rotor equivalent wind speed model (Redfern et al., 2019), wind-waves and swell (Porchetta et al., 2021), wind farm layout (Pan and Archer, 2018), and model resolution (Pryor et al., 2020), among others on the power production and wakes of wind turbines.

Until recently, mesoscale wake studies have predominantly focused on limited time periods that are insufficient to directly assess annual mean wake effects or sub-annual wake variability. These shorter time periods were often chosen because of the high computational cost associated with long-term simulations. However, with increasing computational resources, it is becoming more common to perform simulations over full years or longer (Palatos-Plexidas et al., 2025). For example, earlier studies approached seasonal variability by using representative subsets of data. Pryor et al. (2021) investigated eleven 5-day periods in order to represent seasonality. A similar approach was used by Fischereit et al. (2020) where 180 days were selected to represent the wind and wave climate to investigate the wind-wave-wake interactions of wind farms in the North Sea. More recently Borgers et al. (2024) investigated farm-farm wakes for one year for different wind farm density scenarios for planned wind farm locations in the North Sea. Their findings revealed that farm-farm wakes are highly sensitive to capacity density, inter-farm spacing, and wind farm sizes. In addition, Akhtar et al. (2021) simulated the wake impacts in the North Sea over multiple years, however, both Akhtar et al. (2021) and Borgers et al. (2024) employed similar wind turbines over the full area and did not account for the actual type of installed/planned wind turbines. These theoretical studies can provide useful insight into the importance of farm-farm interactions but are less relevant to quantify the effect of future planned wind farm clusters on the actual adjacent existing wind farms, as these studies do not consider the actual wind farm characteristics. In contrast, Cuevas-Figueroa et al. (2022) investigated farm-farm interaction of an operational farm for shorter periods of time, and stated that yearly runs are still computational expensive. Borgers et al. (2025) simulated a realistic 92 GW North Sea wind farm expansion scenario with COSMO-CLM and found that inter-farm wakes could reduce annual energy production by more than 10% at several sites, with the Princess Elisabeth zone causing power reductions exceeding 15% during certain high wind 24 hour periods. Lastly, Rosencrans et al. (2024) studied the sub-annual variability of offshore wind deployments in the mid-Atlantic and observed monthly and daily fluctuations in power deficits resulting from farm-farm interactions. They also showed the non negligible effect of farm-farm interactions. It is clear that there is a growing interest on farm-farm interaction in numerical weather prediction models for periods that resolve seasonal variations.

In this study, we aim to investigate annual averaged wake effects and sub-annual wake variability of a newly planned wind farm cluster on adjacent existing wind farms. We predict these effects using a numerical weather prediction model namely the Weather Research and Forecasting (WRF) model (Skamarock et al., 2008). More specifically, the effect of the new Princess Elisabeth (PE) wind farm cluster which will be built in the near future in the Belgian part of the North Sea, will be investigated. We simulate a year in which the annual wind climate is very similar to the wind climate of 1990-2020, allowing us to examine the most typical wake effects on the existing neighboring wind farms, which are important for the operations of the latter. Furthermore, this study focuses solely on the most commonly used wind farm parameterization despite the knowledge that certain parameterizations parameters perform better under specific conditions. The primary objective of this study is to offer insights into the annual wake impact and its sub-annual variability for one of the main offshore wind energy development hotspots, using the most commonly employed, out-of-the-box wind farm parameterization within WRF. We seek to quantify the determinants of the wind farm wake effects on neighboring wind farms, considering wind speed, wind direction, and atmospheric stability over an annual period.

This paper constitutes Part I of a two-part study investigating wake impacts of an offshore wind farm clusters. In Part II, the wake impacts induced by the Princess Elisabeth wind farm cluster are evaluated using fast-running engineering wake models and compared against the numerical weather prediction results presented here, allowing for a systematic assessment of model approach differences and uncertainty in long term farm-farm wake estimates.

2 Material and methods

The materials and methods presented in this section are applied to the new Princess Elisabeth (PE) wind farm cluster and existing adjacent wind farms. The same methodology can be extrapolated to study other farm-farm interactions.

2.1 Study area and period

Within the southern portion of the North Sea, a new wind farm cluster, the Princess Elisabeth cluster (PE) (red dots in Fig. 1), will be built. Although the final installed capacity is still under discussion, ranging from 3.15 GW to 3.5 GW, only one possible wind farm scenario (Munters et al., 2022) will be considered in this study, corresponding to a newly installed capacity of 3.5 GW with 15 MW turbines with a rotor diameter of D=236 m and a hub height of z_h =146 m. While we investigate the impact of the new wind farm cluster on all neighboring farms, the impact on the Belgian-Dutch (BE-NL) wind farm cluster, located just downstream of the prevailing southwesterly wind direction, is the primary focus in this study. However, as other nearby wind farms are likely to be affected (Lundquist et al., 2019; Barthelmie et al., 2010; Pryor et al., 2021; Stieren and Stevens, 2022), they are also considered in the numerical weather prediction model of this study (Fig. 1). In total, the influence of the Princess Elisabeth wind farm zone on 1409 wind turbines is investigated. The turbines are modeled in the numerical simulations with the appropriate turbine manufacturer curves or approximations thereof (Pierrot, 2024; EMD International A/S). The locations of the existing wind turbines are extracted from Hoeser et al. (2022), while the locations for the new Princess Elisabeth wind farm are from Munters et al. (2022) and Cornillie et al. (2021). The latter layout results from a preliminary distribution of turbines over the lease area, accounting for a known exclusion zone, without delving into the specifics of micrositing based on sea surface topography.

The simulations are performed for the year 2016 as it is a representative year for the long-term wind climate at 100 m above mean sea level for the study area. This was determined based on the methodology outlined in Borgers et al. (2024), based on hourly ERA5 data for the period 1990-2020. This methodology identifies a representative year by comparing the wind speed and wind direction distributions for a single year with the long-term distributions. The goal of using a representative year is so that this study can provide an appropriate basis for long-term representation of the influence of building the new Princess Elisabeth wind farm cluster close to the neighbouring wind farms.

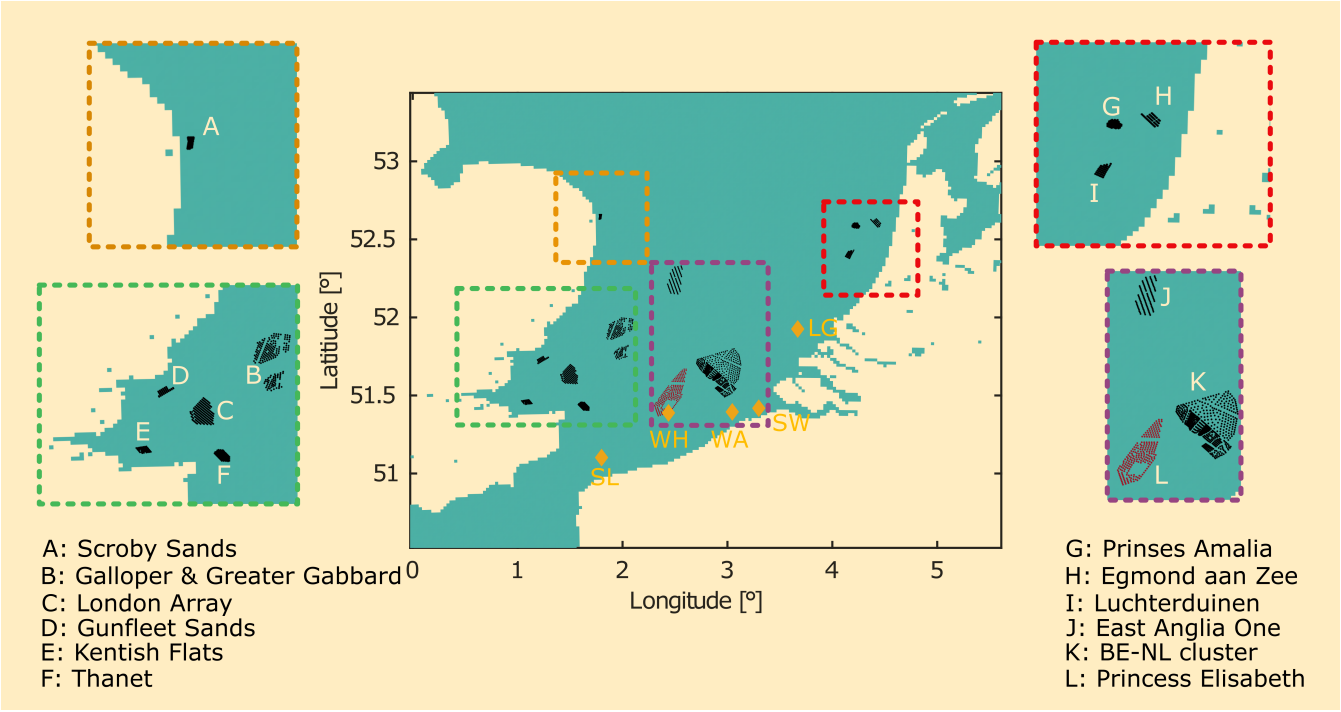


Figure 1. Location of the new Princess Elisabeth wind farms (red dots) and the existing wind farms (black dots) within the southern North Sea. Yellow diamonds show the location of measurement masts, with further details found in Table 1.

2.2 Observation stations

The simulation results are compared with offshore measurements. For the year 2016, 5 measurement platforms (yellow diamonds Fig. 1, Table 1) measured wind speed and wind directions at different altitudes and with a temporal resolution of 10 minutes (Borgers et al., 2024). These measurements were taken by boom- or platform-mounted anemometers, wind vanes or a LiDAR. At the location of Wandelaar both anemometers and vanes are present, while at Lichteiland-Goeree both an anemometer and a LiDAR are present. Table 1 also shows the uncertainty of the wind speed measurements including the uncertainty of the calibration, mounting, data acquisition and local site conditions (Borgers et al., 2024). For wind direction the measurement uncertainty is not known. Furthermore, Table 1 indicates the recovery rate at each observational mast.

Table 1. Observational mast name, location, measurement altitude, uncertainty of the wind speed measurements and recovery rate for 2016.

Observational mast	Longitude	Latitude	Height [m]	Uncertainty [%]	Recovery rate [%]
Westhinder (WH)	2.4378° E	51.3883° N	26	5.6	98.30
Wandelaar US (WA)	3.0458° E	51.3945° N	26	3.3	35.55
Wandelaar vane (WA)	3.0458° E	51.3945° N	26	3.3	97.04
Scheur-Wielingen (SW)	3.2985° E	51.4183° N	25	3.3	96.23
Sandettie-Lightship (SL)	1.800° E	51.102° N	14	3.3	92.5
Lichteiland-Goeree (LG)	3.67° E	51.9258° N	38	3.3	98.29
Lichteiland-Goeree (LG) LiDAR	3.67° E	51.9258° N	62 - 290	3.3	99.46 - 92.63

2.3 Mesoscale model setup

The numerical model used is the Weather Research and Forecasting (WRF) model v4.3 (Skamarock et al., 2008) with three nested domains (150 × 150, 190 × 190 and 220 × 190 grid cells) with a horizontal grid spacing of 18 km for the outermost domain, 6 km for the middle domain and 2 km for the innermost domain (Fig. 2), following the recommendation of Fischereit et al. (2022a). The vertical resolution has 80 vertical levels which are stretched, resulting in more levels close to the surface, and follows the recommendations of Lee and Lundquist (2017). Within the first 150 m there are approximately 15 vertical levels. The model top is located at 1000 Pa. The Global Multi-resolution Terrain Elevation Data (GMTED2010) is imposed for the geographical data with a resolution of 30 arcseconds. The initial and lateral boundary conditions come from the ERA5 reanalysis data set provided by the European Centre for Medium-Range Weather Forecast (Hersbach et al., 2018a, b), which have a 0.25° x 0.25° horizontal grid resolution, 1 h temporal resolution, and 37 pressure levels up to 1 hPa. The physical parameterizations in this study are based on previous studies for similar applications in the same geographical region (Table 2) (Siedersleben et al., 2020; Porchetta et al., 2020, 2021). The parameterizations are a double-moment microphysics scheme (Morrison et al., 2005), the long and short wave Rapid Radiative Transfer Model for General Circulation Models (RRTMG) (Iacano et al., 2008), the revised MM5 surface layer scheme (Jiménez et al., 2012), the Noah land surface scheme (Tewari et al., 2004), the Kain-Fritsch cumulus scheme (Kain, 2004) (only applied to the parent domain as the two innermost domains have a convective permitting resolution) and the Mellor-Yamada Nakanishi Ninno (MYNN) planetary boundary layer scheme (Nakanishi and Niino, 2006). When wind turbines are included, the parameterization of Fitch et al. (2012) is used with a turbulent kinetic energy generation parameter of 0.25, which currently is the default value used in WRF (Archer et al., 2020).

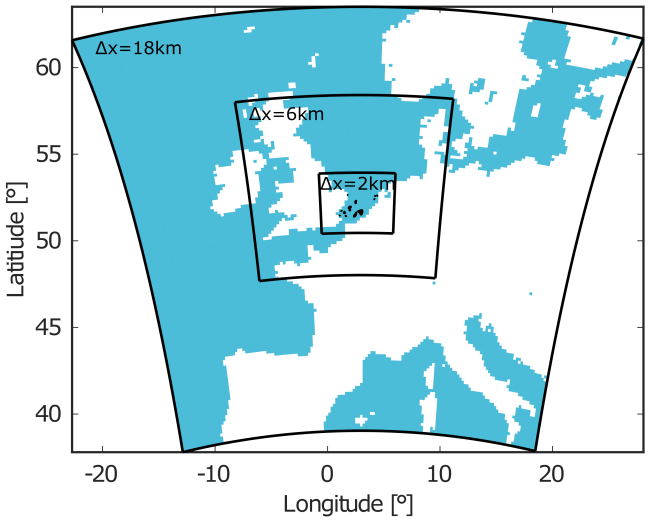


Figure 2. The WRF computational configuration with 3 nested domains with a horizontal grid spacing of 18 km, 6 km and 2 km for the outer to the innermost domain. The innermost domain shows all wind farm clusters included in the simulations (see Fig.1 and Table 1 for details).

Table 2. Parameterizations used in the WRF simulations.

Physics	Parameterization	Reference
Microphysics	double-moment	Morrison et al. (2005)
Short and long wave radiation	RRTMG	Iacano et al. (2008)
Planetary boundary layer	MYNN	Nakanishi and Niino (2006)
Surface layer	revised MM5	Jiménez et al. (2012)
Land surface	Noah	Tewari et al. (2004)
Cumulus	Kain-Fritsch	Kain (2004)
Wind farm	Fitch	Fitch et al. (2012)

Three simulations for the year 2016 are performed, a first one where no wind farms are included, which is used as a reference simulation. One simulation with only the existing wind farms in 2022 (black dots Fig. 1, see Appendix A) and one simulation with the existing wind farms in 2022 and the new Princess Elisabeth wind farm cluster (black and red dots Fig. 1). The names of these three simulations throughout the paper will be referred to as, 'no WF', 'without PE' and 'with PE' respectively. The simulations including wind turbines (without PE and with PE) have exactly the same set-up as the no WF setup, grid size and employed parameterizations except for the additional wind farm parameterization.

2.4 Stability classification

Because atmospheric stability has significant effects on the wakes of wind turbines (Platis et al., 2022; Rosencrans et al., 2024; Wu et al., 2023), it is important to investigate how the wake impacts of the new PE wind farm are influenced by different atmospheric stability regimes. The atmospheric stability in this work is defined by the Monin-Obukhov length (L), which categorizes atmospheric stability based on the ratio of turbulence production by mechanical shear to turbulence production by buoyancy associated with the surface layer (Monin and Obukhov, 1954). The different stability classes based on L are shown in Table 3. This classification is proposed by Van Wijk et al. (1990) and has been utilized in various studies (Porchetta et al., 2019; Nybø et al., 2020; Platis et al., 2022; Howland et al., 2022). The Monin-Obukhov length is output at every 10-minute time interval by WRF and is calculated by the surface layer scheme (Jiménez et al., 2012). A stability classification based on the bulk Richardson number between model levels at 10 and 100 m produced similar results, showing a Pearson correlation of 72% with the Monin–Obukhov length classification. Consequently, only the Monin–Obukhov length method is applied in the following analyses.

Table 3. Atmospheric stability classification based on the Monin-Obukhov length (L).

Stability class	Range of L
Very stable	0 L < 200
Stable	200 ≤ L < 1000
Near neutral	1000 ≤ $\|L\|$
Unstable	-1000 < L ≤ -200
Very unstable	-200 < L 0

2.5 External and internal wake energy loss quantification

In this study, we quantify total wake energy losses and decompose them into internal and external contributions. External wake energy losses are defined as the additional wake-induced energy losses caused by the new PE wind farm cluster on the existing wind farms. Internal wake energy losses, as defined here, represent the wake energy losses experienced by the existing wind farms in the absence of the PE wind farm cluster. It is important to note that this definition differs from the strict definition of internal wake energy losses, which include only wake effects generated by turbines within the same wind farm. Due to the simulation setup employed in this study, this distinction cannot be made. Consequently, the internal wake energy losses presented here include inter farm wake effects among the existing wind farms, but exclude wake effects originating from the new PE wind farm cluster. Note that these internal wake effects virtually exclusively originate from wind turbines within the dense Belgian-Dutch cluster, as other wind farms included in the without PE simulation are at least 58 km away.

Three different averaging procedures are employed, where N_s is the number of turbines, N_t the number of time steps, and $P_i(t)$ the instantaneous power output of turbine i at time t:

- Temporal average: $\overline{P}_i = \frac{1}{N_t} \sum_{t=1}^{N_t} P_i(t)$, i.e., the average over time for turbine-containing grid cells.

- Spatiotemporal average: $\overline{P} = \frac{1}{N_s N_t} \sum_{i=1}^{N_s} \sum_{t=1}^{N_t} P_i(t)$, i.e., averaging across all turbine(s) containing grid cells and time steps simultaneously.
- Spatiotemporal conditional average: $\overline{P}_{\text{spatio-bin}} = \frac{1}{N_{\text{bin}}} \sum_{i,t \in \text{bin}} P_i(t)$, considering only specific conditions such as wind speed, wind direction, atmospheric stability, or a combination of the previous.

The absolute internal wake energy loss is defined in Eq. (1) as the power reduction of the reference power (no WF) associated with the existing wind farms only (without PE). The reference power $\overline{P}_{\text{noWF}}$ is obtained by sampling the hub-height wind speed from the no WF WRF simulation at each turbine location and converting it to power using the turbine power curves. The total (internal + external) absolute wake energy loss is defined in Eq. (2) as the difference between the reference power and the mean power obtained in the presence of both the existing wind farms and the PE cluster (with PE). The absolute external wake energy loss induced by the PE wind farm cluster is defined in Eq. (3) as the difference between the total and internal losses:

$$\Delta\overline{P}_{\text{internal}} = \overline{P}_{\text{noWF}} - \overline{P}_{\text{withoutPE}}, \tag{1}$$

$$\Delta\overline{P}_{\text{internal+external}} = \overline{P}_{\text{noWF}} - \overline{P}_{\text{withPE}}, \tag{2}$$

$$\Delta\overline{P}_{\text{external}} = \Delta\overline{P}_{\text{internal+external}} - \Delta\overline{P}_{\text{internal}} = \overline{P}_{\text{withoutPE}} - \overline{P}_{\text{withPE}}. \tag{3}$$

From the absolute wake energy losses defined in Eqs. (1)–(3), the corresponding percentage wake energy losses are obtained by normalization with the reference power $\overline{P}_{\text{noWF}}$. The percentage internal wake energy loss is defined in Eq. (4) as the relative power reduction associated with the existing wind farms only (without PE), normalized by the reference power. The total (internal + external) percentage wake energy loss is defined in Eq.(5) as the relative power reduction in the presence of both the existing wind farms and the PE cluster (with PE), normalized by the reference power. The percentage external wake energy loss induced by the PE wind farm cluster is defined in Eq. (6) as the difference between the total and internal percentage losses:

$$\text{Loss}_{\text{internal}} = 100 \times \frac{\Delta\overline{P}_{\text{internal}}}{\overline{P}_{\text{noWF}}}, \tag{4}$$

$$\text{Loss}_{\text{internal+external}} = 100 \times \frac{\Delta\overline{P}_{\text{internal+external}}}{\overline{P}_{\text{noWF}}}, \tag{5}$$

$$\text{Loss}_{\text{external}} = 100 \times \frac{\Delta\overline{P}_{\text{external}}}{\overline{P}_{\text{noWF}}}. \tag{6}$$

All (absolute or percentage) wake energy losses are computed from the averaged power values defined above, rather than from instantaneous (absolute or percentage) losses at individual time steps. As described earlier, these losses (internal, external, and total), will be analyzed using temporal, spatiotemporal, and spatiotemporal conditional averages to further elucidate the drivers of the interactions between turbines and farms. Throughout this manuscript, the term wake energy losses refers to the percentage definitions given in Eqs. (4)–(6), unless explicitly stated as absolute wake energy losses, in which case the definitions of Eqs.(1)–(3) are used.

In addition to wake energy loss metrics, annual energy production (AEP) is computed by integrating the power of the turbines power over the full simulation period. AEP is calculated separately for the without PE and with PE simulations and AEP losses are reported as a relative change between these two cases. In contrast to the wake energly loss definitions above, AEP changes are normalized by the baseline production of the existing wind farms, without PE, rather than by the noWF reference.

3 Results and discussion

Throughout this manuscript, the results are shown on grid cells which refers to single horizontal WRF model grid cells. As multiple turbines may fall within one grid cell, all wind farm quantities evaluated at the grid cell level (e.g., power or wake energy losses) represent aggregated model responses rather than turbine resolved values.

3.1 WRF validation

We first seek to establish confidence in the WRF model representation of the wind field. The simulations in this study represent idealized scenarios, as only a few of the Belgian-Dutch wind farms (Thorntonbank I, II and III, Belwind, and Northwind, 182 of 572 turbines) were operational in 2016, while the existing turbines used in the simulations correspond to the wind farm layout as of [illegible] year 2016 was nevertheless selected because it was identified as the most meteorologically representative. As a consequence of this mismatch between the meteorological year and the wind farm layout, a true validation of wake energy losses is not possible. As such, validation will only become feasible once post-construction field observations for the fully developed wind farm area become available (Palatos-Plexidas et al., 2025). Future research may then also explore the optimal representation of the wind field by selecting the most appropriate model configuration and parameterizations.

Although optimizing the model setup through an extensive sensitivity study is beyond the scope of this work and has already been addressed elsewhere (Hahmann et al., 2014; Siedersleben et al., 2020; Tomaszewski and Lundquist, 2022; Li et al., 2021; Vermuri et al., 2022), it remains essential to assess the performance of the simulated flow fields relevant to this study. For this purpose, wind speed and wind direction from the no WF, without PE, and with PE simulations are compared against observations at five different locations (Table 1). The mean bias (simulated minus observed) is reported in Tables 4 and 5 for both wind speed and wind direction.

The validation of the ambient wind estimation largely focuses on the no WF case because the inclusion of wind farms in the simulation causes wakes at the observational mast locations, thus deviating from the observed values, where only a few turbines generated wakes in 2016. This is especially visible at the location of WH while the location in SL is less affected by

wakes (smaller differences between the different simulations no PE, without PE and with PE). For the latter, this is the case since the main wind direction in this area of the North Sea is dominated by southwesterly winds (Ivanova et al., 2023).

The bias in the simulation without wind farms (no WF) is relatively small, ranging from −0.95 to 0.66 ms^{-1} for wind speed and −9.85 ° to 13.71° for wind direction. This falls within the range reported in previous studies on offshore wind fields (Rosencrans et al., 2024; Fischereit et al., 2022b; Borgers et al., 2024; Li et al., 2021). Examining specific observation locations, namely WH, SL, and LG, the wind speed predicted by WRF tends to underestimate observed values offshore, consistent with findings by Li et al. (2021), Rosencrans et al. (2024) and Borgers et al. (2024). In contrast, at WA and SW, closer to the coast, the WRF model tends to overestimate wind speed (Hahmann et al., 2014), suggesting a potential coastal effect not well captured by WRF. Due to the relatively coarse coastal resolution, WRF sees a longer fetch which results in higher wind speeds in the model (Hahmann et al., 2014). No clear trend is evident in the no WF biases concerning the altitude of the measurement masts considered, except that the highest observation point exhibits the lowest bias, similar to Klemmer et al. (2024), but opposite to Munoz-Esparza et al. (2012) and Sward et al. (2023).

When comparing all three simulations (no WF, without PE, and with PE), the strongest wake related deviations appear at WH, WA, and SW, where the inclusion of wind farms leads to a significant change in bias compared to the no WF case. At LG, which is located downwind, some differences between the three simulations can also be linked to wake effects. At WH the differences between the simulation no WF and without PE are within the uncertainty range (95 % confidence interval which accounts for both model variability and, when available, measurement uncertainty, see Appendix Section C), while the wake effect of the new PE is clearly present in the wind speed bias with PE. At SL, where wakes are not expected to play a large role, the biases are nearly identical across the three simulations. This indicates that the background flow is consistently reproduced in all simulations, providing confidence in the subsequent wake energy loss analysis.

The LiDAR at LG was designed specifically for assessing offshore wind resources. It provides vertical wind profiles up to 215 meters, enabling model evaluation at heights comparable to the level of turbine hub heights. Comparing the different WRF simulations with the LiDAR observations (Table 3) reveals a small mean bias across all altitudes and different simulation. The bias for wind speed ranges from 0.04 ms^{-1} at 62 m to –0.10 ms^{-1} at 215 m in the no WRF simulation, from -0.08/-0.07 ms^{-1} at 62 m to -0.22/-0.23 ms^{-1} at 215 m in the without PE simulation and with PE simulation, respectively. Wind direction biases gradually decrease with height, ranging from values around 5° at 62 m to around 1.5° at 215 m. This suggests improved directional agreement at higher altitudes. The mean wind speed and direction bias of different simulations often fall within the observational uncertainty, accounting for model variability and LiDAR measurement error, especially between without PE simulation and with PE simulation. Larger differences are observed when comparing to the no WF simulation, this could be caused by wakes. To conclude, the background wind field can be assumed to be similar across simulations, and justify studying the wake effects in the suggested simulations. Overall, based on all observation comparisons, a good agreement between modeled and observed values at hub height supports using WRF to evaluate wake impacts of the newly built PE on existing wind farms.

Table 4. Mean wind speed [ms^{-1}] and wind direction [°] bias (simulation – observations) at LG and the 95% confidence interval, which accounts for both model variability and when available measurement uncertainty, for the no WF WRF, without PE and with PE simulations at the five different observation locations (Table 1).

	Wind speed bias [m s^{-1}]			Wind direction bias [°]		
Observational mast	**no WF**	**without PE**	**with PE**	**no WF**	**without PE**	**with PE**
Westhinder (WH)	-0.33 ± 0.04	-0.37 ± 0.04	-1.14 ± 0.04	13.71 ± 0.53	13.09 ± 0.53	12.96 ± 0.54
Wandelaar (WA) US	0.14 ± 0.06	-0.02 ± 0.07	-0.05 ± 0.07	-9.85 ± 1.26	-10.42 ± 1.30	-11.15 ± 1.30
Wandelaar (WA) vane	0.29 ± 0.04	0.19 ± 0.04	0.13 ± 0.04	11.57 ± 0.55	10.50 ± 0.56	10.53 ± 0.56
Scheur–Weilingen (SW)	0.66 ± 0.03	0.60 ± 0.04	0.58 ± 0.03	9.24 ± 0.56	8.42 ± 0.57	8.40 ± 0.56
Sandettie–Lightship (SL)	-0.95 ± 0.27	-0.94 ± 0.27	-0.94 ± 0.27	9.14 ± 4.05	9.33 ± 4.07	9.43 ± 4.11
Lichteiland–Goeree (LG)	-0.06 ± 0.04	-0.17 ± 0.04	-0.16 ± 0.04	2.10 ± 0.53	1.57 ± 0.54	1.49 ± 0.53

Table 5. Mean wind speed [ms^{-1}] and wind direction [°] bias (simulation minus observations) and the 95% confidence interval, which accounts for both model variability and when available measurement uncertainty, for the no WF WRF, without PE, and with PE simulations at different altitudes of the LG LiDAR location (Table 1).

	Wind speed bias [m s^{-1}]			Wind direction bias [°]		
Altitude [m]	**no WF**	**without PE**	**with PE**	**no WF**	**without PE**	**with PE**
62	0.04 ± 0.04	-0.08 ± 0.04	-0.07 ± 0.04	5.77 ± 0.32	5.49 ± 0.33	5.10 ± 0.32
90	0.03 ± 0.04	-0.09 ± 0.04	-0.08 ± 0.04	5.06 ± 0.32	4.81 ± 0.33	4.39 ± 0.32
115	0.01 ± 0.04	-0.12 ± 0.04	-0.11 ± 0.04	4.29 ± 0.32	4.09 ± 0.33	3.78 ± 0.32
140	-0.01 ± 0.04	-0.14 ± 0.04	-0.13 ± 0.04	3.43 ± 0.32	3.45 ± 0.33	3.10 ± 0.32
165	-0.04 ± 0.04	-0.17 ± 0.04	-0.16 ± 0.04	2.63 ± 0.32	2.63 ± 0.33	2.52 ± 0.32
190	-0.07 ± 0.04	-0.19 ± 0.04	-0.19 ± 0.05	1.98 ± 0.32	1.90 ± 0.33	1.90 ± 0.32
215	-0.10 ± 0.05	-0.22 ± 0.05	-0.23 ± 0.05	1.53 ± 0.33	1.60 ± 0.34	1.50 ± 0.33

3.2 AEP losses compared to spatiotemporal averaged internal and external wake energy losses

The annual energy production (AEP) and mean yearly wind speed deficit before (top row Fig. 3) and after constructing the new Princess Elisabeth wind farm cluster (middle row Fig. 3) are shown in Fig. 3. The wind speed deficit at the mean hub height (96 m) of the wind farms is defined as the temporally averaged wind speed of the simulation, which could be with or without PE, minus the temporally averaged wind speed of the no WF simulations. The bottom row of Fig. 3 shows the effect of constructing the new Princess Elisabeth wind farm cluster. The wind farm cluster most affected by the new PE wind farm cluster is the Belgian-Dutch (BE-NL) wind farm cluster (Fig. 1), with differences in Annual Energy Production (AEP) up to 14% at certain grid cell locations and 5% spatially averaged over the wind farm cluster (Table 6). This effect is primarily due to the

proximity of this cluster to the Princess Elisabeth wind farms and its downstream location for the main wind direction, which is southwesterly (Ivanova et al., 2023). The BE-NL cluster experiences the most significant impact, but smaller effects are also observed for wind farms further away. For instance, a wind farm located at a distance of 181 km exhibits a small AEP loss of 0.12%. While the 95% confidence interval does not include zero, such a small value is unlikely to represent a physical wake impact and is more probably explained by numerical variability of the WRF simulations. It is important that further research investigates these small wake impacts and assesses whether such small deviations hold physical or economic significance. The observed impact over distances underscores the importance of factoring in AEP losses for existing and planned wind farms, both nearby and more distant farms, in future siting decisions and yield assessment. This consideration becomes increasingly crucial as the density of offshore wind farms is projected to increase in the coming years (Borgers et al., 2024). It should also be noted that very small increases (0.11-0.15%) in AEP are seen for three wind farms after the construction of the PE wind farm. Given the low magnitude and the fact that these occur at only three locations, it is difficult to draw any strict conclusions regarding actual increases in AEP. These increases in AEP may be attributable to numerical variability, possibly related to coastal effects or model variability in WRF, and further research would be needed to determine whether they have physical (flow speedup) or economic significance.

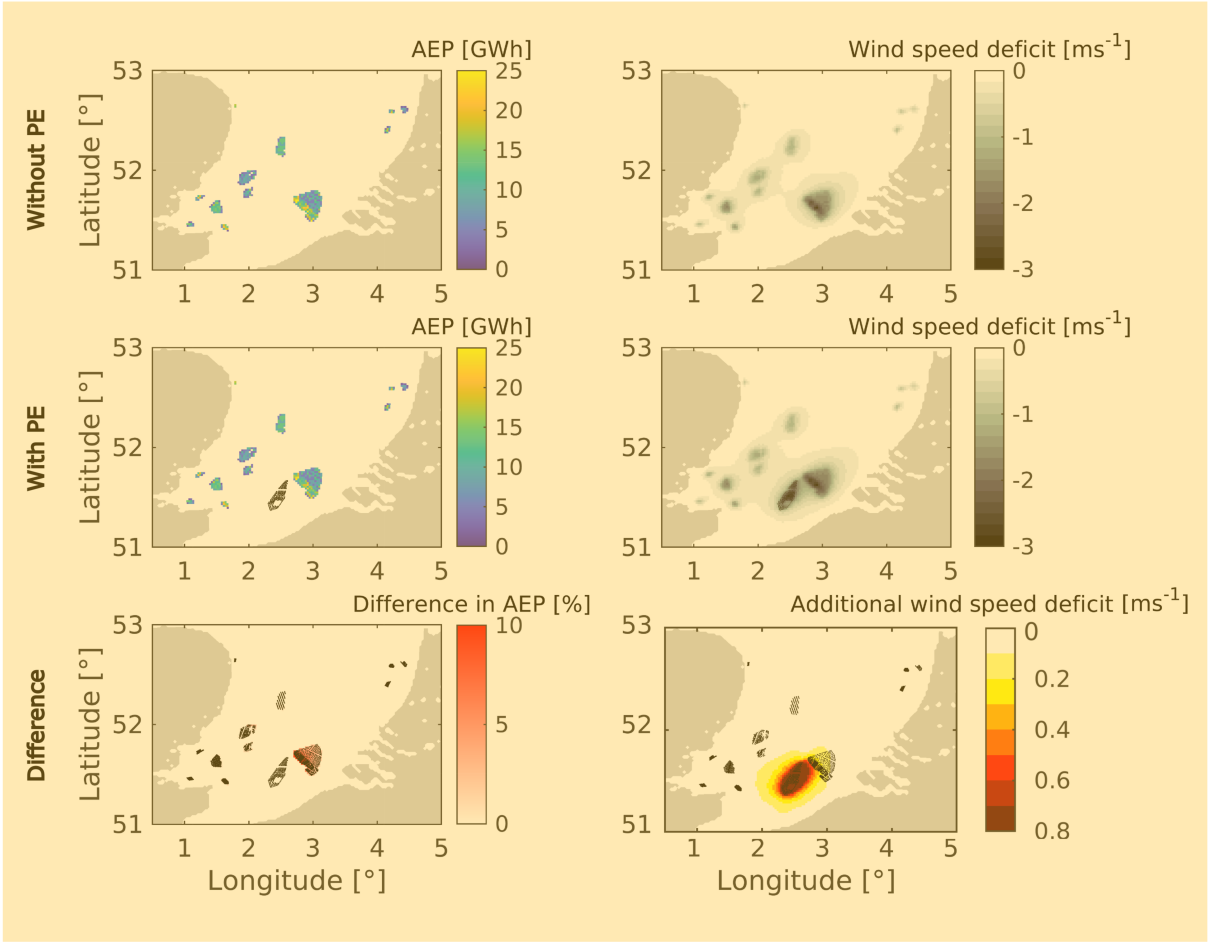


Figure 3. Annual energy production (left column) and temporally averaged wind speed deficit (right column) before (top row) and after (middle row) the construction of the PE wind farm cluster. The bottom row shows the difference between the two.

Due to the presence of the new PE wind farm cluster, wind deficits are intensified (maximum deficit increasing from 2.7 to 2.9 ms^{-1}) and spread over a larger region (Fig. 3). This effect is attributed to the increased momentum extraction of the 15 MW turbines planned for the PE wind farm cluster. The wind speed deficit exerts the strongest influence in the wake in the main wind direction, which is southwesterly (Ivanova et al., 2023). However, wind speed deficits are also observed southwest of the PE farms and extend toward the northwest of the future concession. These wind speed deficits contribute to changes in AEP, although the relationship between wind speed reduction and power loss is not strictly proportional, as power production depends nonlinearly on wind speed. This nonlinearity has also been highlighted in recent studies on cluster wake-induced energy losses (Xia et al., 2025). Consequently, regions experiencing the strongest wind speed deficits generally correspond to areas of larger AEP losses, but even small changes in wind speed may produce disproportionately larger or smaller impacts on AEP depending on the turbine operating regime. It is also important to note that the wind speed deficits mentioned here are

temporally averaged (annual) deficits, and their strength and direction are strongly dependent on wind direction and stability, as discussed in the following sections. Previous work showed that it is less dependent on the TKE coefficient (Rosencrans et al., 2024).

Table 6. Distance to the PE wind farm cluster (center-to-center), spatially averaged AEP loss over each wind farm (with ±95% confidence interval from 1000 bootstrap resamples), and the spatial maximum AEP loss within each farm.

Wind farm	Distance to PE [km]	Spatially averaged AEP loss [%]	Max spatial AEP loss [%]
BE–NL cluster	34	5.13 ± 0.47	14.35
Scroby Sands	135	-0.15 ± 0.07	-0.22
East Anglia ONE	81	0.07 ± 0.06	0.49
Galloper & Greater Gabbard	54	0.76 ± 0.17	3.92
Gunfleet Sands	89	-0.11 ± 0.03	-0.17
London Array	68	0.50 ± 0.03	0.67
Kentish Flats	95	-0.15 ± 0.03	-0.21
Thanet	58	0.94 ± 0.08	1.19
Luchterduinen	153	0.27 ± 0.05	0.37
Egmond aan Zee	181	0.12 ± 0.03	0.22
Prinses Amalia	170	0.13 ± 0.02	0.15

As shown in Table 7, the internal wake energy losses are larger than the external wake energy losses. Note that internal wake energy losses do not refer to the strict definition of internal wake losses but to the energy losses caused in the absence of the PE wind farm cluster (Section 2.5). For all the simulated wind farms, the internal wake energy losses are greater than 20.99% and reach as high as 42.01% for the BE-NL wind farm cluster. These losses are spatiotemporal averaged wake energy losses. New wind farm deployments at the East Coast of the US, even though with a different configuration, are predicted to have similar order of magnitude internal wake losses using the WRF model (Rosencrans et al., 2024; Rybchuk et al., 2022). It is known that the WRF model with the wind farm parameterization of Fitch (Fitch et al., 2012) can overestimate internal wake power losses because turbine wakes are distributed over grid cells much larger than individual wakes and turbulence generation is also underrepresented (Abkar and Porté-Agel, 2015; Sanchez Gomez et al., 2024). As such, the results shown in Table 7 may be an upper estimate of internal wake energy losses. Future comparisons with operational SCADA could assess this in more detail.

Relative to the internal wake losses, the external wake losses are generally much smaller (Table 7). For several distant wind farms, such as Scroby Sands, East Anglia ONE, Kentish Flats, Egmond aan Zee, Gunfleet Sands, and Prinses Amalia, the confidence intervals overlap zero. This suggests that the apparent external wake effect of the PE cluster on these distant farms is likely not statistically significant and may reflect numerical variability or random fluctuations rather than a true physical

wake effect. In contrast, only closely located farms such as the BE–NL cluster, Galloper & Greater Gabbard, London Array, Thanet, and Luchterduinen, show statistically significant external wake losses.

Table 7. Spatiotemporal averaged external and internal wake energy losses over different wind farms. Uncertainty is reported as the half-width of the 95% confidence interval from 1000 bootstrap resamples.

Wind Farm	External losses [%]	Internal losses [%]
BE–NL cluster	3.96 ± 0.11	42.01 ± 0.28
Scroby Sands	-0.11 ± 0.14	24.04 ± 0.27
East Anglia ONE	0.05 ± 0.10	22.03 ± 0.24
Galloper & Greater Gabbard	0.56 ± 0.09	25.98 ± 0.26
Gunfleet Sands	-0.08 ± 0.11	28.05 ± 0.26
London Array	0.34 ± 0.09	33.58 ± 0.27
Kentish Flats	-0.11 ± 0.13	27.90 ± 0.26
Thanet	0.67 ± 0.12	32.50 ± 0.26
Luchterduinen	0.19 ± 0.13	20.99 ± 0.26
Egmond aan Zee	0.10 ± 0.14	22.82 ± 0.28
Prinses Amalia	0.08 ± 0.13	27.20 ± 0.27

Comparing the external wake energy losses (Table 7) with the AEP losses (Table 6) shows that both tables exhibit similar spatial trends. The BE–NL wind farm cluster, Galloper & Greater Gabbard, London Array, Thanet, and Luchterduinen show the largest impacts, while more distant farms show much smaller effects. Differences between the two tables arise because the metrics are defined using different normalizations. The AEP losses are computed as relative changes between the without PE and with PE simulations and normalized by AEP without PE, whereas the external wake losses are defined as ratios of temporally averaged power normalized by the noWF simulation (Eqs. 4–6). This difference in normalization, together with the implicit weighting of high-production periods in the AEP calculation, explains why some farms show statistically significant AEP impacts while their external wake losses are not statistically significant.

3.3 External wake energy losses as a function of wind direction, wind speed and atmospheric stability

To gain more insight into the atmospheric conditions influencing external wake energy losses (defined in Section 2.3), a more in-depth study of the BE-NL wind farm cluster (Fig. 1 - K) is conducted. This wind farm cluster is investigated because it experiences the largest wake losses. In all following figures we characterize the atmospheric conditions (wind direction, atmospheric stability class and wind speed) based on a reference location (spatial averaged grid cell location of the considered BE-NL wind farm cluster) of the no WF WRF simulation. The height at which the wind speed and direction is taken, is at 96 m altitude, which is the weighted averaged hub height over all wind turbines considered in this work. The error bars in the following figures represent a 95% confidence interval calculated by bootstrapping with 1000 resamples.

In Figure 4 (a), we show the annually averaged external wake energy losses of the BE-NL wind farm cluster caused by the PE wind farm cluster. We also show how this external wake energy effect depends on wind direction (Fig. 4 (b)), stability (Fig. 4 (c)) and wind speed (Fig. 4 (d)). We note that each of these figures (Fig. 4 (b)-(d)) only looks at a single variable in isolation, and does not control for the other variables simultaneously, which can be important due to the inherent correlations between wind direction, wind speed and stability. This means that the patterns in Figure 4 (b)-(d) reflect combined effects rather than the influence of a single variable.

The external wake energy losses are spatially concentrated at the top left corner of the BE-NL wind farm cluster, resulting in external energy wake losses up to 10% at these grid cell locations (Fig. 4 (a)). These high losses are linked to the prevailing southwesterly wind direction of approximately 225°, leading to the highest losses in this part of the cluster, as the new PE wind farm is upstream of the BE-NL cluster for this wind direction (Fig. 4 (b) and 5). For wind directions outside the range where BE–NL is directly in the wake of PE, the new PE wind farm cluster induces small external wake energy losses (Fig. 4 (b)). In some directions negative wake energy losses are observed, which imply a limited power gain after the PE wind farm cluster was constructed. This will be discussed later in the manuscript.

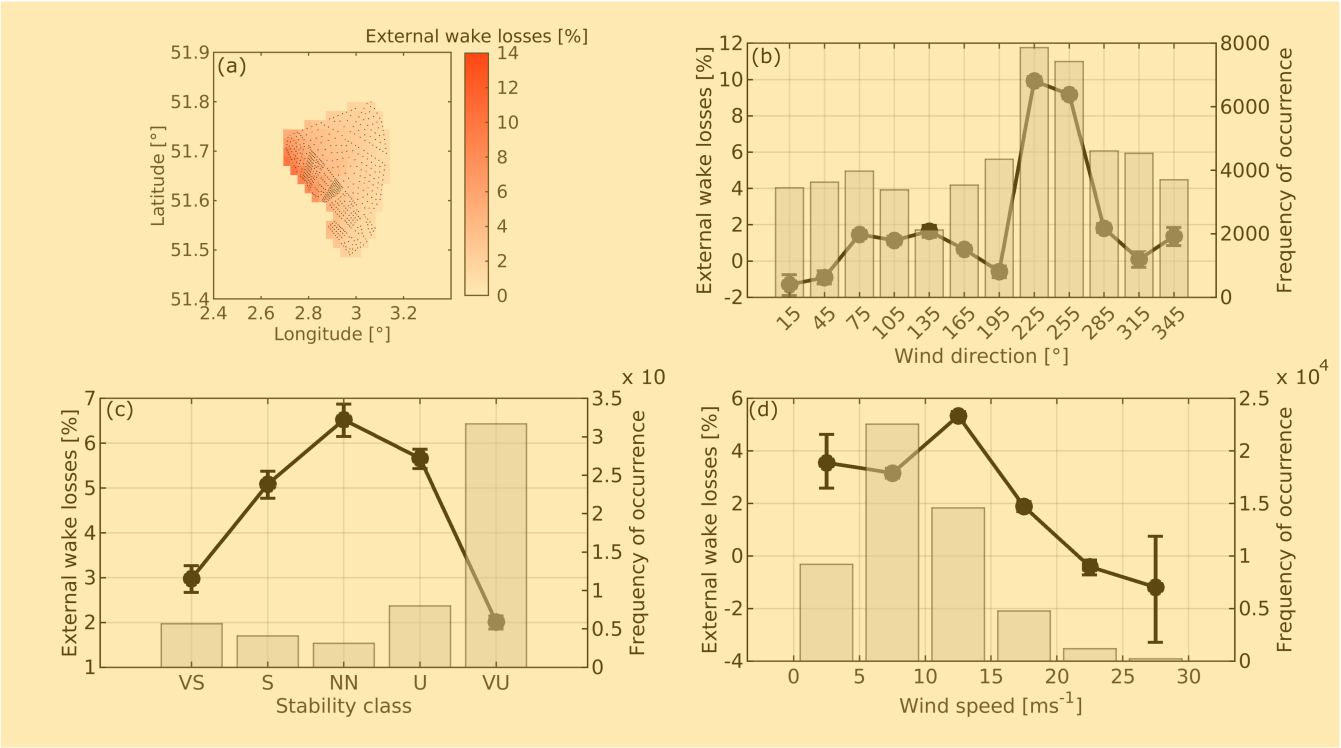


Figure 4. Results are shown for the BE-NL wind farm cluster. (a) Temporal average of external wake energy losses for the BE-NL wind farm. (b) (Line) Spatiotemporal conditional average of external wake energy losses as a function of wind direction, (bars) frequency of occurrence of the different wind directions. (c) (Line) Spatiotemporal conditional average of external wake energy losses as a function of atmospheric stability classes (VS: Very Stable, S: Stable, NN: Near Neutral, U: Unstable, VU: Very Unstable), (bars) frequency of occurrence for the different atmospheric stability classes. (d) (Line) Spatiotemporal conditional average of external wake energy losses as a function of wind speed, (bars) frequency of occurrence of the different wind speeds. The error bars represent a 95% confidence interval obtained via bootstrapping with 1000 resamples.

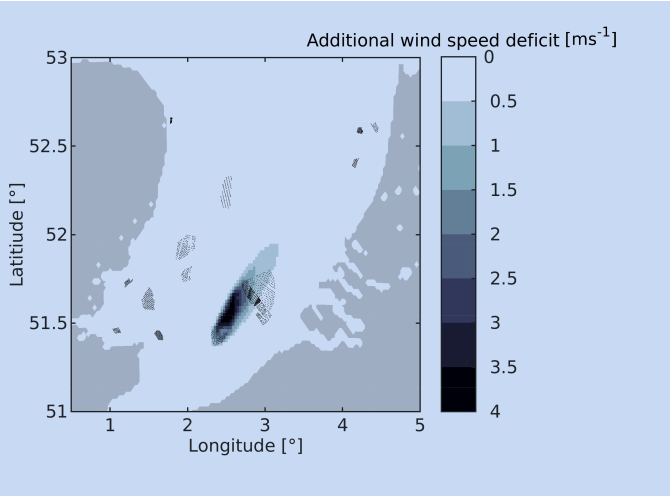


Figure 5. External BE-NL wind farm wake deficit for wind directions between 215 and 235°, which corresponds to the highest external wake losses and the most frequent wind direction. The error bars represent a 95% confidence interval obtained via bootstrapping with 1000 resamples.

Figure 4 (c) shows external wake energy losses as a function of atmospheric stability. In this figure, the highest losses are present for near-neutral conditions. This arises because the figure does not control for wind conditions, and aggregating over all atmospheric situations allows competing effects to cancel or amplify, which obscures the underlying stability dependence. To elucidate how the wake effects depend on stability more clearly, we define a narrow wind direction bin of 193° to 317°. This wind direction bin only includes wind directions for which the BE–NL wind farm cluster is in the wake of the PE wind farm cluster. These results are shown in Fig. 6 and show decreasing external wake energy losses from a very stable to a very unstable atmosphere. The lowest external wake energy losses are present for the most frequently occurring very unstable atmospheric conditions. It has been reported in earlier studies that, for the North Sea, (very) unstable atmospheric conditions are commonly seen (Porchetta et al., 2019; Munoz-Esparza et al., 2012; Nybø et al., 2020). Also at the location of the planned Vineyard wind farm at the East Coast of the US, unstable conditions are present 53.6% of the time (Rosencrans et al., 2024). Stable conditions in the North Sea (BE–NL wind farm cluster) are often associated with southwesterly wind directions, when warmer air is transported over the colder sea, especially in summer. However, this pattern is site-dependent, as stability is strongly influenced by the temperature contrast with the nearest coastline. For other wind directions, particularly those bringing colder air over a relatively warmer sea, especially in winter, (very) unstable conditions tend to dominate (Nybø et al., 2020; Cheynet et al., 2018).

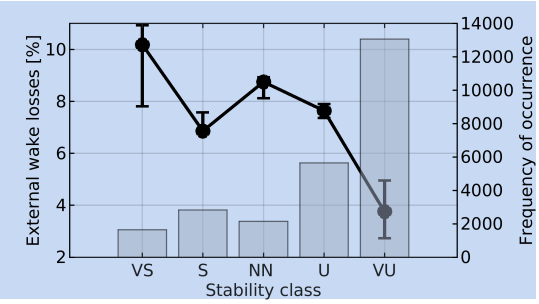


Figure 6. (Line) Spatiotemporal conditional average of external wake energy losses as a function of atmospheric stability classes (VS: Very Stable, S: Stable, NN: Near Neutral, U: Unstable, VU: Very Unstable) only including wind directions from 193° - 317°, (bars) frequency of occurrence for the different atmospheric stability classes. The error bars represent a 95% confidence interval obtained via bootstrapping with 1000 resamples.

External wake energy losses are expressed as percentages (Eq. 6). At lower wind speeds, turbines produce little power, so even small external wake energy losses appear as relatively large percentage losses (Fig. 4(d)), even though the absolute wake effect may not be stronger. At the same time, turbine thrust coefficients are higher at low wind speeds, leading to longer wake recovery distances. In contrast, when examining absolute losses (Fig. 7), the largest deficits occur for wind speeds between 10 and 15 ms^{-1} (mostly Region II). In this range, turbines operate close to rated power while still generating significant thrust, so wakes cause large power losses. At higher wind speeds, the thrust coefficients decrease and turbines typically remain at rated power even in the presence of wakes.

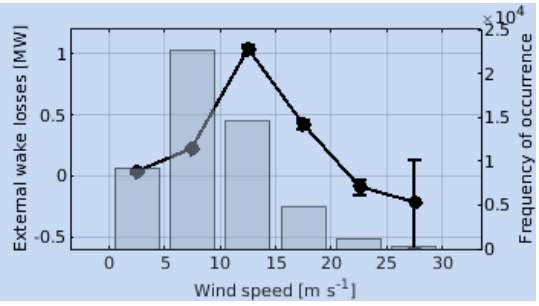


Figure 7. (Line) Spatiotemporal conditional average of absolute external wake energy losses as a function of wind speed, (bars) frequency of occurrence for the different wind speed bins. The error bars represent a 95% confidence interval obtained via bootstrapping with 1000 resamples.

Interestingly, negative external wake energy losses (-1%), i.e., positive interference from the construction of the new PE wind farm cluster, are observed for winds coming from the north to northeast (0°-60°) or south (1[illegible]10°) (Fig. 4 (b)). The negative external wake energy losses for wind directions from the south can be explained by a speedup at the lateral locations of the PE wind farm clusters (Fig. 8). It appears that the PE wind farm cluster act as a windbreak, causing global blockage and accelerating the flow around sides of the wind farm. A comparable lateral acceleration caused by global blockage is reported

for certain North Sea wind farm clusters (Borgers et al., 2025). While similar effects have been studied for windbreaks, where they mainly cause vertical speed-ups (Liu and Stevens, 2021), lateral flow accelerations influencing farm-to-farm wakes have only recently been examined in more detail (Hasager et al., 2015; Nygaard and Hansen, 2016; Borgers et al., 2025). Nygaard and Hansen (2016) observed this farm effect based on measured wind turbine data from two offshore wind farms. This speedup effect in the lateral direction has been observed multiple times for individual wind turbines (Ammara et al., 2022; Araya et al., 2014; Puccioni et al., 2023). In the coming years, it would be beneficial to enhance our understanding of this acceleration phenomenon around wind farms, through idealized simulations, however, this is outside the scope of this work. Understanding these speedups is important, as they may have a significant impact on external wake energy losses, necessitating consideration in the planning of high-density offshore regions.

Why negative external wake energy losses are observed for wind directions from the north to northeast is less clear. As mentioned previously for the AEP losses, these may result from numerical variability or other uncertainties in the simulation. The underlying mechanisms of these minor effects, which might be physical or not, should be investigated in the future.

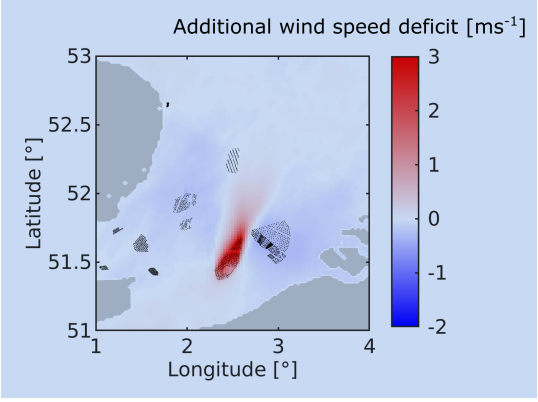


Figure 8. External BE-NL wind farm wake deficit for wind directions between 180° and 210°, the sector showing negative external wake losses. This map shows the additional wind speed deficit after the construction of the PE wind farm for timesteps with negative external wake energy losses over the farm.

3.4 Internal wake energy losses as a function of wind direction, wind speed and atmospheric stability

The yearly averaged internal wake energy losses are shown in Fig 9 (a). At specific locations within the BE-NL wind farm cluster (grid level), the internal wake energy losses reaches as high as 53%, which are similar values as in previous studies (Rosencrans et al., 2024; Rybchuk et al., 2022). These high internal wake energy losses are associated with very dense wind farm layouts. As mentioned previously, WRF with the Fitch wind farm parameterization, is knwon to overestimates the internal wake losses (Sanchez Gomez et al., 2024; Abkar and Porté-Agel, 2015), and the results here thus show the upper limit.

Figure 9(b) shows the spatiotemporal internal wake energy losses as a function of wind direction. The high internal wake energy losses are associated with wind directions corresponding to very dense wind farm layouts. Unlike the external wake energy losses (Fig. 4(b)), which are dominated by wind directions for which the wind farms are waked by the PE wind farm

cluster, the internal wake energy losses are strongest for the least frequent southeasterly wind direction (occurring only 4% of the time). This wind direction corresponds to conditions under which the largest number of turbines are influenced by upstream turbines within the same wind farm cluster.

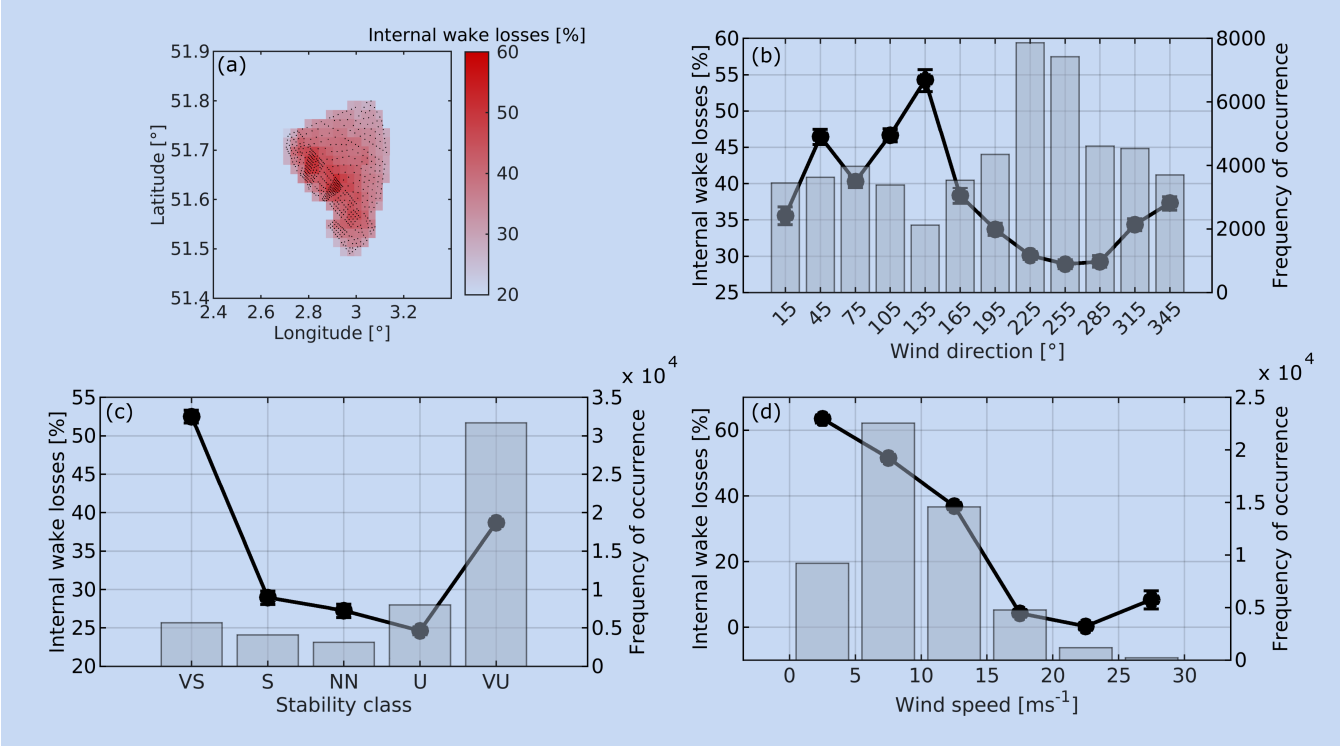


Figure 9. Results are shown for the BE-NL wind farm cluster. (a) Temporal average of internal wake energy losses for the BE-NL wind farm. (b) (Line) Spatiotemporal conditional average of internal wake energy losses as a function of wind direction, (bars) frequency of occurrence of the different wind directions. (c) (Line) Spatiotemporal conditional average of internal wake energy losses as a function of atmospheric stability classes (VS: Very Stable, S: Stable, NN: Near Neutral, U: Unstable, VU: Very Unstable), (bars) frequency of occurrence for the different atmospheric stability classes. (d) (Line) Spatiotemporal conditional average of internal wake energy losses as a function of wind speed, (bars) frequency of occurrence of the different wind speeds. The error bars represents a 95% confidence interval obtained via bootstrapping with 1000 resamples.

Figure 9 (c) shows the internal wake energy losses as a function of atmospheric stability. The internal wake energy losses generally decrease from stable to unstable conditions, with an apparent increase for very unstable conditions. Similar to the external wake energy losses, this may seem counterintuitive, but arises because this figure does not control for wind speed or wind direction and instead aggregates all atmospheric conditions. After additionally conditioning on wind speeds between 10 and 15 ms^{-1}, a clear pattern of decreasing internal wake energy losses with increasing atmospheric instability emerges (Fig. 10), as expected. Since very unstable conditions occur most frequently, a large number of low wind speed events are included, which increases the relative percentage losses and therefore results in higher apparent internal wake energy losses. This is

consistent with the findings of Xia et al. (2025), who showed that wind speed deficits do not translate linearly into power or energy losses.

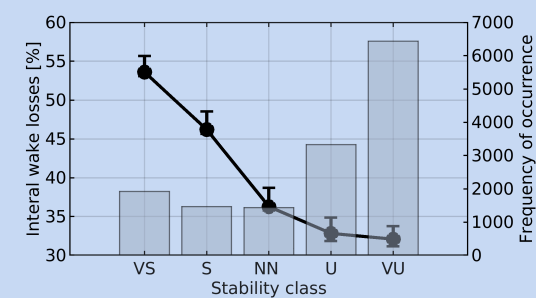


Figure 10. (Line) Spatiotemporal conditional average of internal wake energy losses as a function of atmospheric stability classes (VS: Very Stable, S: Stable, NN: Near Neutral, U: Unstable, VU: Very Unstable) only including wind speeds between 10 and 15 ms^{-1}, (bars) frequency of occurrence for the different atmospheric stability classes. The error bars represent a 95% confidence interval obtained via bootstrapping with 1000 resamples.

For the internal wake energy losses in function of velocity we observe the same behavior as for the external wake losses. When expressed as percentages, they are larger at lower wind speeds because the denominator is small, so even modest absolute deficits translate into large relative losses (Fig. 9 (d)). In contrast, when considering absolute losses, the largest deficits occur between 10 and 15 ms^{-1}, when turbines operate close to rated power with high thrust coefficients and wakes cause substantial power losses (Fig. 11). At higher wind speeds, turbines remain at rated power, which limits the relative impact of internal wake losses.

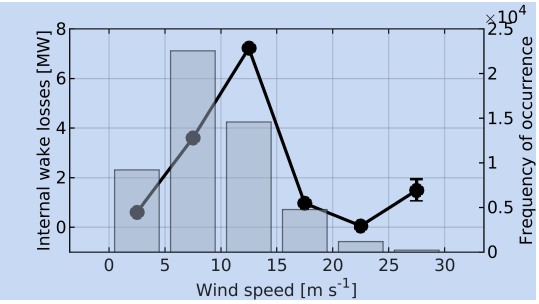


Figure 11. (Line) Spatiotemporal conditional average of absolute internal wake energy losses as a function of wind speed, (bars) frequency of occurrence for the different wind speed bins. The error bars represent a 95% confidence interval obtained via bootstrapping with 1000 resamples.

3.5 Internal wake evolution across successive turbine-containing grid cells

We seek to further understand the complex interactions between the internal and external wake effects. To do so, we look at the internal wake energy losses of five subsequent wind turbines containing grid cells for two specific wind directions, one in

which the BE-NL wind farm cluster is not affected by the new PE wind farm cluster and one in which it is. In Fig. 12, we demonstrate that the structure of the internal wake of the selected wind turbines are affected by the new upstream PE wind farm cluster. If the turbines are not in the wake of the upstream PE wind farm cluster the internal wake is unaffected by the presence of the new PE wind farm cluster (Fig. 12 (a)-(e)). However, the internal wakes of the selected wind turbines of the downwind farm that are in the wake of the new PE wind farm cluster undergo non linear effects (Fig. 12 (f)-(j)). The power normalized by the first row turbines is higher for the turbines when they are waked by the PE wind farm cluster (Fig. 12 (h)). This increase in power could be caused by a higher added TKE compared to the simulation without the new PE wind farm cluster (Fig. 12 (j)) which enhances the mixing of the wake and thus dissipates the wake faster. Additionally, the velocity deficit is smaller for the waked turbines which additionally results in higher power after the front row wind turbine (Fig. 12 (i)). Together, the new PE wind farm cluster lowers the overall power of the turbines (Fig. 12 (g)) but it also reduces the internal wake energy losses (Fig. 12 (h)). This phenomena again emphasized the caution that should be paid in the future for farm-farm interactions, as they can induce non-linear effects within a distant wind farm.

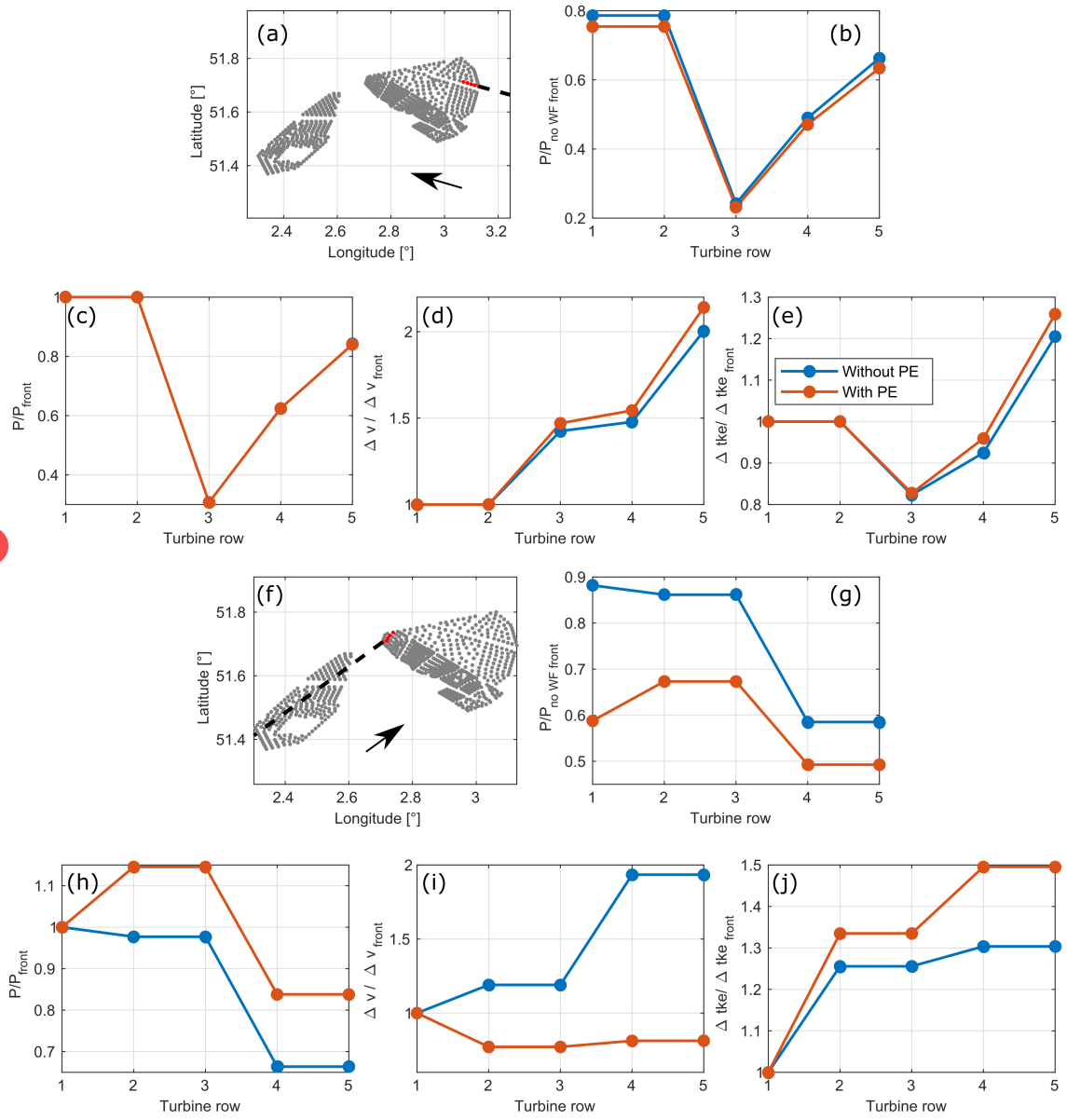


Figure 12. (a) & (f) In red are the wind turbine locations considered for a specific wind direction (depicted by the black arrow (a) 105° (f) 234°), for (a) the BE-NL wind farm cluster is not waked by the PE wind farm cluster while for (f) the BE-NL cluster is waked by the PE wind farm cluster. (b) & (g) The wind turbine power per turbine row normalized by the no WF front row turbine for unwaked (blue) and waked (orange) conditions. (c) & (h) The wind turbine power per turbine row normalized by the front row turbine for unwaked (blue) and waked (orange) conditions. (d) & (i) The wind speed deficit (compared to the noWT case) per turbine row normalized by the front row turbine for unwaked (blue) and waked (orange) conditions. (e) & (f) The added TKE (compared to the no WT case) per turbine row normalized by the front row turbine for unwaked (blue) and waked (orange) conditions.

3.6 Hourly and monthly variation in external and internal wake energy losses

Due to the temporal variability in atmospheric conditions, the yearly averaged wake energy losses are not informative on which atmospheric conditions are more critical to induce larger internal or external wake energy losses. As mentioned earlier the atmospheric conditions (wind direction, atmospheric stability class and wind speed) are based on a reference location (spatial averaged grid cell location of the considered BE-NL wind farm cluster) of the no WF WRF simulation at a height of 96 m. There is a different behaviour, in both hourly and monthly timescales, between the external and internal wake energy losses (Fig. 13 (b) & (d)). The hourly variation is stronger for external wake energy losses compared to internal wake energy losses, and both vary seasonally. Larger external wake energy losses are observed in summer during the late afternoon, while the internal wake energy losses variability are mainly determined by the season. The higher external wake energy losses in summer are explained by the lower wind speeds that coincide with the steep ramp of the power curve and have higher turbine thrust coefficients (Fig. 13 (e)) and the higher occurrence of stable atmospheric conditions (Fig. 13 (g)), when warm air is advected over the colder water (Rosencrans et al., 2024). Additionally, these higher external wake losses coincide with increased fraction of time during which the wind farm is waked by the upstream PE wind farm cluster (Fig. 13 (h)). In contrast, lower wake energy losses in winter occur for higher wind speed and more unstable atmospheric conditions (Fig. 13 (e) & (g)), when cold air moves across the warmer water (Rosencrans et al., 2024). It should be noted that these results are based on one year of data, and therefore any generalisation of the diurnal and seasonal variation should be made with caution. In addition, further investigation to better understand the occurrence of negative external wake losses during the evening hours in spring is required in the future but outside the scope of this manuscript.

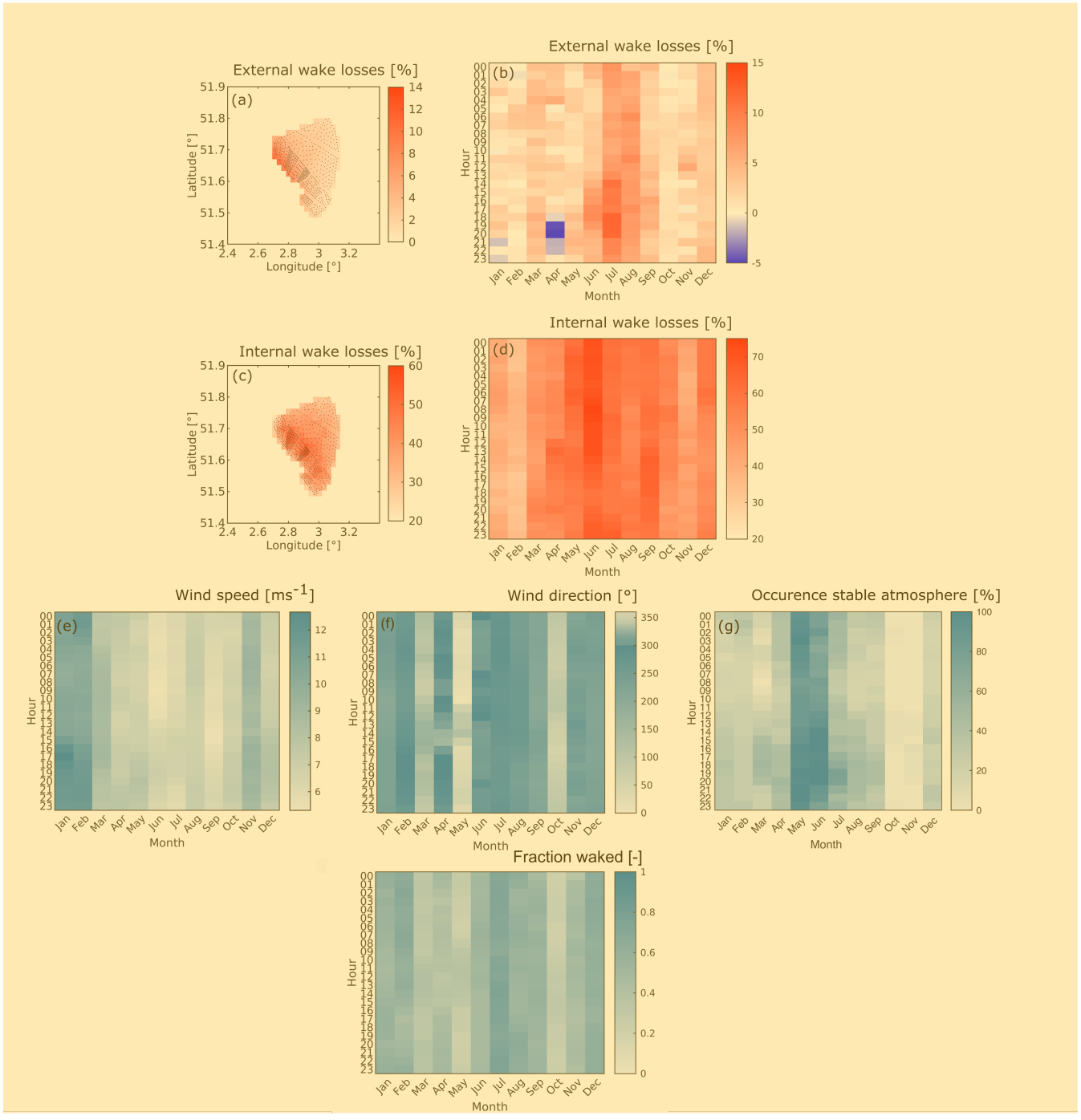


Figure 13. Results are shown for the BE-NL wind farm cluster. (a) Temporal average external wake energy losses. (b) Hourly and monthly variations of the spatiotemporally averaged external wake energy losses. (c) Yearly averaged internal wake energy losses. (d) Hourly and monthly variations of the spatiotemporally averaged internal wake energy losses. Hourly and monthly variations of (e) wind speed, (f) wind direction, (g) occurrence of stable atmospheric conditions (h) fraction of wind directions within the PE wind farm cluster wake (193° - 317°), with 1 corresponding to waked and 0 to non waked conditions.

The yearly averaged and the sub-annual variation of the wake energy losses of a new wind farm cluster on adjacent, existing wind farms is studied, this for the new Princess Elisabeth cluster. The wake impacts of a representative year has been simulated with the mesoscale model WRF to estimate representative wake energy losses.

The mesoscale model predicts that building the new Princess Elisabeth wind farm cluster gives differences up to 5% of AEP for a closely located neighbouring wind farm. The external wake energy losses of this closely located neighbouring wind farm are mainly determined by the waked wind direction of the Princess Elisabeth wind farm cluster, stable conditions and region II wind speeds. The internal wake energy has the largest losses for wind directions with the highest wind turbine densities within the wind farm. Additionally, the interaction with the new wind farm cluster induces a non-linear modification of the internal wake dynamics, whereby increased turbulence promotes wake recovery and partially offsets internal wake losses within the downwind farm. Interestingly, some further located wind farms show negative wake losses. For closely located farms, such negative values can in part be explained by specific wind directions where a lateral speedup occurs at the flanks of the upstream wind farm. However, for more distant farms, negative wake losses but also very small positive values, could be due to numerical variability or other simulation uncertainties. A more in depth study of these values and their significance are needed in future work.

These internal and external wake energy losses are investigated by hour and month. The external wake energy losses exhibit a stronger hourly variation, while the internal wake energy losses depend strongly on season. However, both variations can be linked to the atmospheric stability and wind speed. With stable atmospheric conditions and wind speeds below rated power resulting in higher wake energy losses.

This study provides a year-long dataset simulated by WRF, which provides insight into the order of magnitude of external and internal wake effects that may be expected in future North Sea wind power development. We also elucidate how these wake effects depend on season and hours of the day, wind speed, wind direction, and atmospheric stability. These data could also serve as calibration data for future improvements in fast-running models. While the WRF model is not ground-truth, engineering wake models could be compared for farm–farm interactions based on these results, which is presented in the companion paper "Annual wake impacts in en between wind farm clusters - Part II: comparison of WRF and fast-running engineering wake models". However, the development of enhanced wake models falls outside the scope of this work. Future work could include a validation of farm-farm interactions once the new Princess Elisabeth wind farm cluster is built, which would provide clearer reference values and could accelerate model developments in WRF.

Code and data availability. The Advanced Research WRF (ARW) model is developed by the National Center for Atmospheric Research (Skamarock et al., 2008). WRF v4.3 is publicly available athttps://github.com/wrf-model/WRF/releases/tag/v4.3. The forcing data used for WRFs initial and boundary conditions in the WRF simulations is also publicly available at https://cds.climate.copernicus.eu/cdsapp!/dataset/reanalysis-era5-single-levels?tab=form and https://cds.climate.copernicus.eu/cdsapp!/dataset/reanalysis-era5-pressure-levels?tab=form. Data from the numerical simulations and the namelists used in the WRF model are available upon reasonable requests excluding any potentially confiden-

tial information. The measurements at Lichteiland Goeree can be retrieved at the data platform of the Royal Netherlands Meteorological Insitute (KNMI) (Koninklijk Nederlands Meteorologisch Instituut, 2022). For the in situ measurements at the Belgian coast, the data can be obtained from the website of the Belgian coastal measurement network (Meetnet Vlaamse Banken, 2022).

Appendix A: Wind turbine details

Table A1. Wind Farm details, including the name of the wind farm, the number of turbines per wind farm, the turbine capacity, the turbine hub height and turbine rotor diameter.

Wind farm name	Total number of turbines (#)	Turbine Capacity	Hub Height (m)	Rotor Diameter (m)
Belwind	55	3.0 MW	70.1	112
Belwind Alstom Hailiade	1	6.0 MW	98.1	150
Borssele I Borssele II	94	8.4 MW	107	164
Borssele III Borssele IV	77	9.5 MW	107	164
Borssele V	2	9.5 MW	107	164
C-POWER I	6	5.0 MW	93.3	126
C-POWER II & III	48	6.15 MW	93.3	126
East Anglia ONE	102	7 MW	120	154
Egmond aan Zee	36	3 MW	70	90
Galloper	56	6 MW	88	154
Greater Gabbard	140	3.6 MW	78	107
Gunfleet Sands	50			
	48	3.6 MW	78	107
	2	6 MW	84	120
Kentish Flats	45			
	30	3 MW	70	90
	15	3.3 MW	83.6	112
London Array	175	3.6 MW	87	120
Luchterduinen	43	3 MW	81	112
Nobelwind	50	3.3 MW	77.1	112
Norther	44	8.4 MW	107	164
Northwind	72	3.0 MW	80.1	112
Northwester 2	23	9.5 MW	107	164
Prinses Amalia	60	2 MW	60	80
Rentel	42	7.35 MW	102	154
Scroby Sands	30	2.0 MW	68	80
SeaMade (Seastar)	30	8.4 MW	107	164
Seamade (Mermaid)	28	8.4 MW	107	164
Thanet	100	3 MW	70	90

Appendix B: Representative year

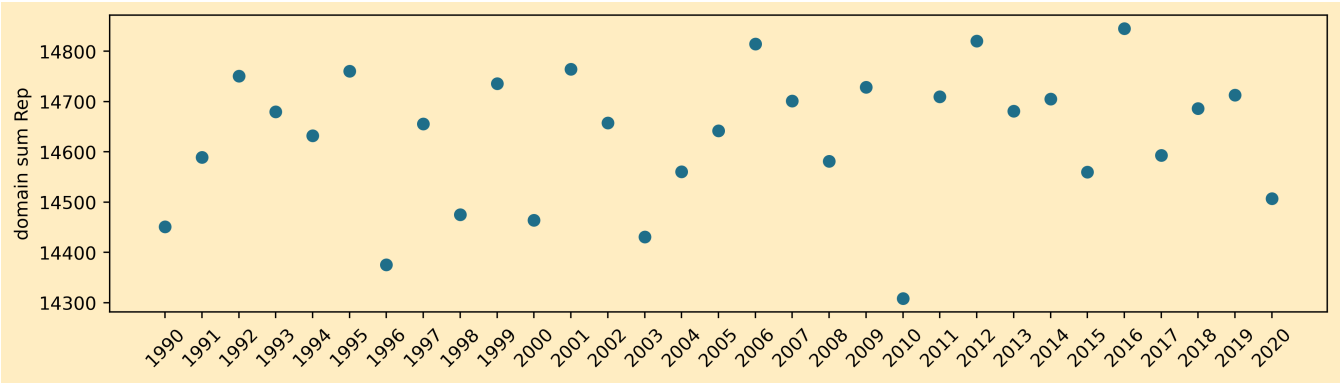


Figure B1. Sum of the representativeness per year over the area of interest, where the representativeness is based on the Perkins Skill Score for the wind climate between each single year and the 30 year window (Borgers et al., 2024).

Appendix C: Confidence interval for mean bias (simulation - observation)

The uncertainty calculation accounts for both the variability of the bias time series and the uncertainty associated with the measurements . For wind speed, a relative measurement uncertainty (U_m) of 3.3% is assumed for all stations, except Westhinder where a value of 5.6% is used. For wind direction, no measurement uncertainty is available and thus only the model variability is considered.

The effective number of independent samples (N_{eff}) is estimated to account for temporal autocorrelation (10 minute output) in the bias time series as shown in Eq. C1.

$$N_{\text{eff}} = \frac{N}{1 + 2\rho_1} \tag{C1}$$

Here, N is the total number of samples and ρ_1 is the lag-1 autocorrelation coefficient of the bias.

The total uncertainty on the mean bias (U_{tot}) is calculated as the quadratic sum of the uncertainty due to model variability and the uncertainty associated with the measurements, shown in Eq. C2.

$$U_{\text{tot}} = \sqrt{\left(\frac{\sigma_{\text{bias}}}{\sqrt{N_{\text{eff}}}}\right)^2 + \left(\frac{U_m \bar{X}_{\text{obs}}}{\sqrt{N_{\text{eff}}}}\right)^2} \tag{C2}$$

Here, σ_{bias} is the standard deviation of the bias time series, and $\bar{X}_{\text{obs}}$ is the mean measured value at the observation mast. The first term in Eq. C2 represents the standard error of the mean bias due to model variability, while the second term represents the measurement uncertainty. When the measurement uncertainty is not available (e.g., for wind direction), only the first term in Equation C2 is used.

Author contributions. SP contributed to the conceptualization, formal analysis, data curation, software, validation, methodology, visualisation, and writing (original draft, review and editing). MFH contributed to conceptualization, methodology, visualisation, funding, supervision and writing (review and editing). ML helped in wrinting (review and editing). RB contributed to data curation, methodology, and writing (review and editing). SB contributed to the conceptualization, funding, and writing (review and editing). WM contributed to the conceptualization, formal analysis, validation, methodology, visualisation, funding, and writing (review and editing).

Competing interests. The authors declare that no competing interests are present.

Acknowledgements. SP and MFH were funded by MIT Climate Grand Challenges. WM acknowledges support from the Energy Transition Fund of the Federal Public Service Economy of the Belgian Federal Government through the BeFORECAST project, as well as from the Flemish Agency for Innovation and Entrepreneurship (VLAIO) through the Cloud4Wake project. The resources and services used in this work were provided by the VSC (Flemish Supercomputer Center), funded by the Research Foundation-Flanders (FWO) and the Flemish Government.

References

Abkar, M. and Porté-Agel, F.: A new wind-farm parameterization for large-scale atmospheric models, Journal of Renewable and Sustainable Energy, 7, 013 121, 2015.

Akhtar, N., Geyer, B., and Rockel, P., S. C.: Accelerating deployment of offshore wind energy alter wind climate and reduce future power generation potentials, Scientific Reports, 11, 2021.

Ammara, I., Leclerc, C., and Masson, C.: A Viscous Three-Dimensional Differential/Actuator-Disk Method for the Aerodynamic Analysis of Wind Farms., Journal of Solar Energy Engineerin, 124, 2022.

Araya, D., Craig, A., Kinzel, M., and Dabiri, J.: Low-order modeling of wind farm aerodynamics using leaky Rankine bodies, Journal of Renewable and Sustainable Energy, 6, 2014.

Archer, C., Wu, S., Ma, Y., and Jiménez, P.: Two Corrections for Turbulent Kinetic Energy Generated by Wind Farms in the WRF Model, Monthly Weather Review, 148, 4823–4835, 2020.

Barthelmie, R. J., Pryor, S. C., Frandsen, S. T., Hansen, K. S., Schepers, J. G., Rados, K., Schlez, W., Neubert, A., Jense, n. L. E., and Neckelmann, S.: Quantifying the Impact of Wind Turbine Wakes on Power Output at Offshore Wind Farms, Journal of Atmospheric and Oceanic Technology, 27, 1302 – 1317, 2010.

Borgers, R., M., D., Wijnant, I., Stepek, A., Stoffelen, A., Akhtar, N., Neirynck, J., Van de Wallen, J., Meyers, J., and van Lipzig, N.: Mesoscale modelling of North Sea wind resources with COSMO-CLM: model evaluation and impact assessment of future wind farm characteristics on cluster-scale wake losses, Wind Energy Science, 9, 697–719, 2024.

Borgers, R., Meyers, J., and van Lipzig, N.: Energy production and inter-farm wake losses in future North Sea wind farms, Environmental Research Letters, 20, 2025.

Cheynet, E., Jakobsen, J., and Reuder, J.: Velocity Spectra and Coherence Estimates in the Marine Atmospheric Boundary Layer, Boundary-Layer Meteorology, 169, 429–460, 2018.

Cornillie, J., Baetens, R., and Vanheusden, W.: LCOE Offshore Wind in the Princess Elisabeth zone, Tech. rep., 3E, 2021.

Cuevas-Figueroa, G., Stansby, P., and Stallard, T.: Accuracy of WRF for prediction of operational wind farm data and assessment of influence of upwind farms on power production, Energy, 254, 2022.

EMD International A/S: WindPro, https://www.emd-international.com/windpro/, accessed: April 30, 2024.

Fischereit, J., Larsen, X., and Hahmann, A.: Climatic Impacts of Wind-Wave-Wake Interactions in Offshore Wind Farms, Frontiers in Energy Research, 13, 2020.

Fischereit, J., Brown, R., Larsén, X., Badger, J., and Hawkes, G.: Review of mesoscale wind-farm parameterizations and their applications, Boundary-Layer Meteorology, 182, 175–224, 2022a.

Fischereit, J., Schaldemose Hansen, K., Larsen, X., van der Laan, M., Rethore, P.-E., and Murcia Leon, J.: Comparing and validating intra-farm and farm-to-farm wakes across different mesoscale and high-resolution wake models, Wind Energy Science, 7, 1069–1091, https://doi.org/10.5194/wes-7-1069-2022, 2022b.

Fitch, A., Lundquist, J., Dudhia, J., Gupta, A.K.and Michalakes, J., and Barstad, I.: Local and mesoscale impacts of wind farms as parameterized in a mesoscale NWP Model, Monthly Weather Review, 140, 3017–3038, 2012.

Hahmann, A., Vincent, C., Pena, A., Lange, J., and Hasager, C.: Wind climate estimation using WRF model output: methodand model sensitivities over the sea, International Journal for Climatology, 35, 3422–3439, 2014.

Hasager, C., Vincent, P., Badger, J., Badger, M., Di Bella, A., Peña, A., Husson, R., and Volker, P.: Using Satellite SAR to Characterize the Wind Flow around Offshore Wind Farms, Energies, 8, 5413–5439, 2015.

Hersbach, H., Bell, B., Berrisford, P., Biavati, G., Horányi, A., Munoz Sabater, J., Nicolas, J., Peubey, C., Radu, R., Rozum, I., Schepers, D., S. A., Soci, C., Dee, D., and Thépaut, J.-N.: ERA5 hourly data on single levels from 1959 to present. Copernicus Climate Change Service (C3S), Climate Data Store (CDS), 2018a.

Hersbach, H., Bell, B., Berrisford, P., Biavati, G., Horányi, A., Munoz Sabater, J., Nicolas, J., Peubey, C., Radu, R., Rozum, I., Schepers, D., S. A., Soci, C., Dee, D., and Thépaut, J.-N.: . ERA5 hourly data on pressure levels from 1959 to present. Copernicus Climate Change Service (C3S), Climate Data Store (CDS), 2018b.

Hoeser, T., Feuerstein, S., and Kuenzer, C.: DeepOWT: A global offshore wind turbine data set from Sentinel-1 data, Earth System Science Data, 14, 4251–4270, 2022.

Howland, M. F., Ghate, A. S., Quesada, J. B., Pena Martínez, J. J., Zhong, W., Larrañaga, F. P., Lele, S. K., and Dabiri, J. O.: Optimal closed-loop wake steering – Part 2: Diurnal cycle atmospheric boundary layer conditions, Wind Energy Science, 7, 345–365, 2022.

Iacano, M., Delamere, J., Mlawer, E., Shephard, M., Clough, S., and Collins, W.: Radiative forcing by long lived greenhouse gases: calculations with the AER radiative transfer models, Journal of geophysical research: atmospheres, 113, 2008.

Ivanova, T., Porchetta, S., Buckingham, S., van Beeck, J., and Munters, W.: Improving Wind and Power Predictions via Data Assimilation (FDDA) in the WRF Model: Case Study of Storms in February 2022 at Belgian Offshore Wind Farms, Wind Energy Science Discussions, 2023.

Jiménez, P., Dudhia, J., González-Rouco, F., Navarro, J., Montávez, J., and García-Bustamente, E.: A revised scheme for the WRF Surface Layer Formulation, Monthly Weather Review, 140, 898–918, 2012.

Kain, J.: The Kain-Fritsch convective parameterization: an update, Journal of Applied Meteorology and Climatology, 43, 170–181, 2004.

Klemmer, K., Condon, E., and Howland, M.: Evaluation of wind resource uncertainty on energy production estimates for offshore wind farms, Journal of Renewable and Sustainable Energy, 16, 2024.

Koninklijk Nederlands Meteorologisch Instituut: KNMI data platform, https://dataplatform.knmi.nl/group/wind, 2022.

Lee, J. and Lundquist, J.: Evaluation of the wind farm parameterization in the Weather Research and Forecasting model (version 3.8.1) with meteorological and turbine power data, Geoscientific Model Development, 10, 4229–4244, 2017.

Li, H., Claremar, B., Wu, L., Hallgren, C., Körnich, H., Ivanell, S., and Sahlée, E. .: A sensitivity study of the WRF model in offwhore wind modeling over the Baltic Sea, Geoscience Frontiers, 12, 2021.

Liu, L. and Stevens, R.: Enhanced wind-farm performance using windbreaks, Physical Revies Fluids, 6, 2021.

Lundquist, J., DuVivier, K., Kaffine, D., and Tomaszewski, J.: Costs and consequences of wind turbine wake effects arising from uncoordinated wind energy development, Nature Energy, 4, 26–34, https://doi.org/10.1038/s41560-018-0281-2, 2019.

Meetnet Vlaamse Banken: Data of the Flemish Banks Monitoring Network, https://meetnetvlaamsebanken.be/Download/Welcome, 2022.

Monin, A. and Obukhov, A.: Basic laws of turbulent mixing in the surface layer of the atmosphere, Tr. Akad. Nauk SSSR Geophiz. Inst., 24, 1954.

Morrison, H., Curry, J., and Khvorostyanov, V.: A new double-moment microphysics parameterization for application in cloud and climate models. Part I: description, Journal of the Atmospheric Sciences, 62, 1665–1667, 2005.

Munoz-Esparza, D., Canadillas, B., Neumann, T., and van Beeck, J.: Turbulent fluxes, stability and shear in the offshore environment: Mesoscale modelling and field observations at FINO1, journal of Renezable and Sustainable Energy, 4, 2012.

Munters, W., Adiloglu, B., Buckingham, S., and van Beeck, J.: Wake impact of constructing a new offshore wind farm zone on an existing downwind cluster: a case study of the Belgian Princess Elisabeth zone using FLORIS, in: Journal of Physics: Conference Series, vol. 2265, 2022.

Nakanishi, M. and Niino, H.: An improved Mellor-Yamada level 3 model: its numerical stability and application to a regional prediction of advection fog, Boundary-Layer Meteorology, 119, 397–407, 2006.

Nybø, A., Nielsen, F., Reuder, J., Churchfield, M. J., and Godvik, M.: Evaluation of different wind fields for the investigation of the dynamic response of off shore wind turbines, Wind Energy, 23, 1777–1886, 2020.

Nygaard, N. and Hansen, S.: Wake effects between two neighbouring wind farms, in: Journal of Physics: Conference Series, vol. 753, 2016.

Palatos-Plexidas, A., Gremmo, S., van Beeck, J., De Cruz, L., and Munters, W.: Assessing the Accuracy of a Three-Year High-Resolution Mesoscale Wind Farm Wake Simulation with Lidar and Satellite Radar Data, Wind Energy Science Discussions, 2025, 1–33, https://doi.org/10.5194/wes-2025-202, 2025.

Pan, Y. and Archer, C.: A Hybrid Wind-Farm Parameterization for Mesoscale and Climate Models, Boundary-Layer-Meteorology, 168, 469–495, 2018.

Pierrot, M.: The Wind Power, https://www.thewindpower.net, 2024.

Platis, A., Siedersleben, S., Bange, J., Lampert, A., Barfuss, K., Hankers, R., Canadillas, B., Foreman, R., Schulz-Stellenfleth, J., Djath, B., Neumann, T., and Emeis, S.: First in situ evidence of wakes in the far field behind offshore wind farms, Scientific Reports, 8, https://doi.org/10.1038/s41598-018-20389-y, 2018.

Platis, A., Hundhausen, M., Lampert, A., Emeis, S., and Bange, J.: The Role of Atmospheric Stability and Turbulence in Offshore Wind-Farm Wakes in the German Bight, Boundary-Layer Meteorology, pp. 441–469, 2022.

Porchetta, S., Temel, O., Muñoz Esparza, D., Reuder, J., Monbaliu, J., van Beeck, J., and van Lipzig, N.: A new roughness length parameterization accounting for wind-wave (mis) alignment, Atmospheric Chemistry and Physics, pp. 6681–6700, 2019.

Porchetta, S., Temel, O., Warner, J., Muñoz Esparza, D., Monbaliu, J., van Beeck, J., and van Lipzig, N.: Evaluation of a roughness length parameterization accounting for wind-wave alignment in a coupled atmosphere-wave model, Quarterly Journal of the Royal Meteorological Society, 147, 825–846, 2020.

Porchetta, S., Munoz-Esparza, D., Munters, W., and van Beeck, J.: Impact of ocean waves on offshore wind farm power production, Renewable energy, 180, 1179–1193, 2021.

Prosper, M., Otero-Casal, C., Canoura Fernandez, F., and Miguez-Macho, G.: Wind power forecasting for a real onshore wind farm on complex terrain using WRF high resolution simulations, Renewable Energy, 135, 674–686, 2019.

Pryor, S., Shepherd, T., Volker, P., Hahmann, A., and Barthelmie, R.: "Wind Theft" from onshore wind turbine arrays: sensitivity to wind farm parameterization and resolution, Journal of Applied Meteorology and Climatology, 59, 145–174, 2020.

Pryor, S., Barthelmie, R., and Shepherd, T.: Wind power production from very large offshore wind farms, Joule, 5, 2663–2686, 2021.

Puccioni, M., Moss, C.F. end Jacquet, C., and Iungo, G.: Blockage and speedup in the proximity of an onshore wind farm: A scanning wind LiDAR experiment, Journal of Renewable and Sustainable Energy, 15, 2023.

Redfern, S., Olson, J., Lundquist, J., and Clack, C.: Incorporation of the Rotor-Equivalent Wind Speed into the Weather Research and Forecasting Model's Wind Farm Parameterization, Monthly Weather Review, 137, 1029–1046, 2019.

Rosencrans, D., Lundquist, J., Optis, M., Rybchuk, A., Bodini, N., and Rossol, M.: Seasonal variability of wake impacts on US mid-Atlantic offshore wind plant power production, Wind Energy Science Discussions, 9, 555–583, 2024.

Rybchuk, A., Juliano, T., Lundquist, J., Rosencrans, D., Bodini, N., and Optis, M.: The sensitivity of the fitch wind farm parameterization to a three-dimensional planetary boundary layer scheme, Wind Energy Science, 7, 2085–2098, 2022.

Sanchez Gomez, M., Deskos, G., Lundquist, J., and Juliano, T.: Can mesoscale models capture the effect from cluster wakes offshore?, in: Journal of Physics: Conference Series, vol. 2767, 2024.

Schneemann, J., Rott, A., Dörenkämper, M., Steinfeld, G., and Kühn, M.: Cluster wakes impact on a far-distant offshore wind farm's power, Wind Energy Science, 5, 29–49, https://doi.org/10.5194/wes-5-29-2020, 2020.

Siedersleben, S., Platis, A., Lundquist, J., Djath, B., Lampert, A., Bärfuss, K., Canadillas, B., Schulz-Stellenfleth, J., Bange, J., Neumann, T., and Emeis, S.: Turbulent kinetic energy over large offshore wind farms observed and simulated by the mesoscale model WRF (3.8.1), Geoscientific Model Development, 13, 249–269, 2020.

Skamarock, W. C., Klemp, J. B., Dudhia, J., Gill, D. O., Barker, D., Duda, M. G., and Powers, J. G.: A Description of the Advanced Research WRF Version 3, Tech. Rep. NCAR/TN-475+STR, National Center for Atmospheric Research, Boulder (CO), USA, 2008.

Stieren, A. and Stevens, R.: Impact of wind farm wakes on flow structures in and wround downstream wind farms, Flow, 2, 2022.

Sward, J., Ault, T., and Zhang, K.: Spatial biases revealed by LiDAR in a multiphysics WRF ensemble designed for offshore wind, Energy, 262, 2023.

Tewari, M., Chen, F., Wang, W., Dudhia, J., LeMone, M., Mitchell, K., Ek, M., Gayno, G., Wegeil, J., and Cuenca, R.: Implementation and verification of the unified Noah land surface model in the WRF model., pp. 11–15, 20th Conference on Weather Analysis and Forecasting/16th Conference on Numerical Weather Prediction, 2004.

Tomaszewski, J. and Lundquist, J.: Simulated wind farm wake sensitivity to configuration choices in the Weather Research and Forecasting model version 3.8.1, Geoscientific Model Development, 10, 2645–2662, 2022.

Van Wijk, A., Beljaars, A., Holtslag, A., and Turkenburg, W.: Evaluation of stability corrections in wind speed profiles over the North Sea, Journal of Wind Engineering and Industrial Aerodynamics, 33, 551–566, 1990.

Veers, P., Dykes, K., Lantz, E., Barth, S., Bottasso, C., Carlson, O., Clifton, A., Green, J., Green, P., Holttinen, H., Laird, D., Lehtomäki, V., Lundquist, J., Manwell, J., Marquis, M., Meneveau, C., Moriarty, P., Munduate, X., Muskulus, M., Naughton, J., Pao, L., Paquette, J., Peinke, J., Robertson, A., Rodrigo, J. S., Sempreviva, A., Smith, J. C., Tuohy, A., and Wiser, R.: Grand challenges in the science of wind energy, Science, 366, https://doi.org/10.1126/science.aau2027, 2019.

Vermuri, A., Buckingham, S., Munters, W., Helsen, J., and van Beeck, J.: Sensitivity analysis of mesoscale simulations to physics parameterizations over the Belgian North Sea using Weather Research and Forecasting – Advanced Research WRF (WRF-ARW), Wind Energy Science, 7, 1869–1888, 2022.

Wu, S., Archer, C., and Mirocha, J.: New insights on wind turbine wakes from large-eddy simulation: Wake contraction, dual nature, and temperature effects, Wind Energy, 2023.

Xia, G., Optis, M., Deskos, G., Sinner, M., Mulas Hernando, D., Lundquist, J. K., Kumler, A., Sanchez Gomez, M., Fleming, P., and Musial, W.: Understanding Cluster Wake-Induced Energy Losses off the U.S. East Coast, Wind Energy Science Discussions, 2025, 1–35, https://doi.org/10.5194/wes-2025-154, 2025.

Annual wake impacts in and between wind farm clusters - Part II: Comparison of WRF and fast-running engineering wake models

Sara Porchetta[1,2,3], Michael F. Howland[1], Maxime Lejeune[3], Ruben Borgers[4], Sophia Buckingham[5], and Wim Munters[3]

[1]Massachusetts Institute of Technology, Civil and Environmental Engineering, 77 Massachusetts Avenue, 1-290, Cambridge, MA 02139, United States of America
[2]Faculty of Civil Engineering and Geosciences, Delft University of Technology, Delft, The Netherlands
[3]von Karman Institute for Fluid Dynamics, 1640 Sint-Genesius-Rode, Belgium
[4]Department of Earth and Environmental Sciences, KU Leuven, Belgium
[5]ENGIE Laborelec, 1630 Linkebeek, Belgium

Correspondence: s.p.porchetta@tudelft.nl

Abstract.

Wind energy is essential for global decarbonization strategies, and the rapid expansion of offshore wind farms has led to increasingly large and closely spaced wind farm clusters. As a result, assessments of wake impacts increasingly rely on numerical models, multiple models exist which differ in physical assumptions, representations of atmospheric processes and computational cost. Numerical weather prediction models and fast-running engineering wake models are both used for long-term wake impact studies, yet they are based on different assumptions regarding atmospheric variability and wake recovery. These differences introduce uncertainty in predicted power production and it remains unclear how consistently the different modeling approaches estimate long-term wake impacts and how sensitive these estimates are to model formulation.

Here we compare wake impacts predicted by commonly used engineering wake models with those simulated by a numerical weather prediction model (WRF), simulated in Part I of this paper series, for a meteorologically representative year (2016), focusing on the planned Princess Elisabeth offshore wind farm cluster and the Belgian-Dutch wind farm cluster in the southern North Sea. We show that engineering wake models generally predict higher wind farm power production and smaller wake energy losses than WRF. Separating wake energy losses into internal and external components reveals that external wake energy losses have a larger relative spread between modeling approaches than internal wake energy losses, particularly during summer.

By analyzing wake energy losses as a function of atmospheric stability, we demonstrate that discrepancies between modeling approaches increase under stable stratification, which occurs more frequently during summer. Under these conditions, reduced turbulent mixing leads to slower wake recovery and increased sensitivity to the wake recovery formulation. Engineering wake models that explicitly account for turbulence-dependent wake recovery, show closer agreement with WRF, particularly for external wake losses. These results quantify the uncertainty associated with long-term intra-farm and farm–farm wake estimates and identify atmospheric stability as a key driver of model spread.

This paper forms the second part of a two-part study investigating wake impacts of offshore wind farms. In Part I, wake effects induced by the planned Princess Elisabeth wind farm cluster are analysed using WRF to characterize annual mean and sub-annual variability under atmospheric conditions. The present paper (Part II) builds on this analysis by comparing the WRF estimates with commonly used fast-running engineering wake models, enabling a systematic assessment of differences between modeling approaches and the uncertainty associated with long-term intra and farm–farm wake estimates.

1 Introduction

Wind energy is essential for our global decarbonization strategy. In recent years, an accelerating deployment of wind energy has been seen, urging for a better understanding of its interaction with its surroundings. Furthermore, because of this rapid expansion of wind energy, wind farms are larger in size and closer to each other. In densely developed regions, such as the North Sea, the interaction between neighboring wind farms becomes more important, known as the farm-farm wake interaction. A farm wake is the region of reduced wind speed behind a wind farm that affects the power production of a wind farm located downstream (Lundquist et al., 2019; Barthelmie et al., 2010; Pryor et al., 2021; Stieren and Stevens, 2022). These farm–farm wake interactions introduce an additional source of uncertainty in wind resource assessment and energy yield estimates, which has direct impacts on wind farm development. Moreover, wake impacts are not constant in time and vary during the year, which is particularly important for operational planning, maintenance scheduling, and short-term power trading.

Different numerical models examine these farm-farm wakes, each model focuses on different atmospheric scales, ranging from the microscale to the mesoscale, synoptic scales, and even global scales (Veers et al., 2019; Porté-Agel et al., 2020). Microscale numerical approaches for studying farm-farm wakes encompass a range of fidelity levels. High-fidelity computational fluid dynamics models such as large eddy simulations (Maas and Siegfried, 2022; Stieren and Stevens, 2022) and mid-fidelity Reynolds-Averaged Navier-Stokes models (van der Laan et al., 2015, 2023) are computationally more expensive, often still limiting their application to specific atmospheric conditions. On the other hand, low-fidelity, fast-running engineering wake models provide a cost-effective alternative for wake studies that can account for multiple atmospheric conditions (Nygaard et al., 2020; Nygaard and Hansen, 2016; Munters et al., 2022). Yet, they highly simplify the underlying physics and often rely on empirical tuning, limiting their ability to fully capture the actual atmospheric conditions.

In recent years, numerical weather prediction models have been employed to study wakes (Cuevas-Figueroa et al., 2022). These models account for multiple non-uniform spatial and temporal atmospheric variables and are able to capture flow heterogeneity at the mesoscale. For wind energy purposes, these models have typically spatial horizontal resolutions between 1 and 3 km, which is larger than the typical inter-turbine spacings (Fischereit et al., 2022a). In some occasions, this spatial horizontal resolution can be as small as 333 m or as large as 5 km (Prosper et al., 2019). Wind farm parameterizations are used within these models to represent the effects of wind turbines that occur at the subgrid scales (Veers et al., 2019). Historically, numerical weather prediction models have not been considered the models of choice for evaluating yearly power production or wake loss estimates from wind farms due to their relatively high computational cost. However, recent advancements in computational resources have allowed to apply these models to longer time periods (Akhtar et al., 2021; Borgers et al., 2024). In numerical

weather prediction models, wakes are not explicitly prescribed. Instead, wake dynamics are determined by the atmospheric flow field, where the mean flow is explicitly resolved at the grid scale for the mesoscale model and subgrid-scale turbulence is represented through parameterizations. In these models there are no explicit assumptions about wake propagation, recovery or superposition but the resolution remains insufficient to resolve intra-farm wake interactions down to the turbine scale (< 1 km).

Fast-running engineering models, on the other hand, have been widely used to estimate the yearly production and wake losses of wind farms, due to their very low computational cost (Peña et al., 2018). The computational cost of most engineering wake models scales linearly with the number of turbines and is therefore generally not a limiting factor when modeling large wind farm clusters. Instead, the main limitation of engineering wake models lies in the assumptions and simplifications used and how these assumptions remain valid for large wind farms and farm–farm wakes. Engineering wake models can be categorized into bottom-up, top-down, and coupled approaches. Bottom-up models simulate wakes at turbine scale and combine individual wakes to represent farm-scale effects (Bastankhah and Porté-Agel, 2014; Katic et al., 1986). These models perform well for intra-farm wakes but often predict a faster recovery of wakes than observed for large wind farms, leading to an underestimation of farm–farm effects (Fischereit et al., 2022b). Top-down models describe the impact of a wind farm on the atmospheric boundary layer as a whole and are better suited to capture the total momentum deficit induced by large wind farms, but generally lack flow heterogeneity dependence (Emeies, 2010; Antonini and Caldeira, 2021). Coupled approaches aim to combine turbine scale wake formulations with boundary layer information, offering improved physical consistency at the cost of increased complexity and calibration requirements (Stevens et al., 2015; Nygaard et al., 2020).

Although there have been previous comparisons between numerical weather prediction models and fast-running engineering models (Hansen et al., 2015; Fischereit et al., 2022b), they have not been conducted over an extended time period. Fischereit et al. (2022b) found that mesoscale models are able to accurately estimate the mean wind speed deficit but incur a higher error in estimating peak wind speed deficits, which can be partly attributed to their limited ability to resolve intra-farm wake effects. On the other hand, most engineering wake models perform well for intra-farm wakes but less so for farm-farm wakes, as they indicate a faster recovery of wind-speed deficits, particularly at longer downstream distances. Fischereit et al. (2022b) suggest that engineering wake models could be enhanced in estimating farm-farm wakes with the availability of more calibration data. Recently, new developments have been proposed to reduce the underestimation of fast-running engineering models to better represent farm-farm wakes (Pedersen et al., 2022; Bay et al., 2023).

Despite these advances, it remains unclear which modeling approach (numerical weather prediction model vs fast-running engineering wake models) provides more reliable long term estimates of wake impacts for large offshore wind farm clusters. Since no validation data are available within the scope of this study to establish a ground truth, the objective is not to identify a single best-performing model. Instead, comparing wake predictions from different model approaches allows the uncertainty associated with farm–farm wake assessments to be quantified. Such a comparison makes it possible to assess the spread in integrated metrics, such as annual energy production and wake-induced losses, and to identify the atmospheric factors, such as wind speed, wind direction and atmospheric stability that drive differences between model predictions.

To address this gap, this study examines the annual mean and sub-annual variability of wake effects induced by a planned wind farm cluster on surrounding operational wind farms. Wake impacts are predicted using both a numerical weather predic-

tion model (Part I) and commonly used fast-running engineering wake models (Part II). While both approaches are suitable for longer-term analyses, a systematic comparison over a full, meteorologically representative year has so far been lacking. This comparison is conducted for the planned Princess Elisabeth (PE) wind farm cluster, which will be constructed in the near future in the Belgian part of the North Sea. The year under investigation is the most meteorologically representative of the past 30 years (see Part I). This allows for a realistic assessment of the impact of wakes on adjacent operational wind farms. This study only includes commonly used wind farm parameterization and engineering wake models using standard calibration parameters, even though some models or calibration parameters may perform better under specific conditions.

This paper constitutes Part II of a two-part study investigating wake impacts of offshore wind farm clusters. While Part I focuses on the characterization of annual mean and sub-annual wake effects using a numerical weather prediction model, the present paper (Part II) extends this analysis by comparing numerical weather prediction results with commonly used fast-running engineering wake models. By comparing the results of these different model strategies, this study aims to quantify the spread in predicted wake impacts and to identify key drivers of model approach discrepancies, thereby providing insight into the uncertainty associated with long term farm-farm wake assessments.

2 Material and methods

The materials and methods presented in this section are applied to the new Princess Elisabeth (PE) wind farm cluster and existing adjacent wind farms. However, the same methodology can be extrapolated to study other farm-farm interactions.

2.1 Study area and period

The study area and period are identical to Part I of this study and consist of the meteorological year 2016, modeling the new 3.5 GW Princess Elisabeth (PE) wind farm cluster of 15 MW turbines together with the existing adjacent wind farms (Fig. 1). Three configurations are considered for both numerical models: (i) a reference case without wind farms ("no WF"), (ii) only the existing wind farms ("without PE"; black dots in Fig. 1), and (iii) both the existing wind farms and the new PE wind farms ("with PE"; black and red dots in Fig. 1). In Part II of the paper we will only focus on the effect of PE on the Belgian–Dutch (BE–NL) wind farm cluster, as such for the fast-running engineering models only these turbines are modeled, while all adjacent wind farms are modeled within WRF.

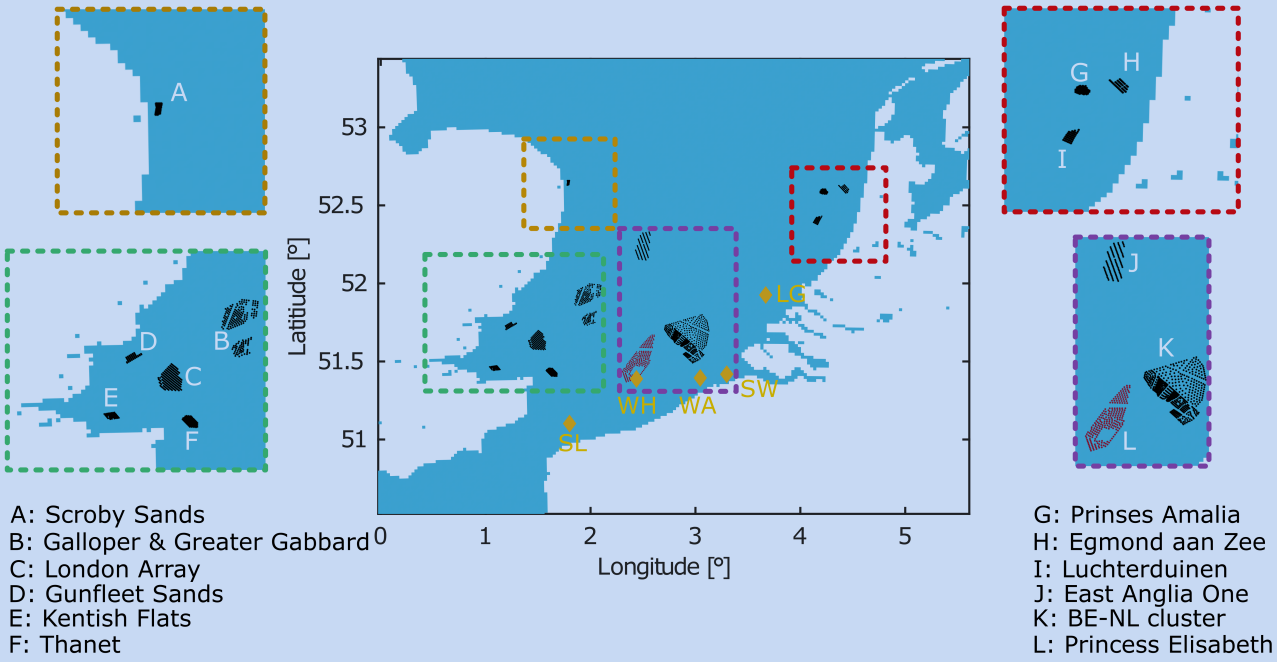


Figure 1. Location of the new Princess Elisabeth wind farms (red dots) and the existing wind farms (black dots) within the southern North Sea. Yellow diamonds show the location of measurement masts used for the validation of the WRF setup in the companion paper I.

2.2 Numerical models

2.2.1 WRF

Simulations are performed using the Weather Research and Forecasting (WRF) model v4.3 (Skamarock et al., 2008) with the setup described in Part I. The wind farm parameterization used is the Fitch scheme (Fitch et al., 2012).

2.2.2 Fast-running engineering wake models

The engineering wake modeling is conducted using FLORIS v4.4 (NREL, 2025), an open-source wake-modeling toolbox developed by the National Laboratory of the Rockies (NLR). FLORIS provides state-of-the-art engineering wake modeling capabilities, including tools for annual energy production estimations and wake steering optimization.

An ensemble of commonly used classical and more recent wake deficit models is employed in this study to provide a comparison with the numerical wearther prediction model WRF.

As a classical bottom-up engineering approach, the Jensen model (Katic et al., 1986) is included. The Jensen model assumes that the wake expands as a cone with a fixed linear expansion constant, k_{w}, independent of the local turbulence intensity (TI). In this study, two values are considered for the wake decay coefficient (1) a "standard" value $k_w = 0.04$ and (2) a reduced value

$k_w = 0.02$, following recent recommendations based on a large-scale benchmark over an entire fleet of offshore wind farms (Nygaard et al., 2022). We note that stability dependent formulations for the wake spreading rate in the Jensen model have been proposed, but are not applied in this study to keep the number of wake model representations constrained (Peña et al., 2016).

The Gaussian wake model proposed by Bastankhah and Porté-Agel (2014), hereafter referred to as Gauss-BPA, is included as a more recent engineering wake formulation. In this model, the wake is represented by a Gaussian velocity deficit whose width depends linearly on the ambient turbulence intensity, $\mathrm{TI}_{\mathrm{amb}}$, through a wake growth rate defined as

$$k^* = k_a \, \mathrm{TI}_{\mathrm{amb}} + k_b. \tag{1}$$

The Gauss-BPA model is used with its out-of-the-box calibration parameters, namely $k_a = 0.38$ and $k_b = 0.004$.

In addition to these conventional engineering models, the TurbOPark model (Pedersen et al., 2022) is considered. TurbOPark was specifically developed to mitigate excessive wake recovery in long-distance wake development, including farm-farm interactions, by means of a modified turbulence recovery scheme. The model incorporates a non-linear wake expansion that is sensitive to the local turbulence intensity and its downstream decay, given by

$$\frac{\mathrm{d}\sigma_{\mathrm{w}}(x)}{\mathrm{d}x} = A \, \mathrm{TI}(x) = A \sqrt{\mathrm{TI}_{\mathrm{amb}}^2 + \mathrm{TI}_{\mathrm{w}}^2(x)}, \tag{2}$$

where σ_w denotes the characteristic wake width and A is a calibration constant. The local turbulence intensity $\mathrm{TI}(x)$ at a downstream distance x from the turbine is computed as the quadratic sum of the ambient turbulence intensity $\mathrm{TI}_{\mathrm{amb}}$ and the wake-added turbulence intensity $\mathrm{TI}_{\mathrm{w}}(x)$, whose evolution is modeled following Frandsen (2007). The TurbOPark model is run using the default expansion coefficient $A = 0.04$ as well as the value $A = 0.06$, as proposed by van der Laan et al. (2022), who show that the default parameter tends to overestimate wake effects.

Finally, the Cumulative Curl model (Bay et al., 2023) is included as a wake model specifically designed for large wind-farm arrays. The Cumulative Curl model builds upon the Gauss-Curl Hybrid (GCH) model (King et al., 2021) by incorporating cumulative wake deflection and recovery mechanisms that account for the superposition of multiple upstream wakes. It introduces a set of streamwise counter-rotating vortices generated by yaw misalignment, which are accumulated across turbines to represent the combined effect of wake steering. Unlike the GCH model, which superimposes individual wakes, the Cumulative Curl model computes the combined wake effect using a momentum-conserving formulation proposed by Bastankhah et al. (2021). The wake velocity deficit is modeled using a Gaussian profile, with centerline deflection and recovery effects evolving cumulatively across the turbine array. The Cumulative Curl model retains the deflection formulation from GCH while adding secondary steering and yaw-induced recovery effects driven by the accumulated vortex structures. The Cumulative Curl model is run using default hyperparameters.

For all cases, except the Cumulative Curl model that uses its built-in superposition scheme, wake overlap is handled using the sum-of-squares freestream velocity superposition method. Turbines are aligned with the mean flow direction, and therefore no additional wake deflection model is applied. A summary of the deficit models used in this study is provided in Table 1.

Table 1. Overview of simulated cases with engineering models

Model	Hyperparameter	Reference
Gauss-BPA	default	Bastankhah and Porté-Agel (2014)
Jensen	$k_w = 0.04$	Katic et al. (1986)
Jensen	$k_w = 0.02$	Katic et al. (1986), hyperparam. following Nygaard et al. (2022)
Cumulative curl	default	Bay et al. (2023)
TurbOPark	$A = 0.04$ (default)	Pedersen et al. (2022)
TurbOPark	$A = 0.06$	Pedersen et al. (2022), hyperparam. following van der Laan et al. (2022)

FLORIS simulations are driven by meteorological conditions extracted from the noWF WRF simulations for the entire year 2016 (see Part I). These conditions include wind speed, wind direction, and Turbulence Intensity (TI). The noWF velocity field is provided to FLORIS using two different inflow setups. The first setup assumes horizontally homogeneous inflow and retrieves the wind speed from a single probe point located at the geographic center of the BE–NL cluster at an altitude of 96 m. In contrast, the heterogeneous inflow configuration accounts for spatial variability in the incoming flow, arising from coastal gradients or large-scale synoptic structures.

In the heterogeneous configuration, FLORIS' built-in implementation described by Farrell et al. (2021) is used. Specifically, the noWF velocity field at 96 m height is extracted at the WRF grid points and fed to FLORIS. For each wind turbine, FLORIS initializes the local inflow wind speed by performing a linear barycentric interpolation of the WRF wind speed field. Wake velocities downstream of each turbine are then computed following the standard FLORIS wake modeling approach, but using this locally interpolated inflow wind speed as the initial condition. No vertical interpolation is applied since both vertical wind shear and veer are omitted in the present study.

A portion of the engineering wake model simulations assume a time-varying TI estimated based on the noWF WRF data following Larsén (2024), which proposes to use the Kaimal turbulence spectrum to approximate the wind speed component variances, σ_u, σ_v, and σ_w, at given heights and wind speeds. Empirical ratios between σ_u and other components then allow to transform the TKE extracted from WRF into the along-wind standard deviation. The ambient TI can then be estimated as

$$\mathrm{TI}_{\mathrm{amb}} = \frac{\sigma_u}{\overline{U}} = \frac{1}{\overline{U}}\sqrt{\frac{2\,TKE}{1+\alpha^{-1}+\beta^{-1}}} \tag{3}$$

with $\overline{U}$, the mean wind speed over the averaging period at the height of interest and α and β, empirical eight and wind speed dependent coefficient determined based on Kaimal turbulence spectra. Integrating this TI correction strategy was however shown not to affect significantly the estimated TI compared to the classical approach, for which $\alpha = 1$ and $\beta = 1$.

Four different FLORIS simulation setups are subsequently considered:

- *Homogeneous FLORIS with fixed TI:* A time-varying and spatially homogeneous wind field is assumed in FLORIS, constructed from the wind speed and direction at 96 m altitude at the geographic center of the BE–NL wind farm cluster,

taken from the no WF WRF simulation (Part I). Turbulence intensity is fixed in space and time at 6%, a typical value for the offshore North Sea area.

- *Homogeneous FLORIS with varying TI:* A time-varying and spatially homogeneous wind field and TI is assumed in FLORIS, constructed from the wind speed, wind direction and TI at 96 m altitude at the geographic center of the BE–NL wind farm cluster, taken from the no WF WRF simulation (Part I). This setup aims at evaluating whether incorporating temporal variability in ambient turbulence resulting from changes in different atmospheric conditions improves the representation of wake recovery.

- *Heterogeneous FLORIS with fixed TI:* A time-varying and spatially heterogeneous wind speed field is assumed in FLORIS, constructed from the wind speed at 96 m altitude taken from the no WF WRF simulation (Part I). Wind direction is kept spatially homogeneous and time-varying, constructed from the no WF WRF simulation at 96 m altitude at the geographic center of the BE–NL wind farm cluster (Part I). Turbulence intensity is fixed in space and time at 6%, a typical value for the offshore North Sea area.

- *Heterogeneous FLORIS with varying TI:* A time-varying and spatially heterogeneous wind speed field is assumed in FLORIS, constructed from the wind speed at 96 m altitude taken from the no WF WRF simulation (Part I). Wind direction is kept spatially homogeneous and time-varying, constructed from the no WF WRF simulation at 96 m altitude at the geographic center of the BE–NL wind farm cluster (Part I). A time-varying and spatially homogeneous TI is assumed, constructed from TI at 96 m altitude at the geographic center of the BE–NL wind farm cluster, taken from the no WF WRF simulation (Part I).

All four setups of the engineering wake models are run in a time-series mode with a 30-min resolution for one full year (2016 selected in this study based on analysis in Part I), where each simulation time step is treated as quasi-steady and independent. Consequently, the model does not account for wake advection or temporal effects in wake propagation contrary to WRF. As noted previously, not all wind farms in the North Sea are modeled, for the engineering models used in this study only those belonging to the BE-NL and PE wind farm cluster are included. This reduced domain of not including all North Sea wind farms allows for the simulation of twelve cases (three layouts (no WF, with PE and without PE similar to WRF) combined with four input setups described above) capturing the dominant inter-farm wake losses of the PE wind farm cluster on the BE-NL wind farm cluster.

2.3 Wake energy losses

Wake energy losses in Part II are evaluated using the same conceptual framework as in Part I (section 2.5), distinguishing between internal, total (internal + external), and external wake losses. For both WRF and the engineering wake model simulations, wake losses are computed from averaged power rather than from instantaneous loss time series. Depending on the analysis, the averaging period may correspond to the full simulation year, individual months, or subsets of the data conditioned on wind speed, wind direction, atmospheric stability, or a combination thereof. To enable a direct comparison between WRF

and the engineering wake models, all wake energy losses are normalized using the same reference energy obtained from the noWF WRF simulation.

Small differences between the wake energy losses reported in Part I and those obtained in Part II arise from differences in temporal resolution. While the WRF analysis in Part I uses 10 min output, the engineering wake model simulations in Part II operate on 30 min mean conditions. For consistency, the WRF power output used in Part II is therefore aggregated to 30 min resolution by averaging consecutive 10 min samples. This difference in temporal aggregation can lead to small deviations in the estimated wake losses (e.g., WRF internal wake losses in Part I and Part II of $42.01 \pm 0.28\%$ and $41.46 \pm 0.24\%$, respectively), but does not affect the comparison between WRF and the engineering wake models presented in this study.

Additionally, it should be noted that the definition of internal wake energy losses used for the WRF simulations (Part I) differs from the definition in engineering wake models (Part II). In WRF, the internal wake energy losses represent the energy losses experienced by the existing wind farms in the absence of the PE wind farm cluster. As a result of the simulation setup, it is not possible to isolate wake effects generated solely by turbines within the same BE-NL wind farm. Consequently, the internal wake energy losses derived from WRF include inter-farm wake interactions among the existing wind farms, but exclude wake effects originating from the newly introduced PE wind farm cluster. In contrast, the engineering wake models apply the strict definition of internal wake losses, accounting only for wake effects generated within the BE-NL wind cluster, since no other wind farms were modeled. This can result in slight differences between the model approaches.

3 Results and discussion

Results are presented either at the wind farm level or at the grid cell level, the latter refers to individual horizontal grid cells of the WRF model. As multiple turbines may be located within a single grid cell, all wind farm quantities evaluated at the grid cell level (e.g., power or wake energy losses) represent aggregated model results rather than turbine resolved values. Since the engineering wake model results are computed at the turbine level, these results are aggregated to the WRF grid cell to enable a direct comparison.

3.1 Spatiotemporally averaged power

We next quantify the differences between the engineering wake models and their various setups (homogeneous or heterogeneous inflow, fixed or varying turbulence intensity) relative to WRF. Prior to this comparison, a verification of the noWF case was performed to ensure consistent use of WRF inputs in the engineering wake models (Appendix A). Since no observational data are available within the scope of this study, the aim is not to identify the best-performing model, but rather to assess the spread between models. To this end, we use three performance statistics: the coefficient of determination R^2, the root-mean-square error (RMSE), and the mean bias. The bias expresses the average difference between the power estimated by the engineering wake models and WRF, where a positive bias indicates that the engineering model predicts higher power than WRF, whereas a negative bias indicates a lower power. In contrast, RMSE reflects the typical size of the deviations between the two time series, and R^2 describes how well the engineering model captures the temporal variability seen in WRF.

Table 2 summarizes these statistics for all engineering wake models and the different setups for the simulations without the PE cluster. It should be noted that all engineering wake models and their different setups exhibit a positive bias relative to WRF, ranging from approximately 0.18 GW for TurbOPark ($A = 0.04$) to 0.342 GW for Jensen ($k_w = 0.04$). Table 2 shows that, among the examined engineering wake models, TurbOPark with a spreading parameter of $A = 0.04$ provides the closest agreement with WRF, with RMSE values as low as 0.356 GW, a bias of 0.18 GW and R^2 values up to 0.917. By comparison, the Jensen model with $k_w = 0.04$, shows the largest deviations from WRF across all metrics, with a RMSE value of 0.617 GW, bias of 0.342 GW and R^2 value 0.752. The same behaviour is observed in the simulations including the PE cluster (Table B1).

When comparing the different model setups (homogeneous or heterogeneous inflow, fixed or varying turbulence intensity) in Table 2, the heterogeneous inflow combined with varying turbulence intensity generally produces the closest agreement with WRF. However, the relative importance of inflow conditions and turbulence intensity depends on both the performance metric and the engineering wake model. For RMSE and R^2, improvements associated with inflow conditions typically amount to reductions of approximately 0.02-0.03 GW in RMSE and increases of about 0.01–0.02 in R^2 when comparing homogeneous and heterogeneous inflow conditions at both fixed and varying turbulence intensity. In contrast, the impact of turbulence intensity on RMSE and R^2 is more model dependent: for Gauss-BPA, switching from fixed to varying turbulence intensity under both homogeneous and heterogeneous inflow conditions reduces RMSE by approximately 0.03 GW, exceeding the corresponding improvement due to inflow conditions, whereas for the Jensen model the effect of turbulence intensity is negligible and improvements are primarily driven by inflow conditions.

For the mean bias, the sensitivity to the setup is model dependent. Gauss-BPA shows a strong dependence on turbulence intensity, with a reduction in bias of approximately 0.01 GW when switching from fixed to varying turbulence intensity, while the bias is small going from homogeneous to heterogeneous inflow. In contrast, TurbOPark shows an almost invariant bias across all setups, with differences below 0.001 GW, indicating that its bias is largely controlled by the wake model formulation itself. The Jensen model exhibits a weak sensitivity on the bias to both inflow conditions and turbulence intensity, consistent with its formulation, in which wake recovery does not explicitly depend on turbulence intensity.

Differences between engineering wake model formulations reach a maximum of 0.26 GW in RMSE, 0.17 in R^2, and 0.16 GW in bias relative to WRF, whereas variations associated with inflow conditions or turbulence intensity within a given engineering wake model remain below 0.03 GW in RMSE, 0.02 in R^2, and 0.01 GW in bias. This indicates that the engineering wake model formulation constitutes the dominant source of variability in comparison to WRF, while setup choices provide a secondary influence on model performance.

Based on these findings, TurbOPark with $A = 0.04$ is used as the representative engineering wake model in subsequent analyses when a single wake model is considered. This choice does not imply that TurbOPark provides the most accurate representation of wake effects, given that no observational validation data are available and WRF cannot be regarded as a ground truth. Rather, TurbOPark is selected because it exhibits the closest overall agreement with WRF within a consistent modeling framework, providing a single reference for further comparative analysis. Likewise, the heterogeneous inflow with varying turbulence intensity setup is selected as the preferred configuration for the remainder of the study when a single setup is considered.

Table 2. R^2, RMSE [GW], and mean bias [GW] for the different engineering wake models (without PE) compared against WRF, shown for the four model setups: homogeneous fixed TI, homogeneous varying TI, heterogeneous fixed TI, and heterogeneous varying TI. Colour shading highlights relative performance of the engineering wake model within each metric (smallest = dark green, largest = dark red). Typographic emphasis (smallest = bold, largest = italic & underlined) highlights relative performance of the setups of the engineering wake models within each metric.

	Homogeneous						**Heterogeneous**					
	Fixed TI			Varying TI			Fixed TI			Varying TI		
Model	R^2	RMSE	Bias	R^2	RMSE	Bias	R^2	RMSE	Bias	R^2	RMSE	Bias
Gauss-BPA	*0.845*	*0.488*	*0.218*	0.864	0.457	0.207	0.858	0.468	0.218	**0.875**	**0.439**	**0.207**
Cumul. Curl	*0.879*	*0.432*	0.215	0.892	0.407	**0.212**	0.892	0.407	*0.215*	**0.905**	**0.383**	0.213
Jensen $k_w = 0.02$	0.842	0.493	*0.213*	*0.839*	*0.497*	0.211	0.853	0.476	**0.210**	**0.855**	**0.472**	0.212
Jensen $k_w = 0.04$	0.752	*0.617*	**0.342**	0.755	0.614	0.344	*0.771*	**0.593**	0.344	**0.769**	0.596	0.342
TurbOPark $A = 0.04$	*0.897*	*0.399*	*0.180*	0.905	0.383	0.180	0.910	0.372	**0.179**	**0.917**	**0.356**	0.180
TurbOPark $A = 0.06$	*0.858*	*0.468*	0.255	0.866	0.454	*0.255*	0.872	0.444	**0.254**	**0.880**	**0.430**	0.255

3.2 Time dependent behavior

3.2.1 Total farm power

The temporal evolution of the total BE-NL wind farm cluster power for WRF and the engineering wake models in the simulations without PE is shown in Fig. 2. The time series further confirms the results obtained from the spatiotemporally averaged comparison in Section 3.1. Over the year the engineering wake models estimate higher total wind farm power compared to WRF. This indicates smaller wake losses in the engineering models relative to WRF, consistent with previous studies showing that WRF with the wind farm parameterization of Fitch et al. (2012) produces stronger wake deficits and reduced power production compared to engineering wake models (Fischereit et al., 2022b, 2025). Quantitatively, the WRF power estimates fall within the envelope of the engineering wake models for 40% of the simulated hours, while for the remaining 60% of the time WRF lies outside this range, indicating periods of stronger disagreement between modeling approaches.

The results for the simulations with PE (Fig. C1) are also showing that the engineering wake models estimate higher total power compared to WRF. In this case, WRF power estimates fall within the envelope of the engineering wake models for 38% of the simulated hours, while for 62% of the time WRF lies outside this range. The increased fraction of hours suggests that the inclusion of the PE cluster increases the differences between the modeling approaches. This could originate from the fact that engineering wake models are primarily calibrated for intra-farm wakes and may be less suited to represent farm–farm wake interactions without additional tuning (Nygaard et al., 2020; Fischereit et al., 2022b).

Furthermore, also consistent with the spatiotemporally averaged comparison in Section 3.1, the temporal comparison in Fig. 2 shows that differences between wake engineering models are larger than differences by different model setups. This is depicted by the narrow spread between different setups of a given engineering wake model (Fig. 2 (b,d,f)) compared to the larger spread between the ensemble of the engineering wake models (Fig. 2 (a,c,e)).

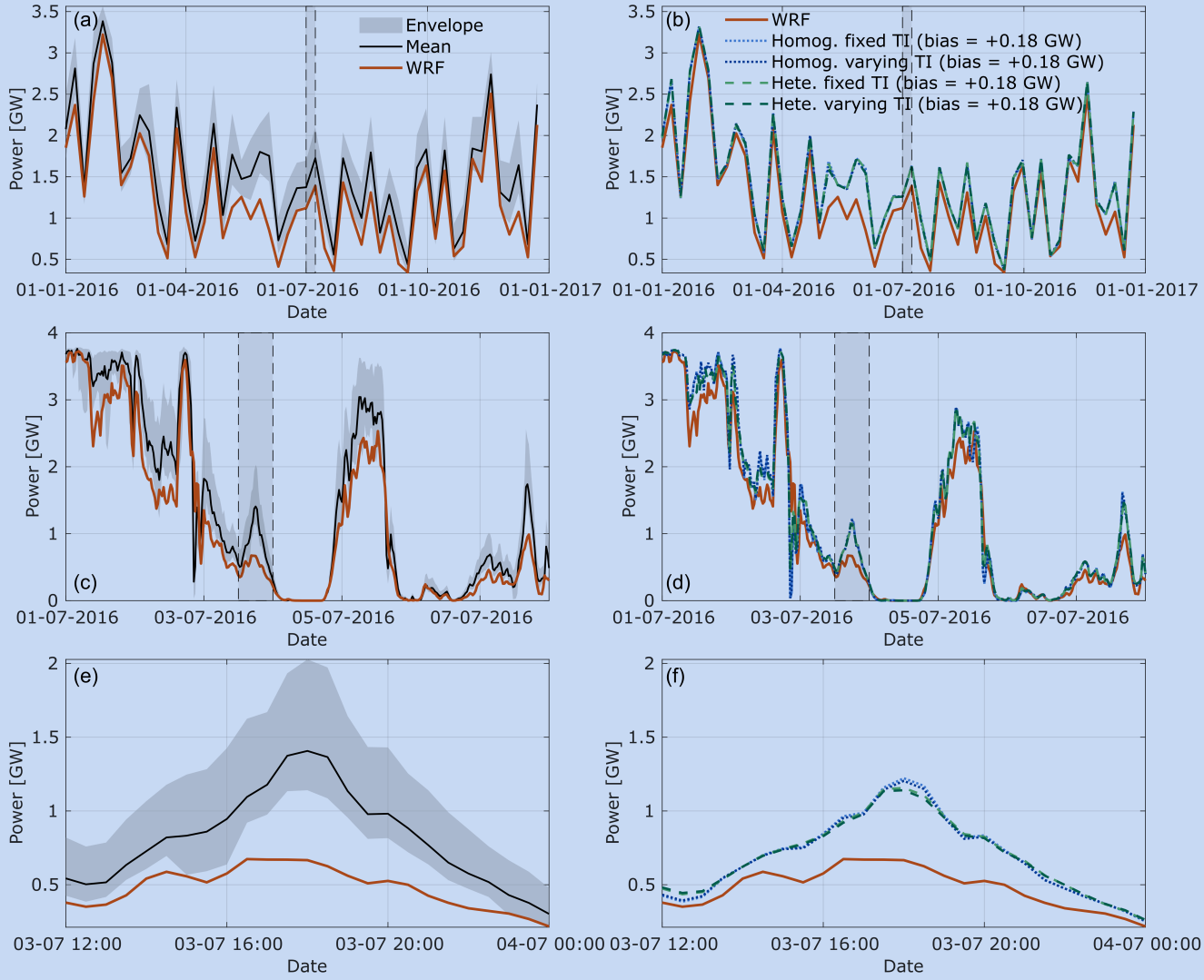


Figure 2. Total power (GW) for the BE–NL offshore wind farm cluster for simulations without PE. Shown are WRF (without PE), and the mean and envelope of all engineering models (a,c,e), and the different configurations of Turbopark with induction factor A=0.04 (b,d,f). The top row (a,b) shows weekly averages computed from 30-min data, the middle row (c,d) shows a one-week zoom (1–7 July 2016) at 30 min resolution, and the bottom row (e,f) shows a twelve-hour zoom (3 July 2016) also at 30 min resolution. The dashed box shows the time period zoom within the longer time series. The bias is calculated as the engineering wake model minus WRF.

3.2.2 Grid cell power

A grid cell refers to an individual horizontal WRF model grid cell (for details of simulation setup see Part I) and represents the aggregated response of all turbines located within that cell. The same spatial aggregation is applied to the engineering wake

model results. Grid cell power at three locations (Fig. 3 (a)) is compared between the engineering wake models and WRF, corresponding to the farm center, a coastal site, and a more offshore site.

In contrast to the total farm power time series (Fig. 2), the grid cell power time series (Fig. 3) exhibits larger differences between the homogeneous and heterogeneous setups. At the farm center (Fig. 3 (d,e)), both configurations yield identical results, as expected. At the coastal location (Fig. 3 (b,c)), introducing heterogeneity improves agreement with WRF, reducing the bias from 0.9 MW to 0.7 MW. In contrast, at the offshore location (Fig. 3 (f,g)), the bias increases from 1.0 MW to 1.1 MW. To interpret these differences, it is useful to distinguish between wake biases and wind speed gradient biases, this latter in the homogeneous inflow setups.

The wake bias shows higher power production estimates by the engineering wake models compared to WRF, for both homogeneous and heterogeneous inflow setups. In addition, the homogeneous configuration is affected by a wind speed gradient bias, because the inflow is derived from wind conditions at a single grid point (at the spatial center of the wind farm) and does not represent the spatial wind speed gradients resolved by WRF. Depending on the local wind speed, this wind speed gradient bias can partially compensate or increase the wake bias when the engineering models are compared with WRF.

At the coastal grid cell, the homogeneous inflow has a higher wind speed compared to the WRF grid cell wind speed, which adds to the wake bias and yields a larger total power bias. Introducing heterogeneity reduces this larger inflow relative to WRF, thereby reducing the power bias. At the offshore grid cell, the homogeneous inflow has lower wind speeds compared to the WRF grid cell wind speed, which compensates the wake bias and leads to a smaller apparent power bias. Accounting for heterogeneity corrects the inflow toward the WRF wind speed. This removes the compensating inflow error present in the homogeneous configuration, revealing the full wake bias and therefore increasing the total power bias compared to WRF. These changes in bias thus reflect the presence or removal of wind gradients bias compensation in comparison to WRF.

Although bias response to the inclusion of inflow heterogeneity differs between regions, the spatiotemporally aggregated comparison in Section 3.1 shows smaller biases compared to WRF for the heterogeneous inflow setup. Accounting for heterogeneity reduces inflow biases associated with wind speed gradients, while local increases or decreases in bias partially cancel when integrated over the full wind farm and year. As a result, the total bias is reduced compared to the homogeneous inflow setup, even though heterogeneity can locally increase the bias at individual grid cells. We nonetheless note that including heterogeneity is expected to improve the physical realism of the modeling setup. Even in cases where the apparent bias increases, the heterogeneous configuration remains more faithful to the underlying flow physics, as it better represents spatial variability in the inflow. The remaining discrepancies therefore primarily reflect differences in wake-model response between the WRF-based inflow and the engineering wake model implementation.

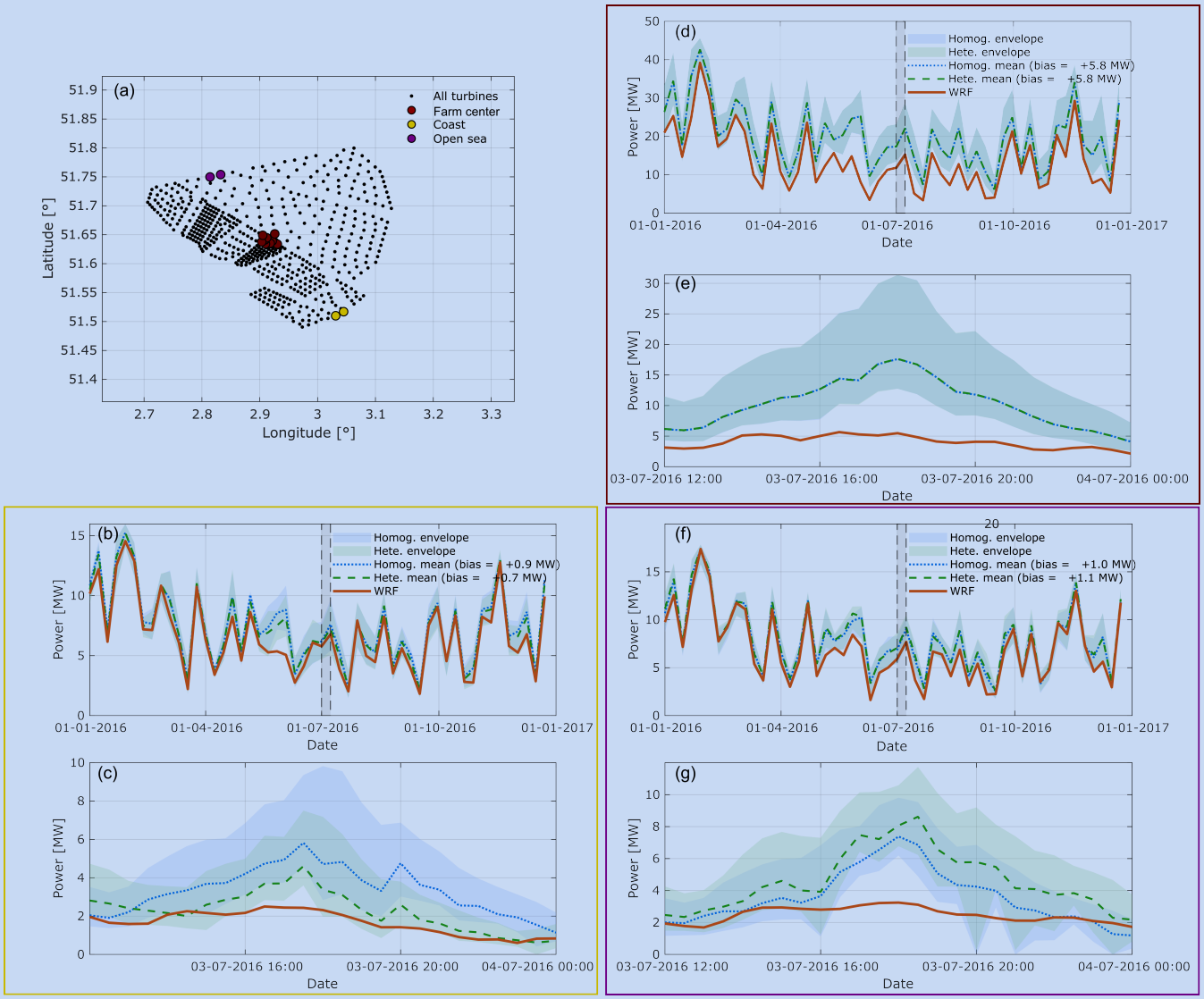


Figure 3. Grid cell power output (MW) at three representative locations within the BE-NL wind farm cluster for simulations without PE. Panel (a) shows the locations of the selected grid cells, representing the farm center, coastal, and open-sea regions. Panels (d,b,f) show weekly averages computed from 30-min data, while panels (e,c,g) show a twelve-hour zoom on 3 July 2016 at 30-min resolution. Shown are WRF (without PE) and the mean and envelope of all engineering wake models grouped by homogeneous and heterogeneous setups. The dashed box indicates the zoomed period within the full time series. Bias is defined as the engineering wake model power minus WRF power.

3.3 Internal and external wake energy losses

3.3.1 Spatiotemporally averaged wake energy losses

Beyond the total power metrics discussed in Section 3.1, the separation of internal and external wake energy losses in Table 3 makes it possible to investigate the contributions of intra-farm and farm–farm wake effects explicitly. Table 3 shows, as presented ealier, that differences between different engineering wake models and WRF are larger compared to the different inflow setups within a given engineering wake model and WRF. For the latter, variations between homogeneous and heterogeneous and between fixed and varying TI are small and mostly within the uncertainty range.

For the internal wake energy losses, WRF predicts larger losses ($41.46 \pm 0.24\%$) than any engineering wake model across all inflow setups, which range from approximately 22% for the Jensen model with $k_w = 0.04$ to about 31% for TurbOPark with $A = 0.04$, the latter providing the closest agreement with WRF. These results are consistent with the spatiotemporally averaged power comparison in Section 3.1, where internal wake effects dominate the overall power differences between modeling approaches.

Also for the external wake losses, differences between the engineering wake models and WRF are larger than the differences from different inflow setups within a given engineering wake model. While WRF yields an external wake loss of $4.00 \pm 0.10\%$, the engineering wake models span from near-zero or slightly negative losses for Gauss-BPA and Jensen to approximately 2.5% for the Cumulative Curl and TurbOPark models. This range indicates that external wake energy loss estimates of the engineering models relative to WRF are primarily controlled by the wake model formulation. In particular, models explicitly designed to represent long-range and cumulative wake interactions, such as TurbOPark and Cumulative Curl, produce external wake losses that are closer to WRF than the more classical engineering formulations (Nygaard et al., 2020). A previous study by Fischereit et al. (2022b) has shown that WRF with Fitch et al. (2012) can provide a more realistic representation of farm–farm wake effects under specific atmospheric conditions (Fischereit et al., 2022b) compared to engineering wake models. While these findings cannot be directly generalized to the full-year simulations analyzed here, the closer agreement of TurbOPark and Cumulative Curl with WRF suggests that these models may be more suitable for representing farm–farm wake interactions than the other engineering wake models considered in this study.

Comparing internal and external wake energy losses show that although the absolute inter-model spread is larger for internal wake losses (22–31%), the relative inter-model variability is larger for external wake losses, which range from negligible or slightly negative values to about 2.5%. This highlights that the farm–farm wake estimates are more sensitive to the wake model formulation than to the estimates of intra-farm wake effects.

The slightly negative external wake energy losses obtained for Jensen with $k_w = 0.04$ and Gauss-BPA, do not represent physically negative external wake energy losses. They arise from the definition of the external wake loss relative to the no WF WRF reference that includes spatial wind speed heterogeneity, combined with the weak long-range wake deficits predicted by these models. Such negative values can only occur in wake model setups that employ the heterogeneous inflow. As Jensen and Gauss-BPA exhibit faster wake recovery, downstream wind farm power can locally approach or slightly exceed the grid-cell-averaged WRF reference, leading to small negative values.

Table 3. Spatio-temporal mean internal and external wake losses for WRF and the engineering wake models without PE. Uncertainties denote the half-width of the 95% confidence interval obtained from 1000 bootstrap resamples. All values are given in %.

	Internal Wake Loss [%]				**External Wake Loss [%]**			
	Homogeneous		**Heterogeneous**		**Homogeneous**		**Heterogeneous**	
	Fixed TI	Varying TI	Fixed TI	Varying TI	Fixed TI	Varying TI	Fixed TI	Varying TI
WRF	41.46 ± 0.24				4.00 ± 0.10			
Gauss-BPA	29.59 ± 0.20	30.18 ± 0.19	29.54 ± 0.20	30.13 ± 0.20	-0.37 ± 0.14	-0.46 ± 0.14	-0.34 ± 0.14	-0.44 ± 0.14
Cumulative Curl	30.43 ± 0.21	30.58 ± 0.21	30.36 ± 0.21	30.50 ± 0.21	$+2.59 \pm 0.04$	$+2.65 \pm 0.04$	$+2.56 \pm 0.04$	$+2.62 \pm 0.04$
Jensen $k_w = 0.02$	29.09 ± 0.22	29.21 ± 0.22	29.18 ± 0.21	29.06 ± 0.21	$+0.15 \pm 0.10$	$+0.03 \pm 0.10$	$+0.02 \pm 0.10$	$+0.09 \pm 0.10$
Jensen $k_w = 0.04$	22.35 ± 0.21	22.28 ± 0.21	22.20 ± 0.20	22.29 ± 0.20	-0.26 ± 0.10	-0.17 ± 0.09	-0.16 ± 0.09	-0.22 ± 0.10
TurbOPark $A = 0.04$	31.27 ± 0.22	31.24 ± 0.22	31.25 ± 0.21	31.21 ± 0.20	$+2.66 \pm 0.04$	$+2.79 \pm 0.05$	$+2.62 \pm 0.04$	$+2.75 \pm 0.04$
TurbOPark $A = 0.06$	27.35 ± 0.20	27.31 ± 0.20	27.31 ± 0.19	27.27 ± 0.20	$+1.76 \pm 0.03$	$+1.87 \pm 0.03$	$+1.73 \pm 0.03$	$+1.84 \pm 0.03$

3.3.2 Spatial patterns of wake energy losses

In Fig. 4, the yearly averaged results for WRF and the different engineering wake models using the heterogeneous varying TI setup are shown, together with the differences (in percent of points) in wake energy loss between each engineering model and WRF. Both the internal (top rows of Fig. 4) and external (bottom rows) wake energy losses are presented together with the performance metrics compared to WRF in Table 4.

For the internal wake losses, all engineering wake models show enhanced wake energy losses in the interior of the wind farm. While several models show comparable spatio-temporal mean internal wake losses in Table 3 (e.g. Gauss-BPA 30.13% and Cummulative Curl 30.50 %), their spatial agreement with WRF differs substantially (R^2 = 0.588 vs 0.893). In particular, Gauss-BPA and Jensen with $k_w = 0.04$ models has larger deviations and thus lower spatial correspondence with WRF. These results indicate that similar spatiotemporal averaged internal wake energy losses can arise even if the spatial distributions are different. TurbOPark and Cumulative Curl reproduce both the magnitude (Table 3) and the spatial pattern (Table 4) of the internal wake losses more consistently compared to WRF.

For the external wake energy losses, the differences between the spatial distribution is larger compared to internal wake energy losses, this can also be seen from Table 4 (e.i. R^2 =0.127 to 0.952 for Gauss-BPA and TurbOPark with $A = 0.04$ respectivily). Only TurbOPark and Cumulative Curl reproduce spatial patterns that are similar to WRF, whereas the other engineering wake models show weak spatial correspondence and are not able to represent the farm–farm wake. This was also represented by the spatiotemporal results in Table 3.

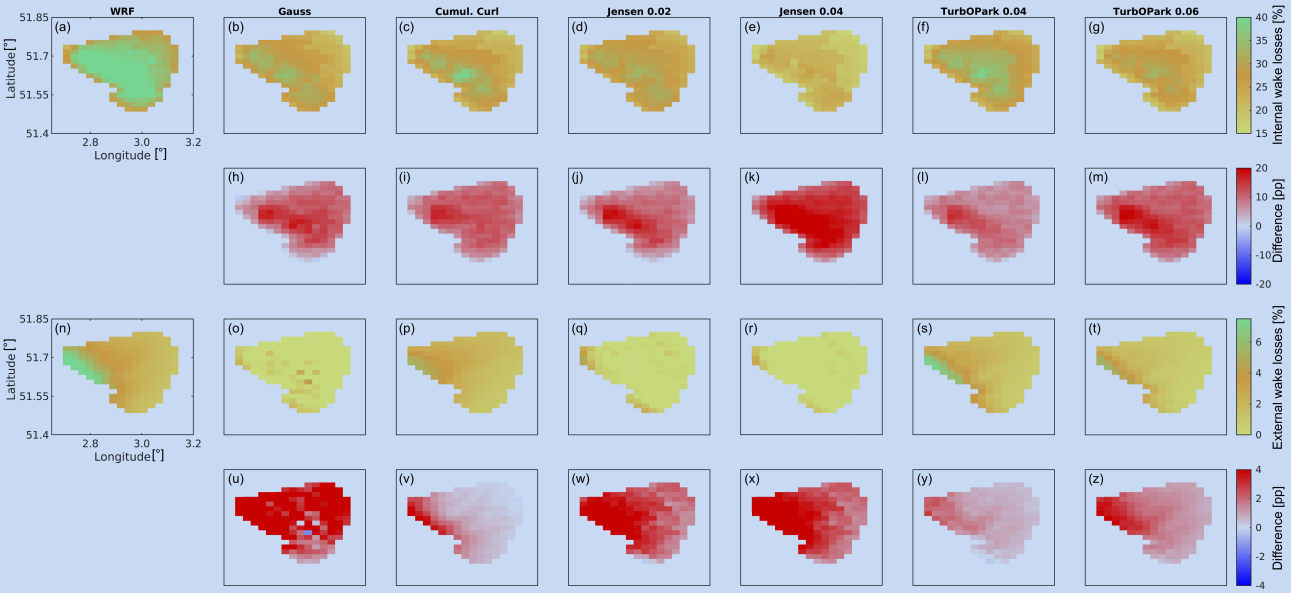


Figure 4. Temporal mean internal (a-g) and external (n-r) wake energy losses for WRF and all engineering wake models with the heterogeneous varying TI inflow setup. The second (h-m) and fourth (u-z) rows show the corresponding differences in percentage points between each engineering wake model and the WRF simulation for internal and external wake losses, respectively.

Table 4. R^2, RMSE [pp], and mean bias [pp] for the different engineering wake models (without PE) compared against WRF, shown for the heterogeneous with varying TI inflow setup. Bias is defined as (engineering model − WRF).

	Internal wake Loss [%]			**External Wake Loss [%]**		
Model	R^2	RMSE	Bias	R^2	RMSE	Bias
Gauss-BPA	0.588	10.628	−9.848	0.127	4.597	−4.151
Cumulative Curl	0.843	10.593	−10.234	0.911	1.354	−0.952
Jensen $k_w = 0.02$	0.750	10.315	−9.565	0.323	3.425	−3.052
Jensen $k_w = 0.04$	0.526	16.550	−15.875	0.200	3.718	−3.308
TurbOPark $A = 0.04$	0.893	8.432	−8.030	0.952	1.105	−0.959
TurbOPark $A = 0.06$	0.864	12.087	−11.695	0.939	1.912	−1.706

3.3.3 Monthly farm wake energy losses variations

Fig. 5 and Fig. 6 show the monthly variation of internal and external wake energy losses from the engineering wake models, expressed as percentage point [pp] differences compared to WRF. Results are shown for three groups (a) comparison of inflow conditions, (b) TurboPark $A = 0.04$ configurations, and (c) heterogeneous inflow with varying TI for all engineering wake models. For both the internal and external wake energy losses a seasonal pattern is present, with larger differences between

the modeling approaches during summer than during winter months. This is also visible in the time series of total wind farm power and grid cell power, respectively, Fig. 2 and Fig 3.

For the internal wake energy losses (Fig. 5), wintertime model approach differences range from 4 to 20 pp, increasing to 19–31 pp during the summer months, with differences between engineering wake models itself being larger compared to differences from inflow setups. For the external wake energy losses (Fig. 6), wintertime model approach differences range from 1 to 6 pp, increasing to 4–11 pp in summer. Although external wake energy losses differences between model approaches are smaller in absolute terms compared to internal wake energy losses, the WRF external energy losses are also small and therefore results in larger relative differences. In addition, the spread between wake model formulations is relatively larger for external than for internal wake losses, reflecting the higher sensitivity of farm–farm wake interactions to engineering wake model formulation. Some slight light negative external wake energy losses are observed during some periods and for certain models, consistent with earlier findings, and likely caused by the no WF WRF reference.

In Part I, both internal and external wake energy losses show seasonal variability, linked to changes in wind speed and atmospheric stability. The results presented here in Figs. 5 and 6 further show that these summer conditions are associated with increased differences between WRF and engineering wake model estimates (modeling approaches) for both internal and external wake energy losses. During summer, lower wind speeds and more frequent stable stratification lead to reduced turbulent mixing and slower wake recovery, conditions that are accounted for in WRF through stability dependent planetary boundary layer parameterisations but are only indirectly represented in engineering wake models. Consequently, these differences between modeling approaches persist downstream and amplify deviations in wake energy losses. Engineering wake models such as TurboPark and the Cumulative Curl model, which incorporate turbulence-dependent wake recovery and wake expansion, tend to show closer agreement with WRF under these conditions. In addition, turbines operate less frequently in above-rated conditions during summer than in winter. Since wake effects are reduced when turbines operate above rated wind speed, agreement between WRF and engineering wake models is generally higher in winter, further contributing to the increased spread observed in summer. The increased spread observed in summer therefore suggests that improved representation of atmospheric stability and its impact on wake recovery in engineering wake models is key to reducing discrepancies with WRF.

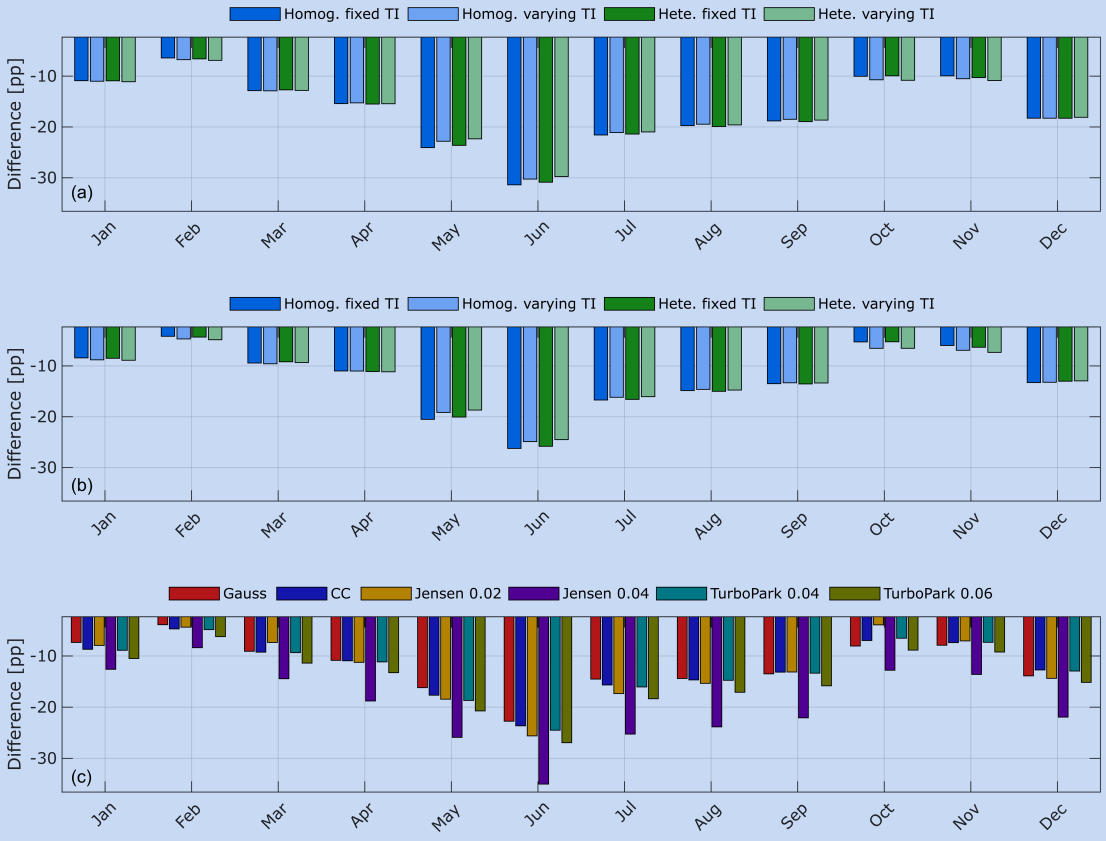


Figure 5. Monthly internal wake energy losses difference compared to WRF (in perecntage points). (a) all engineering wake models clustered by setup (homogeneous fixed TI, homogeneous varying TI, heterogeneous fixed TI, and heterogeneous varying TI). (b) TurboPark ($A = 0.04$) results for the same inflow four setups. (c) all engineering wake models corresponding to the heterogeneous varying TI setup.

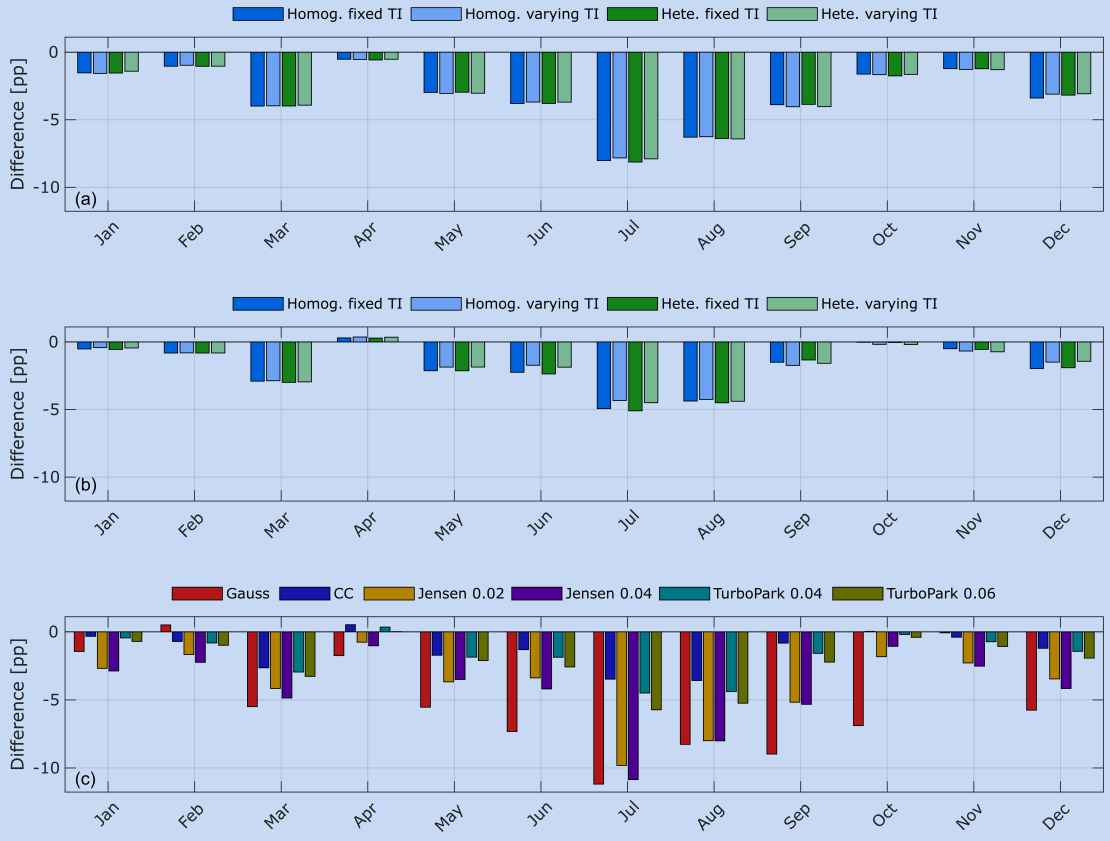


Figure 6. Monthly external wake energy losses difference compared to WRF (in perecntage points). (a) all engineering wake models clustered by setup (homogeneous fixed TI, homogeneous varying TI, heterogeneous fixed TI, and heterogeneous varying TI). (b) TurboPark ($A = 0.04$) results for the same four inflow setups. (c) all engineering wake models corresponding to the heterogeneous varying TI setup.

3.3.4 Variation with atmospheric stability

Building on the seasonal analysis from section 3.3.4, an explicit investigation on how the internal and external wake energy losses from the different modeling approaches behave across atmospheric stability classes will be discussed next (Fig. 7). How these energy losses depend on atmospheric stability classes for WRF only have been discussed in section 3.3 and 3.4 in Part I. In general Fig. 7 shows that, the differences between the modeling approached is primarily controlled by the wake modeling formulation rather than by the inflow conditions.

For the internal wake energy losses with heterogeneous varying TI inflow conditions (Fig. 7 (a)), the uncertainty ranges associated with the different engineering wake models show partial overlap with the WRF modeling approach, especially during

unstable conditions. However, differences between modeling approaches remain during stable conditions. This confirms that there is an increased sensitivity of wake recovery to stability under low turbulence regimes. Under higher turbulence conditions, turbulent mixing accelerates wake recovery, leading to closer agreement between the modeling approaches. The same can be observed from Fig. 7 (b) which isolates the effect of inflow conditions for the TurbOPark model ($A = 0.04$). In both Fig. 7 (a) and Fig. 7 (b), the uncertainty ranges of the engineering wake models and of the different inflow conditions, respectively, largely overlap, making it difficult to identify a single modeling approach or inflow configuration that is consistently closer to WRF for internal wake losses.

For the external wake energy losses when comparing the different modeling approaches under heterogeneous varying TI inflow conditions (Fig. 7 (c)), overlap between uncertainty ranges is observed across multiple stability classes and not only under unstable conditions which was the case for internal wake energy losses. However, in contrast to the internal wake energy losses, the engineering wake models themselves no longer overlap consistently over all stability classes, indicating a stronger sensitivity of external wake losses to the underlying wake formulation. In particular, models that explicitly account for turbulence dependent wake recovery and expansion, such as TurbOPark and the Cumulative Curl model, show closer agreement with WRF across stability classes.

When isolating the effect of inflow conditions for the TurbOPark model (Fig. 7(d)), the uncertainty ranges associated with the different inflow configurations overlap with each other, similar as for the internal wake energy losses (Fig. 7(b)). Nevertheless, a slightly closer agreement with WRF is found for varying TI inflow conditions compared to fixed TI inflow conditions for stable atmospheric conditions.

Overall, this analysis provides a physical explanation for the seasonal patterns discussed in Section 3.3.3, where larger differences between modeling approaches were observed during summer. The increased occurrence of stable atmospheric conditions in summer enhances the sensitivity of wake recovery to the specific wake formulation, particularly for external wakes. As a result, discrepancies between WRF and engineering wake models, and among the engineering models themselves, become more pronounced under these conditions, whereas during periods dominated by unstable stratification the enhanced turbulent mixing leads to closer agreement across modeling approaches.

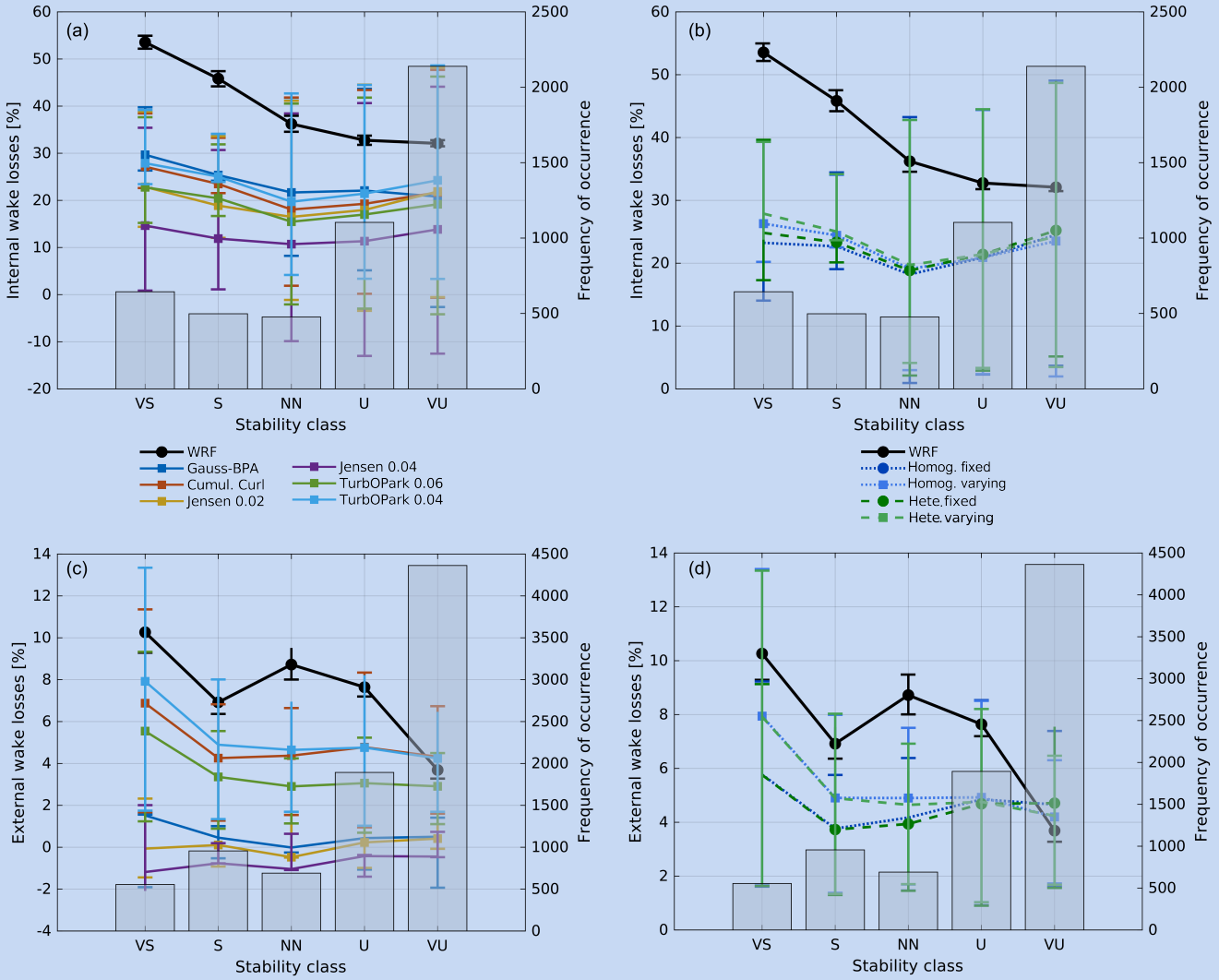


Figure 7. Spatiotemporal conditional averages of wake energy losses by atmospheric stability class (VS: very stable, S: stable, NN: near-neutral, U: unstable, VU: very unstable). (a,b) Internal wake energy losses for wind speeds between 10 and 15 ms^{-1}. (c,d) External wake losses for wind directions from 193° - 317°. Lines show engineering wake models for heterogeneous inflow and varying TI and WRF; (a,c) all models, (b,d) TurbOPark ($A = 0.04$) for all inflow setups and WRF. Bars indicate the frequency of occurrence of each stability class. The error bars represent a 95% confidence interval obtained via bootstrapping with 1000 resamples.

3.4 Flow field

445 Two flow-field snapshots are examined (Fig. 8), one case in which the flow can be considered quasi-steady and another in which the flow is strongly transient. We compare the velocity fields (wind speed and direction) generated by the TurbOPark model

($A = 0.04$, heterogeneous inflow with varying TI) with those produced by WRF for both situations. In Fig. 9, we observe that the first snapshot selected (15-03-2016) demonstrates a relatively steady behavior of both the wind speed and wind direction with a slow wind speed power ramp up. The resulting uncertainty envelopes remain quite narrow for both time series. In contrast, the second selected case (08-11-2016) depicts much wider uncertainty envelopes associated with a strong variability of the mean wind, especially regarding wind direction.

In the steady case (15-03-2016), both the spatial velocity fields (Fig. 8, top row) and the time series (Fig. 9, left) demonstrate consistent behavior. The WRF and TurbOPark flow fields exhibit similar velocity patterns: wake propagation signatures are comparable in both models, while the background velocity field in FLORIS also appears in good agreement with WRF. This spatial agreement is reflected in the temporal evolution of the power time series: the power production predicted by TurbOPark shows good correlation with WRF throughout the period. Although TurbOPark systematically predicts higher power due to faster wake recovery, both models capture comparable temporal trends, confirming that the quasi-steady flow assumption is valid in this case.

In contrast, the transient case (08-11-2016) exhibits fundamentally different behavior. As a steady-state model, FLORIS assumes that wakes propagate instantaneously across the whole domain along the wind direction measured at the central probing location of the wind farm. As a consequence, the wakes appear as coherent flow structures. In WRF, however, no such coherent wake patterns can be identified because of the strong flow heterogeneity, and rapid temporal evolution. In addition, the inflow velocity field used to drive TurbOPark (i.e. the no-farm WRF velocity field) strongly diverges from the actual velocity field in the presence of the wind farm. This may indicate that the large scale cluster partially affects how these transient events unfold across the domain.

This incapacity to account for wake dynamics is inherent to the steady nature of the typical engineering wake models used in this study. The engineering wake models in this study rely on steady, analytical formulations and do not resolve time-dependent atmospheric boundary-layer dynamics, advection, or turbulence transport. WRF solves the unsteady governing equations and explicitly represents atmospheric transport processes, thereby capturing the spatio-temporal evolution of flow structures and their impact on power generation.

To assess the specific impact of these dynamically evolving conditions, a wind-direction unsteadiness flag (WD_{flag}) is introduced to identify periods of strong directional variability. The flag is activated when the difference between the local wind direction at the wind-farm probing location and the domain-averaged wind direction exceeds a predefined threshold of $30°$.

The annual time series are then analyzed for periods where $WD_{\text{flag}} = 1$ and where turbines are operating, assuming a minimum wind-speed cutoff. This analysis indicates that such strongly transient conditions are rare, accounting for only approximately **2%** of the analyzed year. This confims that engineering wake models should exhibit good agreement with WRF for the vast majority of operational conditions. Additionally, it is worth noting that turbines are often curtailed or shut down during these transient events, further limiting the practical impact of discrepancies observed in transient cases.

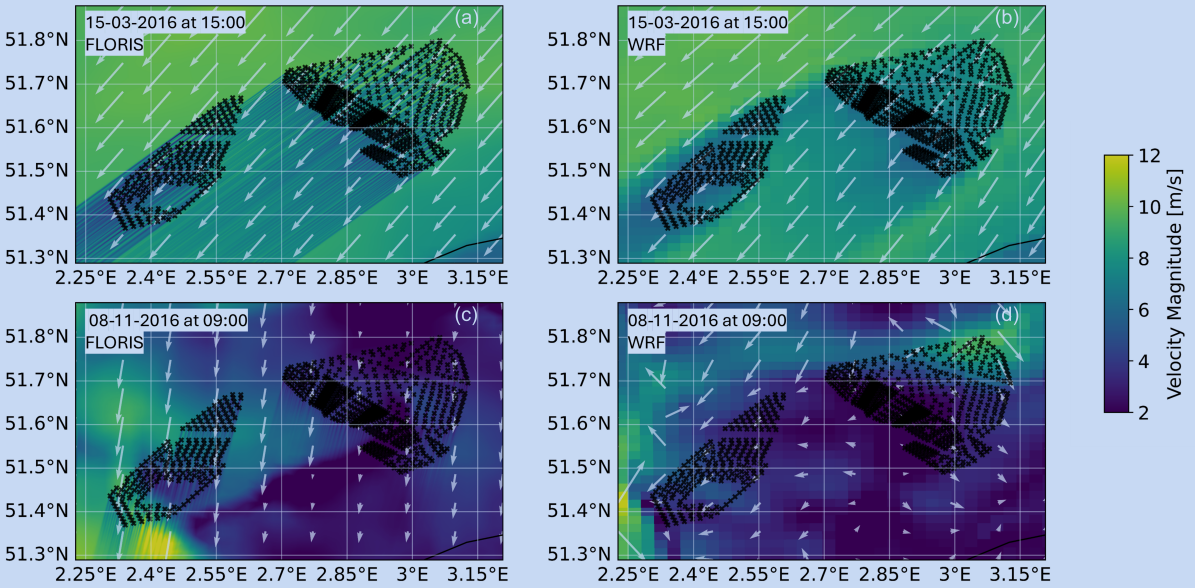


Figure 8. The velocity field for the TurboPark A=0.04 model with varying TI (a,c), and corresponding WRF velocity field (b,d) for a steady case (15-03-2016 at 15:00) (a,b), and a transient case (08-11-2016 at 09:00) (c,d).

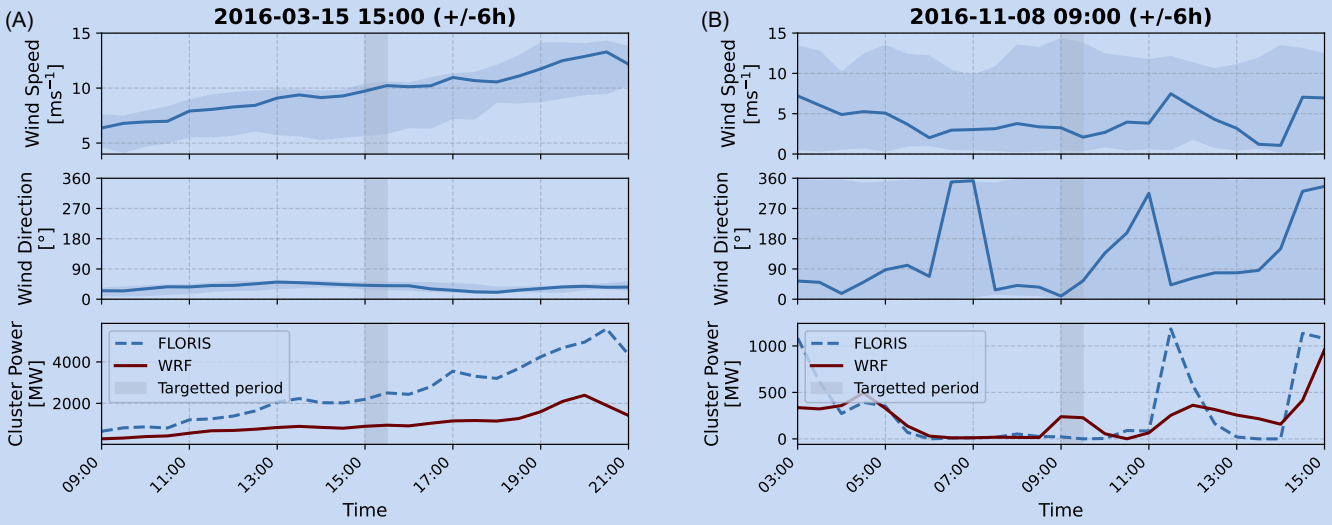


Figure 9. Time series of wind speed, wind direction, and cluster power output for WRF and TurboPark A=0.04 (heterogeneous, varying TI) for a steady case on 15-03-2016 (b) and a strongly transient case on 08-11-2016 (right), shown over a ±6-hour window around 15:00. Shaded blue area indicates lower/upper bounds of wind speed/direction across the WRF domain within the wind farm bounds. Grey area indicates the timestamp at which the snapshots of Fig. 8 were retrieved.

4 Conclusions

This study investigates how wake losses of offshore wind farm cluster depend on the modeling approach, motivated by the lack of systematic, year-long comparisons between numerical weather prediction models and fast running engineering wake models. By analysing a meteorologically representative year for the planned Princess Elisabeth wind farm cluster and the existing BE-NL wind farm cluster and comparing wake impacts simulated with WRF (Part I) and commonly used engineering wake models (Part II), the presented in this work provide a framework to evaluate the spread in predicted wake effects at both the farm and farm–farm scale for both modeling approaches.

Engineering wake models (with different inflow setups) are compared against WRF for total wind farm power production. In general, engineering wake models predict higher power production and therefore smaller wake losses compared to WRF. Differences arising from the choice of engineering wake model are larger than those due to inflow setup, indicating that model formulation has a stronger influence on total farm power estimates than the specification of inflow conditions. Among the considered engineering wake models, TurboPark with $A = 0.04$ shows the closest agreement with WRF, the inflow setup that more closely agrees with WRF is the heterogeneous inflow and varying turbulence intensity (TI).

Including inflow heterogeneity at the grid cell level can locally appear to reduce agreement with WRF; however, this effect is caused by bias compensation. In particular, wind speed gradient bias (between WRF and the engineering wake model) offset overestimations of power production inherent to the engineering wake models, leading to an apparent improvement in agreement at specific locations. When considered in a spatially and temporally averaged sense, heterogeneous inflow configurations show a closer agreement with WRF.

Separating wake losses into internal and external wake energy losses indicates additional differences between the two modeling approaches (WRF vs engineering wake models). For both losses, differences between engineering wake models are larger than differences associated with inflow setup when comparing to WRF. External wake energy loss estimates have a larger spread between modeling approaches than internal wake energy losses, reflecting the higher sensitivity of farm–farm interactions to engineering wake model. Engineering wake models that account for turbulence intensity variations, such as TurboPark and the Cumulative Curl model, tend to show closer agreement with WRF and better reproduce the spatial patterns of wake effects. In contrast, engineering wake models with similar spatiotemporal averaged internal wake energy loss estimates can still exhibit weaker spatial correspondence with WRF, highlighting that agreement in spatiotemporal averaged losses does not mean that the spatial internal wake energy structure is captured.

Seasonal variations in wake losses are present across both modeling approaches, with larger differences during summer than winter. In summer there are lower wind speeds and more stable atmospheric conditions (Part I), under which wake recovery is reduced and the sensitivity of engineering wake model estimates to wake recovery is increased. Although external wake energy losses are smaller in absolute magnitude than internal wake energy losses, their deviations relative to WRF are relatively larger, particularly during summer. The stability classes analysis shows indeed that this seasonal behaviour is linked to stable atmospheric conditions, under which differences between modeling approaches systematically increase. This confirms that atmospheric stability is a dominant physical mechanism governing the spread of wake energy loss estimates, explaining why

discrepancies between modeling approaches are largest during summer and why models with an explicit turbulence dependent wake recovery show closer agreement with WRF, especially for external wake interactions.

The flow field comparison depicts certain conditions under which differences between the modeling approaches arrise. For quasi-steady flow situations, TurbOPark $A = 0.04$ reproduces the velocity deficit patterns of WRF. In contrast, under strongly transient inflow conditions with strong changes in wind direction, the steady state assumptions used by engineering wake models limit their ability to capture the dynamically evolving flow structures presengt in WRF, which causes larger differences between the modeling approaches. However, such transient conditions occur infrequently suggesting that the impact is limited for long-term wake studies.

While this comparison between modeling approaches provides insight into the spread of long-term wake estimates and what drives them, targeted validation against long-term observations will be required to determine which modeling approaches most realistically represent intra-farm and farm–farm interactions.

Code and data availability. FLORIS v4.4 is available at https://github.com/NREL/floris/releases/tag/v4.4

Appendix A: Verification engineering wake models and WRF

To ensure consistent results between the different modeling approaches (i.e., engineering wake models and WRF), the no-WF simulations from both approaches are compared. In the no-WF simulations, wind turbines are not explicitly included; instead, the power production is calculated from the wind speed using the turbine power curve. Fig. A1 compares the total BE–NL cluster power estimated by the engineering models with the power estimated by WRF. Overall we can see that the cluster power estimated by WRF and the engineering wake models are in close agreement thus validating that all inputs from WRF are fed consistently to the engineering wake model setups. As expected, the homogeneous engineering setups exhibit a substantially larger spread compared to the heterogenous setups. Incorporating spatial heterogeneity in the engineering models yields an improved agreement with WRF. Indeed, the no WF wind field is not uniform and can vary substantially over large distances, e.g. due to the presence of coastal gradients or mesoscale weather systems. The remaining discrepancies between the heterogeneous setups of the engineering wake models and WRF arise from differences in how the inflow wind speed is defined for the engineering wake models. Here, the wind speed at 96 m is used, whereas in WRF the power is calculated using the wind speed at hub height, which is different from turbine to turbine. This mismatch in reference height explains the minimal remaining differences.

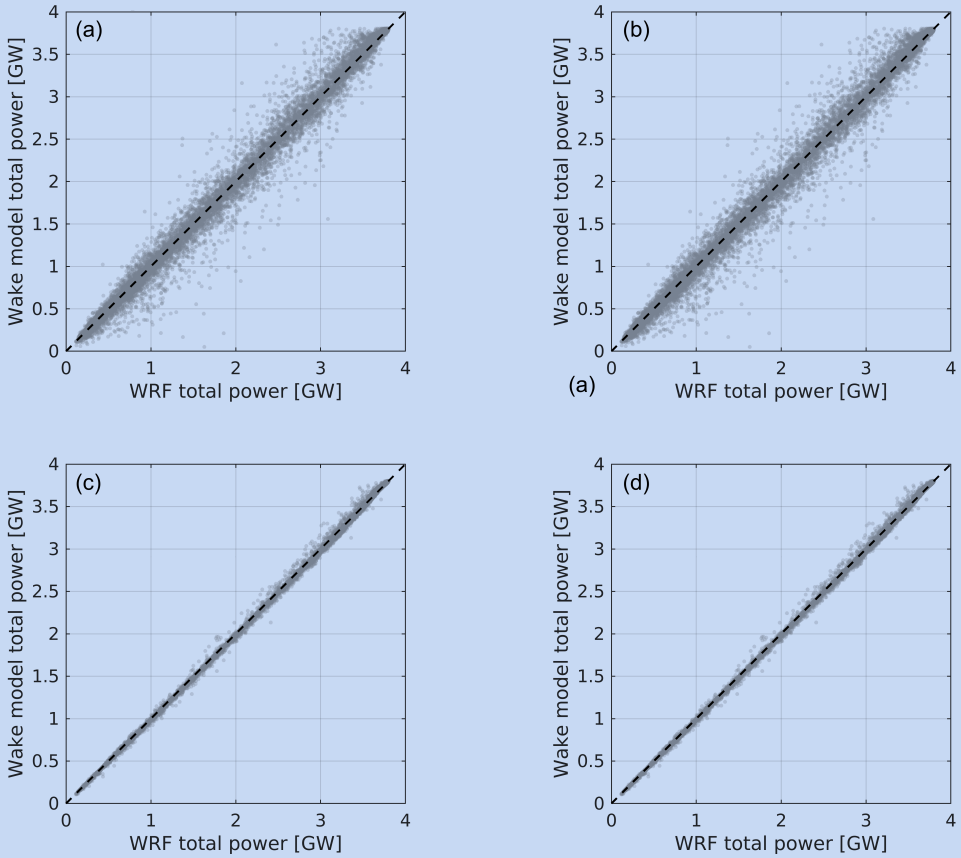


Figure A1. Total BE–NL wind farm cluster power for the no WF simulation compared between WRF and the four engineering wake model setups (a) homogeneous with fixed TI (slope=1.001, $R^2 = 0.990$), (b) homogeneous with varying TI (slope=1.001, $R^2 = 0.990$), (c) heterogeneous with fixed TI (slope=1.000, $R^2 = 0.998$), and (d) heterogeneous with varying TI (slope=1.000, $R^2 = 0.998$). The dashed line represents the 1:1 line.

Appendix B: Spatiotemporally averaged power

Table B1. R^2, RMSE [GW], and mean bias [GW] for the different engineering wake models (with PE) compared against WRF, shown for the four model setups: homogeneous fixed TI, homogeneous varying TI, heterogeneous fixed TI, and heterogeneous varying TI. Colour shading highlights relative performance of the engineering wake model within each metric (smallest = dark green, largest = dark red). Typographic emphasis (smallest = bold, largest = italic & underlined) highlights relative performance of the setups of the engineering wake models within each metric.

	Homogeneous						**Heterogeneous**					
	Fixed TI			Varying TI			Fixed TI			Varying TI		
Model	R^2	RMSE	Bias	R^2	RMSE	Bias	R^2	RMSE	Bias	R^2	RMSE	Bias
Gauss-BPA	*0.754*	*0.600*	*0.303*	0.773	0.575	**0.294**	0.768	0.582	0.303	**0.786**	**0.559**	0.294
Cumul. Curl	*0.848*	*0.471*	0.239	0.865	0.444	**0.235**	0.863	0.448	*0.240*	**0.879**	**0.421**	0.236
Jensen 0.02	*0.792*	0.551	0.280	0.792	*0.552*	0.280	**0.807**	**0.531**	**0.280**	0.806	0.532	*0.281*
Jensen 0.04	*0.681*	*0.683*	*0.418*	0.681	0.683	0.417	**0.697**	**0.665**	0.417	0.696	0.667	**0.417**
TurbOPark 0.04	0.868	*0.439*	*0.203*	*0.882*	0.416	**0.201**	0.882	0.415	0.203	**0.895**	**0.391**	0.201
TurbOPark 0.06	*0.808*	*0.529*	0.294	0.822	0.509	**0.292**	0.824	0.507	*0.294*	**0.837**	**0.488**	0.293

Appendix C: Time dependent behavior

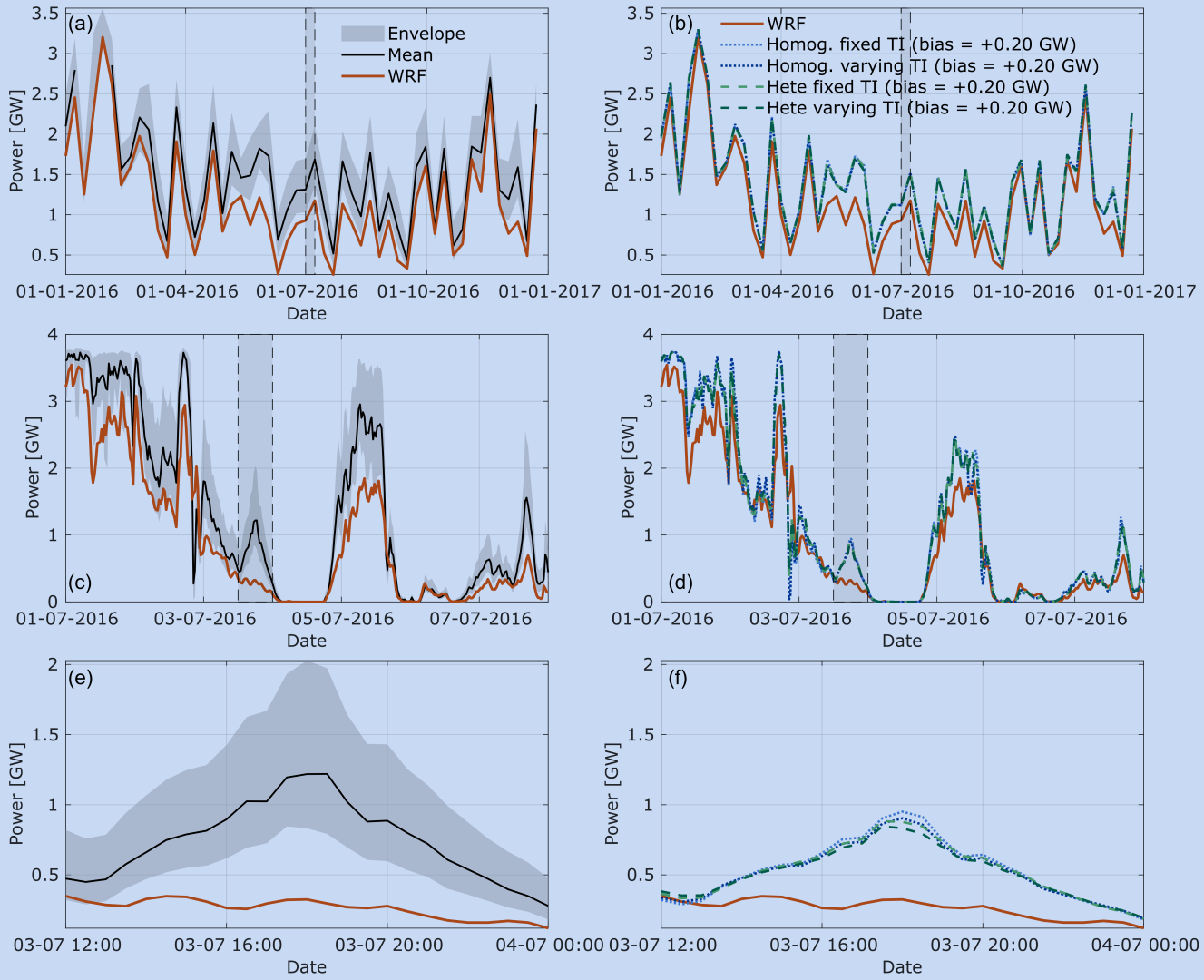


Figure C1. Total wind farm power (GW) for the BE–NL offshore wind farm cluster for simulations with PE. Shown are WRF (without PE), and the mean and envelope of all engineering models (a,c,e), and the different configurations of Turbopark with induction factor A=0.04 (b,d,f). The top row (a,b) shows weekly averages computed from 30-min data, the middle row (c,d) shows a one-week zoom (1–7 July 2016) at 30 min resolution, and the bottom row (e,f) shows a twelve-hour zoom (3 July 2016) also at 30 min resolution. The dashed box shows the time period zoom within the longer time series.

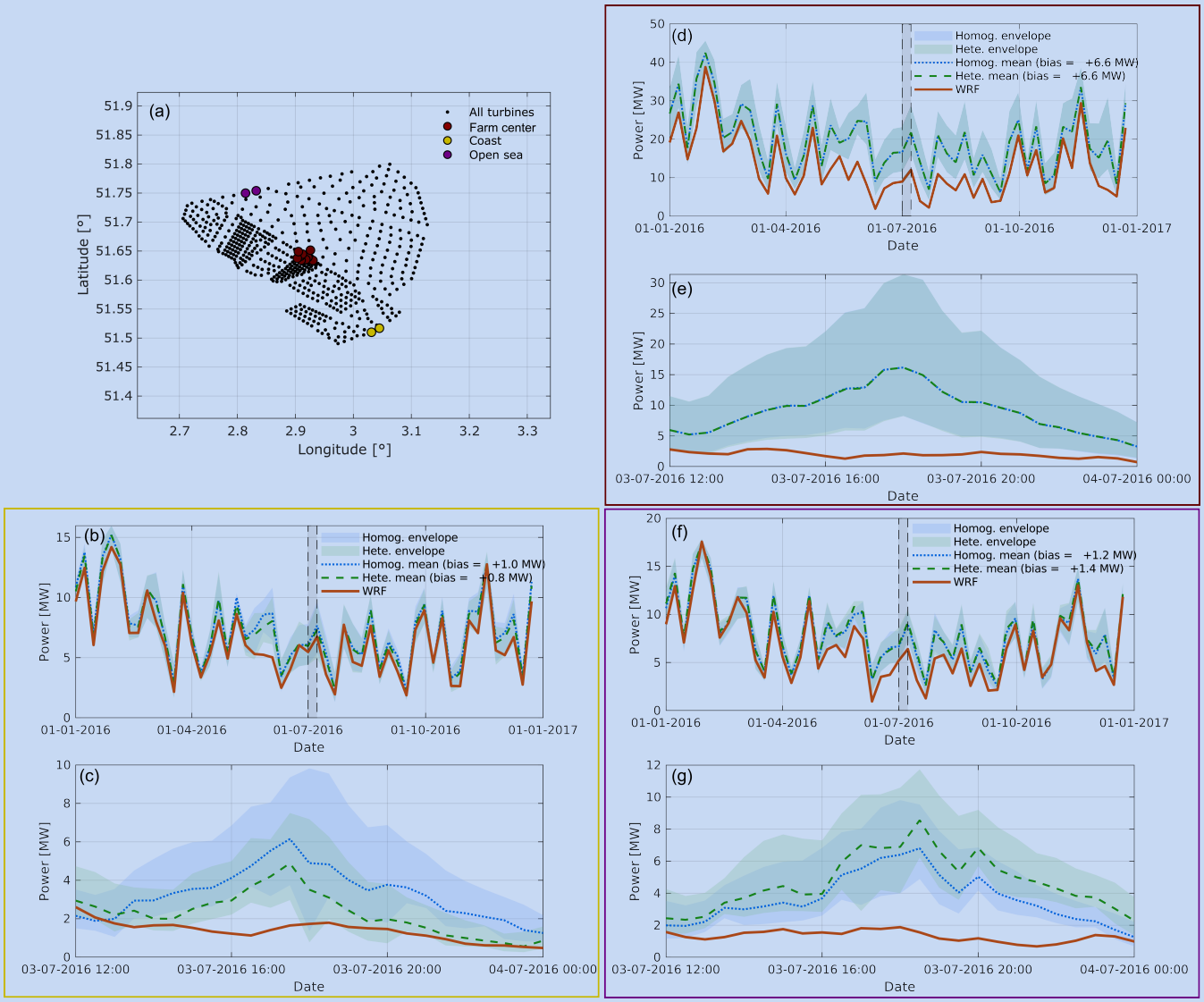


Figure C2. Grid cell power output (MW) at three representative locations within the BE-NL wind farm cluster for simulations with PE. Panel (a) shows the locations of the selected grid cells, representing the farm center, coastal, and open-sea regions. Panels (d,b,f) show weekly averages computed from 30-min data, while panels (e,c,g) show a twelve-hour zoom on 3 July 2016 at 30-min resolution. Shown are WRF (without PE) and the mean and envelope of all engineering wake models grouped by homogeneous and heterogeneous setups. The dashed box indicates the zoomed period within the full time series. Bias is defined as the engineering wake model power minus WRF power.

Author contributions. SP contributed to the conceptualization, formal analysis, data curation, software, validation, methodology, visualisation, and writing (original draft, review and editing). MFH contributed to conceptualization, methodology, visualisation, funding, supervision and writing (review and editing). ML contributed to the data curation, software, validation, methodology, visualization and and writing (original draft, review and editing). RB contributed to writing (review and editing). SB contributed to the conceptualization, funding, and writing (review and editing). WM contributed to the conceptualization, formal analysis, validation, methodology, visualisation, funding, and writing (review and editing).

Competing interests. The authors declare that no competing interests are present.

Acknowledgements. SP and MFH were funded by MIT Climate Grand Challenges. WM and ML acknowledge support from the Flemish Agency for Innovation and Entrepreneurship (VLAIO) through the Cloud4Wake project and from the European Union through the DTWO project funded through Horizon Europe, grant no. 101146689. The resources and services used in this work were provided by the VSC (Flemish Supercomputer Center), funded by the Research Foundation-Flanders (FWO) and the Flemish Government.

References

Akhtar, N., Geyer, B., Rockel, P., and Schrum, C.: Accelerating deployment of offshore wind energy alter wind climate and reduce future power generation potentials, Scientific Reports, 11, 2021.

Antonini, E. and Caldeira, K.: Atmospheric pressure gradients and Coriolis forces provide geophysical limits to power density of large wind farms, Applied Energy, 281, 459–469, 2021.

Barthelmie, R. J., Pryor, S. C., Frandsen, S. T., Hansen, K. S., Schepers, J. G., Rados, K., Schlez, W., Neubert, A., Jense, n. L. E., and Neckelmann, S.: Quantifying the Impact of Wind Turbine Wakes on Power Output at Offshore Wind Farms, Journal of Atmospheric and Oceanic Technology, 27, 1302 – 1317, 2010.

Bastankhah, M. and Porté-Agel, F.: A new analytical model for wind-turbine wakes, Renewable energy, 70, 116–123, 2014.

Bastankhah, M., Welch, B. L., Martínez-Tossas, L. A., King, J., and Fleming, P.: Analytical solution for the cumulative wake of wind turbines in wind farms, Journal of Fluid Mechanics, 911, A53, https://doi.org/10.1017/jfm.2020.1037, 2021.

Bay, C., Fleming, P., Doekemeijer, B., King, J., Churchfield, M., and Mudafort, R.: Addressing deep array effects and impacts to wake steering with the cumulative-curl wake model, Wind Energy Science, 8, 401–419, 2023.

Borgers, R., M., D., Wijnant, I., Stepek, A., Stoffelen, A., Akhtar, N., Neirynck, J., Van de Wallen, J., Meyers, J., and van Lipzig, N.: Mesoscale modelling of North Sea wind resources with COSMO-CLM: model evaluation and impact assessment of future wind farm characteristics on cluster-scale wake losses, Wind Energy Science, 9, 697–719, 2024.

Cuevas-Figueroa, G., Stansby, P., and Stallard, T.: Accuracy of WRF for prediction of operational wind farm data and assessment of influence of upwind farms on power production, Energy, 254, 2022.

Emeies, S.: A simple analytical wind park model considering atmospheric stability, Wind Energy, pp. 459–469, 2010.

Farrell, A., King, J., Draxl, C., Mudafort, R., Hamilton, N., Bay, C. J., Fleming, P., and Simley, E.: Design and analysis of a wake model for spatially heterogeneous flow, Wind Energy Science, 6, 737–758, https://doi.org/10.5194/wes-6-737-2021, 2021.

Fischereit, J., Brown, R., Larsén, X., Badger, J., and Hawkes, G.: Review of mesoscale wind-farm parameterizations and their applications, Boundary-Layer Meteorology, 182, 175–224, 2022a.

Fischereit, J., Sahan, M. E., Imberger, M., and Larsén, X. G.: Benchmarking model coupling and wind farm parameterizations for wind energy applications, in: EMS Annual Meeting 2025, pp. EMS2025–495, Ljubljana, Slovenia, https://doi.org/10.5194/ems2025-495, 2025.

Fischereit, J. anrel2025nd Schaldemose Hansen, K., Larsen, X., van der Laan, M., Rethore, P.-E., and Murcia Leon, J.: Comparing and validating intra-farm and farm-to-farm wakes across different mesoscale and high-resolution wake models, Wind Energy Science, 7, 1069–1091, https://doi.org/10.5194/wes-7-1069-2022, 2022b.

Fitch, A., Lundquist, J., Dudhia, J., Gupta, A.K.and Michalakes, J., and Barstad, I.: Local and mesoscale impacts of wind farms as parameterized in a mesoscale NWP Model, Monthly Weather Review, 140, 3017–3038, 2012.

Frandsen, S.: Turbulence and turbulence-generated structural loading in wind turbine clusters, Ph.D. thesis, risø-R-1188(EN), 2007.

Hansen, K., Rethore, P.-E., Palma, J., Hevia, B., Prospathopoulos, J., Pena, A., Ott, S., Schepers, G., Palomares, A., van der Laan, M., and Volker, P.: Simulation of wake effects between two wind farms, in: Journal of Physics: Conference Series, vol. 625, 2015.

Katic, I., Højstrup, J., Jensen, N. O., et al.: A simple model for cluster efficiency, in: European wind energy association conference and exhibition, vol. 1, pp. 407–410, A. Raguzzi Rome, Italy, 1986.

King, J., Fleming, P., King, R., Martínez-Tossas, L. A., Bay, C. J., Mudafort, R., and Simley, E.: Control-oriented model for secondary effects of wake steering, Wind Energy Science, 6, 701–714, https://doi.org/10.5194/wes-6-701-2021, 2021.

Larsén, X. G.: Calculating Turbulence Intensity from mesoscale modeled Turbulence Kinetic Energy, Technical report (dtu wind energy e-0233), DTU Wind Energy, Technical University of Denmark, Roskilde, Denmark, https://backend.orbit.dtu.dk/ws/portalfiles/portal/364980906/TKE2TI-20240627.pdf, 2024.

Lundquist, J., DuVivier, K., Kaffine, D., and Tomaszewski, J.: Costs and consequences of wind turbine wake effects arising from uncoordinated wind energy development, Nature Energy, 4, 26–34, https://doi.org/10.1038/s41560-018-0281-2, 2019.

Maas, O. and Siegfried, R.: Wake properties and power output of very large wind farms for different meteorological conditions and turbine spacings: a large-eddy simulation case study for the German Bight, Wind Energy Science, 7, 715–739, 2022.

Munters, W., Adiloglu, B., Buckingham, S., and van Beeck, J.: Wake impact of constructing a new offshore wind farm zone on an existing downwind cluster: a case study of the Belgian Princess Elisabeth zone using FLORIS, in: Journal of Physics: Conference Series, vol. 2265, 2022.

NREL: FLORIS Version 4.4, GitHub repository, 2025.

Nygaard, N. and Hansen, S.: Wake effects between two neighbouring wind farms, in: Journal of Physics: Conference Series, vol. 753, 2016.

Nygaard, N., Steen, S., Poulsen, L., and Pedersen, J.: Modelling cluster wakes and wind farm blockage, in: Journal of Physics: Conference Series, vol. 1618, 2020.

Nygaard, N., Poulsen, L., Svensson, E., and Pedersen, J.: Large-scale benchmarking of wake models for offshore wind farms, in: Journal of Physics: Conference Series, vol. 2265, p. 022008, IOP Publishing, 2022.

Peña, A., Schaldemose Hansen, K., Ott, S., and van der Laan, M.: On wake modeling, wind-farm gradients, and AEP predictions at the Anholt wind farm, Wind Energy Science, 3, 191–202, 2018.

Pedersen, J., Svensonn, E., Poulsen, L., and Nygaard, N.: Turbulence Optimized Park model with Gaussian wake profile, in: Journal of Physics: Conference Series, vol. 2265, 2022.

Peña, A., Réthoré, P.-E., and van der Laan, M. P.: On the application of the Jensen wake model using a turbulence-dependent wake decay coefficient: the Sexbierum case, Wind Energy, 19, 763–776, 2016.

Porté-Agel, F., Bastankhah, M., and Shamsoddin, S.: Wind-Turbine and Wind-Farm Flows: A review, Boundary-Layer Meteorology, 174, 1–59, 2020.

Prosper, M., Otero-Casal, C., Canoura Fernandez, F., and Miguez-Macho, G.: Wind power forecasting for a real onshore wind farm on complex terrain using WRF high resolution simulations, Renewable Energy, 135, 674–686, 2019.

Pryor, S., Barthelmie, R., and Shepherd, T.: Wind power production from very large offshore wind farms, Joule, 5, 2663–2686, 2021.

Skamarock, W. C., Klemp, J. B., Dudhia, J., Gill, D. O., Barker, D., Duda, M. G., and Powers, J. G.: A Description of the Advanced Research WRF Version 3, Tech. Rep. NCAR/TN-475+STR, National Center for Atmospheric Research, Boulder (CO), USA, 2008.

Stevens, R. J., Gayme, D. F., and Meneveau, C.: Coupled wake boundary layer model of wind-farms, Journal of renewable and sustainable energy, 7, 2015.

Stieren, A. and Stevens, R.: Impact of wind farm wakes on flow structures in and wround downstream wind farms, Flow, 2, 2022.

van der Laan, M., Hansen, K., Sorensen, N., and Rethore, P.-E.: Predicting wind farm wake interaction with RANS: an investigation of the Coriolis force, in: Journal of Physics: conference Series, vol. 625, 2015.

van der Laan, M. P., García-Santiago, O., Kelly, M., Meyer Forsting, A., Dubreuil-Boisclair, C., Seim, K. S., Imberger, M., Peña, A., Sørensen, N. N., and Réthoré, P.-E.: A new RANS-based wind farm parametrization and inflow model for wind farm cluster modeling, Wind Energy Science Discussions, 2022, 1–38, 2022.

van der Laan, M. P., García-Santiago, O., Kelly, M., Meyer Forsting, A., Dubreuil-Boisclair, C., Sponheim Seim, K., Imberger, M., Peña, A., Sørensen, N. N., and Réthoré, P.-E.: A new RANS-based wind farm parameterization and inflow model for wind farm cluster modeling, Wind Energy Science, 8, 819–848, 2023.

Veers, P., Dykes, K., Lantz, E., Barth, S., Bottasso, C., Carlson, O., Clifton, A., Green, J., Green, P., Holttinen, H., Laird, D., Lehtomäki, V., Lundquist, J., Manwell, J., Marquis, M., Meneveau, C., Moriarty, P., Munduate, X., Muskulus, M., Naughton, J., Pao, L., Paquette, J., Peinke, J., Robertson, A., Rodrigo, J. S., Sempreviva, A., Smith, J. C., Tuohy, A., and Wiser, R.: Grand challenges in the science of wind energy, Science, 366, https://doi.org/10.1126/science.aau2027, 2019.